NANOSCALE STRUCTURAL AND MECHANICAL PROPERTIES OF ALPHA-SYNUCLEIN AMYLOID FIBRILS

KIM SWEERS

NANOSCALE STRUCTURAL AND MECHANICAL PROPERTIES OF ALPHA-SYNUCLEIN AMYLOID FIBRILS

Atomic force microscopy studies

Kim Sweers

Thesis committee members:

Prof. dr. L ter Stappen	Universiteit Twente (Chairman)
Prof. dr. V. Subramaniam	Universiteit Twente (Promotor)
Dr. M.L. Bennink	Universiteit Twente (Assistent Promotor)
Prof. dr. M. Radmacher	Universität Bremen
Prof. dr. R. Mezzenga	ETH Zürich
Dr. T.P.J. Knowles	University of Cambridge
Prof. dr. P.J. Dijkstra	Soochow University
Prof. dr. W.J. Briels	Universiteit Twente
Prof. dr. H.J.W. Zandvliet	Universiteit Twente

Paranimfen:

D.R. Dekker
M.H.W. Stopel

The work in this thesis was performed at the Nanobiophysics group, MESA+ Institute for Nanotechnology, Faculty of Science & Technology, University of Twente, PO box 217, 7500 AE, Enschede, The Netherlands.

Copyright © 2012, K.K.M. Sweers, All rights reserved,
This thesis can be downloaded from:
http://dx.doi.org/10.3990/1.9789036533485

Printed by Printservice Ede

ISBN 978-90-365-3348-5

NANOSCALE STRUCTURAL AND MECHANICAL PROPERTIES OF ALPHA SYNUCLEIN FIBRILS

ATOMIC FORCE MICROSCOPY STUDIES

PROEFSCHRIFT

ter vekrijging van
de graad van doctor aan de Universiteit Twente,
op gezag van de rector magnificus,
prof. dr. H. Brinksma,
volgens besluit van het College voor Promoties
in het openbaar te verdedigen
op woensdag 16 mei om 14:45 uur

door

Kim Katharine Maria Sweers
geboren op 15 november 1982
te Noordoostpolder

Dit proefschrift is goedgekeurd door:

Prof. dr. V. Subramaniam	(Promotor)
Dr. M.L. Bennink	(Assistent Promotor)

Nothing is true, everything is permitted

- Alamut, Vladimir Bartol - 1938

TABLE OF CONTENTS

Chapter 1. Introduction

Chapter 2. Nanomechanical properties of single amyloid fibrils

Chapter 3. Atomic force microscopy study of substrate influences on morphologies of α-synuclein amyloid fibrils

Chapter 4. Morphological and nanomechanical properties of α-synuclein fibrils on supported lipid bilayers investigated by atomic force microscopy

Chapter 5. Atomic force microscopy under controlled conditions reveals structure of C-terminal region of α-synuclein in amyloid fibrils

Chapter 6. Structural model for α-synuclein fibrils derived from high resolution imaging and nanomechanical studies using atomic force microscopy

Chapter 7. Nanomechanical properties of α-synuclein amyloid fibrils: a comparative study by nanoindentation, harmonic force microscopy, and Peakforce QNM

Chapter 8. Spatially resolved frequency-dependent elasticity measured with pulsed force microscopy and nanoindentation

Chapter 9. Nanoscale patterned materials for mechanical characterization of α-synuclein fibrils using atomic force microscopy

Chapter 10. Conclusions

CHAPTER 1

Introduction

Accumulation of protein deposits is a pathological hallmark of several systemic and neurodegenerative diseases. The pathologies of these diseases are very diverse, however they are all characterized by the aggregation of a specific protein or peptide. Although the sequence, structure and function of the proteins are very different, the aggregates found for different diseases have a similar structure, and are referred to as amyloid fibrils [1-4]. Amyloid is a general term for aggregates with the following characteristics: (1) the fibrils are around 10 nm in diameter, (2) they bind to dyes such as Thiovlavin T and (3) the fibrils consists of cross β-sheets stacked perpendicular to the fibril axis and exhibit intermolecular hydrogen bonds [3,5,6,7,8].

PROTEIN MISFOLDING & DISEASES

PROTEIN MISFOLDING

The underlying mechanism to protein aggregation is protein misfolding. Most proteins need, aside from the correct amino acid sequence, to be folded correctly to be able to perform their function. Protein folding is a complex stochastic process leading to the most thermodynamically stable fold, which is often also the protein's native state [9,10]. This complex folding process can be described using an energy landscape for the protein regarding all the possible conformations and interactions. During the downhill trajectory in the energy landscape the protein samples many intermediate states. In some cases in this folding process the protein could get stuck in local minima representing non-native or misfolded states. Also chemical modification can lead to misfolded or partially unfolded states. However, the functionality of the protein itself requires a certain degree of freedom which favors partially folded states or, for some proteins, a natively unfolded state, unfolded hydrophobic regions of the polypeptide chain are prone to aggregation [11].

The cell provides multiple pathways, for instance with the use of chaperone molecules, to control the protein folding processes. Quality control systems within the living cell are able to detect and target misfolded proteins which cannot be repaired to the cell degradation machineries, such as the ubiquitin proteasome system [3,12,13,14]. When this degradation pathway fails, an accumulation of misfolded proteins can lead to disease [3,15,16]. This could be caused by either a loss of function of the misfolded protein or by the toxicity of the misfolded protein species. Due to the tendency of the misfolded proteins to aggregate, systemic or neurodegenerative diseases are often accompanied by aggregated protein deposits. These deposits can be found in single organs like the brain in case of Alzheimer's and Parkinon's disease or in multiple organs throughout the body in case of systemic amyloidoses [16,17,18].

PARKINSON'S DISEASE

Parkinson's disease (PD), first described in 1817 by James Parkinson, is a common neurodegenerative movement disorder affecting about 1 out of 50 people in the Netherlands [19]. However, epidemiological studies suggest that many cases are unidentified and untreated due to the gradual development of the disease. The economic burden is estimated by the Parkinson's Disease Foundation to be 10.5 billion euros per year in the EU. Approximately 40% of these costs are direct costs associated with physician visits, medication and other health care costs [20].

Typical symptoms of the disease are: tremor (around 4-5 per second), mask-like facial

expression, flexed posture and deficiency in spontaneous movement (Bradykinesia) [21]. Apart from the symptoms described above the pathological features are protein inclusions called Lewy Bodies, and the loss of dopaminergic neurons in the substantia nigra pars compacta. A cure for this disease is still not available. Current treatment only alleviates the symptoms, and includes dopamine-based medication to retain motor function or deep brain stimulation to diminish the tremors [21]. Diagnosis of PD is also not straightforward and can only be done by clinical examination (for instance with simple motor function scorings tests) and medical history, supported by positron emission tomography (PET) scans [21]. However, this is often in a late stage of the disease, when almost 80% of the dopaminergic neurons have already died. The final diagnosis can only be done post mortem on the basis of Lewy pathology. Both the cure and the diagnosis for PD are challenged by the limited knowledge of the cause of the disease. Even Lewy pathology is not straightforward since Lewy bodies are found in post mortem brains of patients with and without symptoms of PD.

ALPHA-SYNUCLEIN

The major component of these Lewy Bodies is the protein α-synuclein [22]. α-Synuclein is a small, 140 amino-acid protein that belongs to the class of proteins that are intrinsically disordered or natively unfolded at in vitro conditions [3]. The N-terminal region is known to be involved in membrane binding [23]. The central region of α-synuclein is very hydrophobic and plays a key role in aggregation. The C terminus is highly negatively charged, a net charge of -13 e compared to the +4 e net charge of the N-terminus and central region.

α-Synuclein is abundantly expressed throughout the central nervous system and mainly localized in the nucleus and in presynaptic nerve terminals. [17,24]. However, the specific function of α-synuclein remains unclear. Recently, evidence was found that α-synuclein associates with cytoskeletal components. It interacts with tubulin and the interaction with microtubules alters the cell surface recruitment of the dopamine transporter [25]. α-Synuclein also promotes microtubule assembly and it associates with the actin cytoskeleton [26,27]. In addition to the evidence for association with cytoskeletal components, other physiological roles have been proposed. These include involvement in neurotransmitter release and vesicle recycling [23]. Several studies have demonstrated an interaction between α-synuclein and lipid vesicles or membranes [23, 28-30]. Lipids have been found to play a role in Parkinson's disease pathology as modulators of the α-synuclein structure and putative function, protein-membrane interactions and even α-synuclein aggregation [31].

Aside from being the main component of the Lewy bodies, a causal relation between

α-synuclein and PD has not yet been resolved. Several α-synuclein mutants, with point mutations situated in the N-terminal region, cause rare familial forms of PD [32-34]. Overexpression of α-synuclein, leading to high concentrations of the protein also seems to cause PD [35,36]. These results together indicate a relation between α-synuclein and PD. However, the correlation between PD and α-synuclein/ Lewy bodies is still under debate. Whether the aggregated α-synuclein or Lewy bodies themselves are toxic to the cell remains unclear [22,37]. The aggregation of the protein into amyloid fibrils and storing these fibrils in larger inclusions could very well be a protective mechanism of the cell against the 'toxic' misfolded protein.

AMYLOID FIBRILS

The term amyloid fibril was introduced in 1854 by the German physician Rudolph Virchow. He thought it was a form of starch or cellulose and therefore called it amyloid. After macroscopic studies of body organs and tissues of patients, more microscopic studies started to appear, for instance light microscopy combined with fluorphores like Thioflavin T and Congo red. These dyes and birefringence experiments suggested an ordered structure within the fibrils, which led to submicroscopic studies of these amyloid fibrils. More recently, amyloid fibril formation was found to be a more generic property of proteins [38-40].

FIBRIL STRUCTURE

The structure of the fibrils appeared to be very diverse or polymorphous, not only between fibrils assembled of different proteins, but also between fibrils made of the same protein. The general characteristics listed on page 1 however are similar for all fibrils [5,41,42]. Polymorphism refers to the ability of a solid material to exist in multiple forms or crystallographic structures. The differences between fibrils of different proteins have been studied and have led to assembly models with general characteristics [43]. However, polymorphism is even found in aggregations with one single protein species, for example fibrils formed of a single protein species displaying a twist or not [43]. There are two suggested explanations for amyloid polymorphism. Firstly, the distinct morphologies found in the sample are caused by different lateral associations of protofilaments without a significant molecular difference of the monomers within these protofilaments. Secondly, the monomers within the protofilaments are actually folded differently, which causes morphological differences between the fibril species (see Figure 1).

Several morphological studies have been done on protein fibrils to investigate

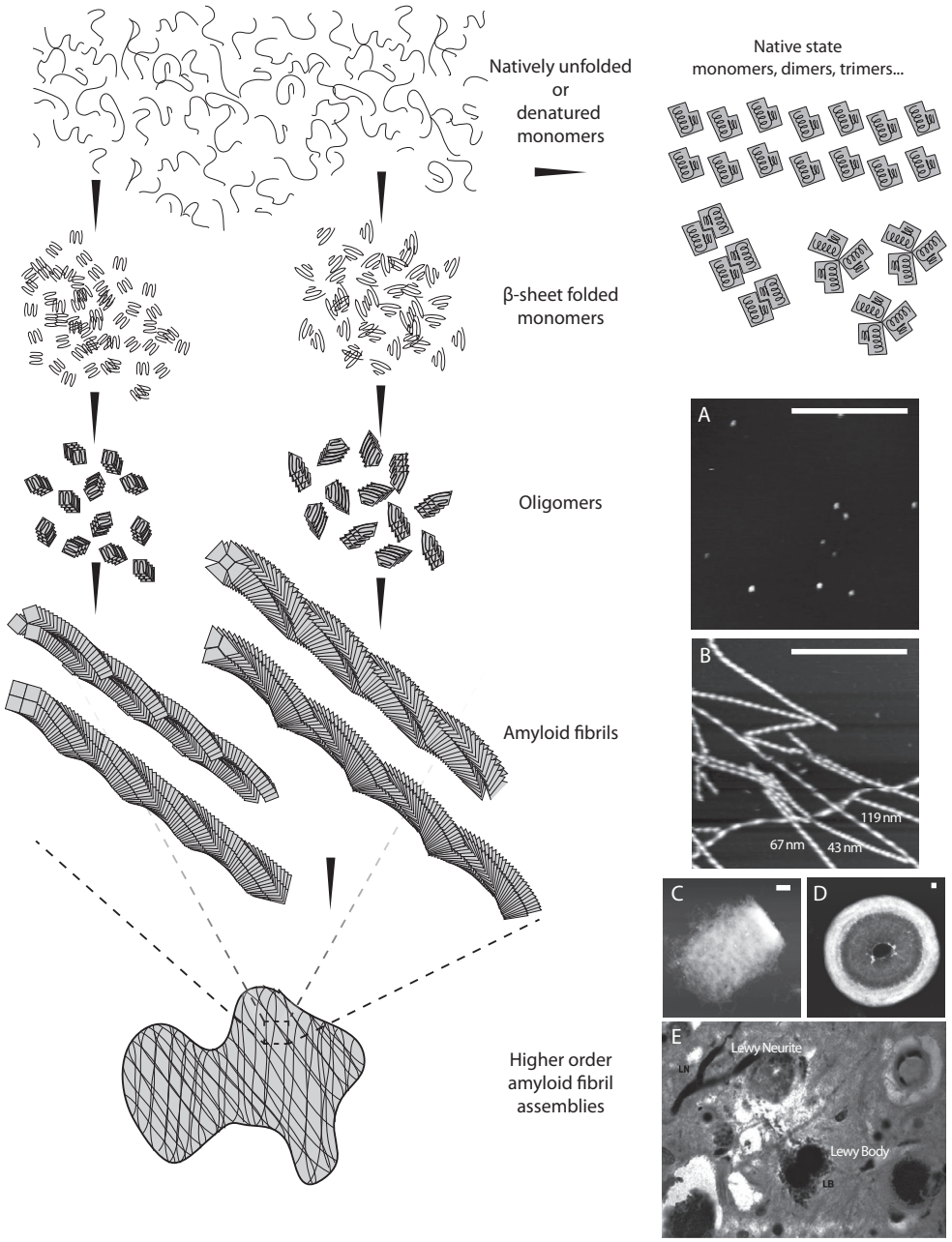

FIGURE 1; General scheme of amyloid protein aggregation, from natively unfolded or denatured state to functional native state or polymorphic amyloid fibrils. From the scheme it is clear that differently shaped fibrils can result from either differently folded monomers or similarly folded filaments that are differently laterally associated. Images on the right are AFM images of α-synuclein in different aggregation states: oligomers, amyloid fibrils (displaying three morphologically different fibrils with different periodicities) and higher order assemblies under two different aggregation conditions (neutral pH and low pH). Scale bars are 1 μm; Z-scales are 15 nm (A&B) and 500 nm and 1500 nm (C&D respectively). Lower image, E, is a histology image of Lewy Bodies stained for α-synuclein found in a Parkinson's Disease brain [Rob de Vos].

amyloid polymorphism [see for reviews 42,44-46]. These studies can be divided into studies with constant aggregation conditions or studies with altered aggregation conditions (like temperature, different solvent, pH or ion concentrations). An example of the latter is the influence of solvent pH on the morphology of α-synuclein protein aggregates, which forms amorphous aggregates at low pH [47]. Agitation is another condition that appears to influence the morphology. Alzheimer's Aβ fibrils either form twisting filaments or laterally-associated filaments depending on whether the sample is agitated or not [48]. This study even proves that seeds can force monomers to form fibrils according to the existing morphology of the seeds irrespective of the aggregation condition. Furthermore, peptide length or point mutations in the protein sequence, pressure during the aggregation, or changes in protein concentration can influence fibril morphology [49,50]. Changing environment can induce different monomer folding pathways or resulting in different laterally associated filaments. For instance, an AFM morphological study on β-lactoglobulin finds five different fibril species containing different number of protofilaments [51]. The glucagon protein is also found to produce fibrils with different number of protofilaments [52,53]. For various other proteins it is also believed that the fibrils consist of different number of filaments that are laterally associated [54-56].

Recent studies combine AFM or electron microscopy with other techniques such as solid state nuclear magnetic resonance (NMR) [48,57-59] as opposed to studies based on only surface scanning techniques [51-53,56] to get more insight in fibril morphology and the underlying assembly mechanisms. Combining different techniques can have advantages; however there are still several open questions in the literature. In case of the fold of α-synuclein two recent solid state NMR studies prove the middle part of the amino acid sequence to be β-strand folded, however one study [57] finds two distinct populations while the other only finds one [58]. Even computational studies are not in agreement over whether polymorphism is caused by different monomeric folds or laterally associated filaments [60,61]. So although every protein produces polymorphic fibrils there is no consensus about the underlying mechanism.

FIBRIL FORMATION

Amyloid fibril formation is thought to be a generic property of proteins under the right conditions. Nucleation-dependent elongation mechanisms are often used to describe the amyloid fibril formation. A critical protein concentration is needed for any aggregation to occur. When this critical concentration is met, the polymerization starts after a certain amount of time, which is referred to as the lag-phase (nucleation). After this, there is a growth phase (elongation) in which fibrils are formed. The lag-phase can be greatly reduced with seeding, meaning adding already mature fibrils to the solution.

This means that already formed fibrils are able to catalyze the formation of new fibrils. Nucleation polymerization describes the elongation of fibrils after the lag-phase. However, the fibril formation process is also proposed to be affected by secondary nucleation pathways [62,63].

The aggregation kinetics can be visualized by the intensity of dyes like Thioflavin T which shows enhanced fluorescence upon binding to structures having across-β conformation, see Figure 2. Therefore almost no fluorescence is observed during the lag phase, and a steep increase is observed in the growth phase [8]. After some time the Thioflavin T fluorescence reaches a plateau, indicating that no new fibrils are formed. However, the process continues by assembling the fibrils in higher ordered structures, see also Figure 1.

As mentioned before the hydrophobic regions of proteins are prone to aggregation. Also the charge of the protein contributes to the aggregation kinetics. Fibril formation can be sped up by high mono- or multivalent ion concentrations. Exposing the hydrophobic region could be obtained by increasing the temperature among other things.

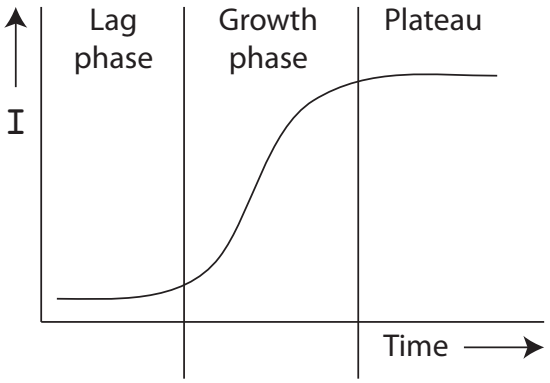

FIGURE 2; Schematic graph of the Thioflavin T fluorescence intensity as a function of time, as observed during the amyloid fibril formation process. The curve shows 3 distinct phases: (i) lag-phase, in which oligomeric species of proteins are already forming(ii) growth phase, in which the fibrils form, (iii) the plateau, where no new fibrils are formed, but existing fibrils are assembled into higher ordered structures.

Underlying questions like what happens in the lag-phase or how does the fibril grow are still unanswered. Whether fibrils grow in single filaments that are intertwining in a later stage, or growing as discrete independent fibrils, which intertwine as a second step is still a debate, see fibril structure section. It is also not completely clear whether the amyloid fibrils grow uni- or bidirectionally. AFM study on amylin fibrils showed a bidirectional growth with no distinct fast or slow end [64]. However, an AFM study on a$\beta_{25\text{-}35}$ shows a more stepwise growth with bursts of rapid growth alternated with

pauses on the fast end [65]. Surfaces probably play a large role in fibril growth. Both studies only showed intermediate fibril species growth on a surface, compared to mature fibrils. These fibrils did not display any periodic morphological features, which could be induced by surface interactions. With an increased amount of ions in solution α-synuclein forms small (~1 nm in height) filaments on a mica surface which are not seen in aggregated samples in solution [66]. This behavior is also shown for $a\beta_{26\text{-}35}$ on POPC lipid membranes [67].

SCOPE OF THIS THESIS

Since the discovery of amyloid fibrils in 1854, the amount of studies done on these fibrils has drastically increased. Initially the studies were conducted using light microscopy, later the arrival of electron microscopes and atomic force microscopes increased the knowledge on amyloid fibrils with increasing resolution. Especially the atomic force microscope has proven to be a very suitable tool because of both the resolution and the ability to probe the protein structures in a more native environment with very precise force control (for instance buffer solutions). Aside from morphological studies done with the AFM also studies investigating mechanical properties have become increasingly popular in the last 10 years. Mechanical properties are not only interesting from a pathological or biomedical point of view, but also from the nanomaterial point of view these mechanical properties are becoming increasingly important. Amyloid fibrils are remarkably stable and can have great adhesive properties, which could make them interesting nanomaterials such as nanowires or even as elementary units in a 3D network such as scaffolds used for tissue engineering applications. Many existing studies are probing the amyloid fibrils on the nanoscale, however these studies are often limited to only a few of the remarkable capabilities of the AFM.

In this thesis the AFM is used to resolve the structural/morphological and mechanical properties of the amyloid fibrils of the protein α-synuclein. Aside from these properties which can be linked to pathological problems of the disease, the influence of different scanning conditions on the results obtained with AFM is also explored. Conditions that are investigated are for instance the effect of different surfaces or environmental conditions (ambient air or buffer solutions). Not only have we studied the influence of these different parameters, but these different conditions are also used to get more insight into the structure of amyloid fibrils and their mechanical properties.

The thesis is divided into three parts, with each one dealing with a well-defined research question. Part III is focused on the mechanical properties of amyloid fibrils, however these mechanical properties are a common thread throughout the thesis.

Therefore an extensive review on mechanical properties of amyloid fibrils measured with AFM is presented in Chapter 2. In the final chapter all conclusions from different chapters are combined to answer the three different research questions.

PART I: SURFACE INFLUENCE

Research Question Part I:

How do substrate surfaces influence the fibril morphology and how can we utilize different surfaces to get a better insight in fibril structure and mechanics?

In the first part of this thesis the influence of the substrate surface on fibril morphology is investigated. In Chapter 3, four different surfaces and their influence on basic measured properties like fibril height and periodicity is studied. The different adsorption properties of surfaces are used in Chapter 4. Lipid membranes are used to obtain conditions where the fibrils are adsorbed strongly enough to be imaged by AFM but are sufficiently loosely bound to probe for mechanical properties such as bending rigidity and persistence length.

PART II: FIBRIL STRUCTURE

Research Question Part II:

How are monomers situated and packed within a fibril, investigated by combining different AFM modes and operation conditions?

The second part of this thesis focuses on the actual morphology of α-synuclein fibrils. Fibrils are investigated for their shape, height and periodicity, from which models for the inner structure are derived. Liquid and ambient air studies are used to determine where the C-terminal part is located in the fibril in Chapter 5 and morphological and mechanical data is combined to model how monomers are packed in a fibril in Chapter 6.

PART III FIBRIL MECHANICS

Research Question Part II:

How can we use AFM to derive mechanical properties of α-synuclein fibrils and what kinds of problems can we encounter?

To determine the mechanical properties of these amyloid fibrils it is important to first get more information on the fibril structure and second to find whether these fibrils behave very differently compared to other cell mechanical components such as actin or microtubulin. When these fibrils have a higher stiffness they could influence

cell motility or intracellular processes. Chapter 7 describes single-point nanoindentation experiments and compares these results with those obtained with fast nanomechanical mapping techniques. Fibrils are indented and moduli of elasticity are derived for the fibrils. In Chapter 8 we have investigated the impact of the fast nanomechanical mapping techniques operating at high frequencies on determining the elastic properties of soft complex materials. Nanoindentation is an easy method to probe very locally the mechanical properties of protein fibrils by applying strain perpendicular to the fibril axis. Since the protein fibrils are expected to be anisotropic, it is interesting to study the modulus of elasticity by applying strain in the direction of the fibril axis . To study this, the fibril needs to be suspended between two fixed points. In Chapter 9 the status of this study is outlined. This chapter also provides an outlook on these experiments, especially on how to combine these suspended fibril experiments with different frequencies to probe nanorheology of amyloid fibrils.

REFERENCES

1. Selkoe DJ. (2003) Nature 426:900-904
2. Soto C. (2003) Nat. Rev. Neurosci. 4:49-60
3. Dobson CM. (2003) Nature 426:884-90
4. Taylor JP, Hardy J, Fischbeck KH. (2002) Science 296:1991-95
5. Sipe JD, Cohen AS. (2000) J. Struct. Biol. 130:88-98
6. Nelson R, Sawaya MR, Balbirnie M, Madsen AØ, Riekel C, Grothe R, Eisenberg D. (2005) Nature 435:773-78
7. Sunde M, Serpell LC, Bartlam M, Fraser PE, Pepys MB, Blake CCF. (1997) J. Mol. Biol. 273:729-39
8. Ban T, Hamada D, Hasegawa K, Naiki H, Goto Y. (2003) J. Biol. Chem. 278:16462-5
9. Dobson CM. (2001) Philos. Trans. R. Soc. Lond. B. Biol. Sci. 356:133-45
10. Dill KA, Chan HS. (1997) Nat. Struct. Biol. 4:10-19
11. Hartl FU, Hayer-Hartl M. (2002) Science 295:1852-58
12. Goldberg AL. (2003) Nature 426:895-99
13. Bukau B, Weissman J, Horwich A. (2006) Cell 125:443-51
14. Ciechanover A. (1994) Cell 79:13-21
15. Balch WE, Morimoto RI, Dillin A, Kelly JW. (2008) 319:916-19
16. Selkoe DJ. (2004) Nat. Cell. Biol. 6:1054-61
17. Goedert M. (2001) Nat. Rev. Neurosci. 2:492-501
18. Lachmann HJ, Hawkins PN. (2006) Curr. Opin. Pharmacol. 6:214-20
19. Parkinson vereniging (april 2011) http://www.parkinson-vereniging.nl/parkinson.html
20. European Markets for Parkinson's Dissease Therapeutics 2009 Frost & Sullivan, London

21. Kandel ER, Schwartz JH, Jessel TM. (2000) Principles of neuroscience 4th edition. McGraw-Hill Companies, Inc
22. Schultz W. (2006) Proc. Natl. Acad. Sci. 103:1661-68
23. Davidson WS, Jonas A, Clayton DF, George JM. (1998) J. Biol. Chem. 273:9443-49
24. Wersinger C, Sidhu A. (2007) Biochemistry 44:13612-24
25. Alim MA, Ma Q, Takeda K, Aizawa T, Matsubara M, Nakamura M, Asada A, Saito T, Kaji H, Yoshii M, Hisanaga S, Ueda K. (2004) J. Alzheimers Dis. 6:435-22
26. Esposito A, Dohm CP, Kermer P, Bahr M, Wouters FS. (2007) Neurobiol. Dis. 26:521-31
27. Giehm L, Oliveira CLP, Christiansen G, Pedersen JS, Otzen DE. (2010) J.Mol.Biol. 401:115-33
28. Murphy DD, Rueter SM, Trojanowski JQ, Lee VM. (2000) J. Neurosci. 20:3214-20
29. Jao CC, Hedge BG, Chen J, Haworth IS, Langen R. (2008) Prot. Nat. Acad. Sci. 105:19666-71
30. Shvadchak VV, Falomir-Lockhart LJ, Yushchenko DA, Jovin TM. (2011) from: Lipids and Cellular Membranes in Amyloid Diseases pp 1-31
31. Reynolds NP, Soragnit A, Rabe M, Verdes D, Liverani E, Handschin S, Riek R, Seeger S. (2011) J. Am. Chem. Soc. 133:19366-75
32. Polymeropoulos MH, Lavedan C, Leroy E, Ide SE, Dehejia A, Dutra A, Pike B, Root H, Rubenstein J, Boyer R, Stenroos ES, Chandrasekharappa S, Athanassiadou A, Papapetropoulos T, Johnson WG, Lazzarini AM, Duvoisin RC, Di Iorio G, Golbe LI, Nussbaum RL. (1997) Science 276:2045-47
33. Zarranz JJ, Alegre J, Gomez-Esteban JC, Lezcano E, Ros R, Ampuero I, Vidal L, Hoenicka J, Rodriguez O, Atares B, Llorens V, Gomez Tortosa E, Del Ser T, Munoz DG, De Yebenes JG. (2004) Ann. Neurol. 55:164-73.
34. Kruger R, Kuhn W, Muller T, Woitalla D, Graeber M, Kosel S, Przuntek H, Epplen JT, Schols L, Riess O. (1998) Nat. Genet. 18:106-8.
35. Chartier-Harlin MC, Kachergus J, Roumier J, Mouroux C, Douay X, Lincoln S, Levecque C, Larvor L, Andrieux J, Hulihan M, Waucquier N, Defebvre L, Amouyel P, Farrer M, Destee A. (2004) Lancet 364:1167-69
36. Singleton AB, Farrer M, Johnson J, Singleton A, Hague S, Kacherus J, Hulihan M, Peuralinna T, Dutra A, Nussbaum R, Lincoln S, Crawley A, Hanson M, Maraganore D, Adler C, Cookson MR, Muenter M, Bapista M, Miller D, Blancato J, Hardy J, Gwinn-Hardy K. (2003) Science 302:841
37. Goldberg MS, Lansbury PT. (2000) Nat. Cell Biol. 2:E115-E119
38. Chiti F, Dobson CM. (2006) Annu. Rev. Biochem. 75:333-66
39. Fowler DM, Koulov AV, Balch WE, Kelly JW. (2007) Trends Biochem. Sci. 32:217-24
40. Kelly JW, Balch WE. (2003) J. Cell Biol. 161:461-62
41. Cohen AS. (1986) In Marrink, J., and Van Rijswijk, M. H. (Eds.), Amyloidosis, pp. 3–19, Nijhoff, Dordrecht.

42. Makin O, Serpell LC. (2005) FEBS Journal 272:5959-61
43. Khurana R, Ionescu-Zanetti C, Pope M, Li J, Nielson L, Ramirez-Alvarado M, Regan L, Fink AL, Carter SA. (2003) Biophys. J. 85:1135-44
44. Fändrich M, Meinhardt J, Grigorieff N. (2009) Prion 3:89-93
45. Kodali R, Wetzel R. (2007)Struct. Biol. 17:48-57
46. Kumar S, Udgaonkar JB. (2010)Current Science 98:639-56
47. Hoyer W, Antony T, Cherny D, Heim G, Jovin TM, Subramaniam V. (2002) J. Mol. Biol. 322:383-393
48. Petkova AT, Leapman RD, Guo Z, Yau W, Mattson MP, Tycko R. (2005) Science 307:262-265
49. Radovan D, Smirnovas V, Winter R. (2008) Biochemistry 47:6352-60
50. Raaij ME van, Segers-Nolten IMJ, Subramaniam V. (2006) Biophys. J.: Biophys. Lett. L96-L98
51. Adamcik J, Jung J, Flakowski J, De Los Rios P, Dietler G, Mezzenga R. (2010) Nat. Nanotech. 5:423-28
52. De Jong KL, Incledon B, Yip CM, DeFelippis MR. (2006) Biophys. J. 91:1905-14
53. Dong M, Hovgaard MB, Xu S, Otzen DE, Besenbacher F. (2006) Nanotechnology 17:4003-09
54. Kad NM, Myers SL, Smith DP, Smith DA, Radford SE, Thomson NH. (2003) Biophys. J. 88:1344-53
55. Anderson M, Bocharova OV, Makarava N, Breydo L, Salnikov VV, Baskakov IV. (2006) J. Mol. Biol. 358:580-596
56. Jansen R, Dzwolak W, Winter R. (2005) Biophys. J. 88:1344-53
57. Heise H, Hoyer W, Becker S, Andronesi OC, riedel D, Baldus M. (2005) Prot. Nat. Acad. Sci. 102:15871-76
58. Villar M, Chou H, Luhrs T, Maji SK, Riek-Loher D, Verel R, Manning G, Stahlberg H, Riek R. (2007) Prot. Nat. Acad. Sci. 105:8637-42
59. Paravustu AK, Leapman RD, Yau W, Tycko R. (2008)Prot. Nat. Acad. Sci. 105:18349-54
60. Wei G, Jewett AI, Shea J. (2010) Phys. Chem. Chem. Phys. 12:3622-29
61. Pellarin R, Schuetz P, Guarnera E, Caflisch A. (2010) J. Am. Chem. Soc. 132:14960-70
62. Knowles TPJ, White DA, Abate AR, Agresti JJ, Cohen SIA, Sperling RA, De Genst EJ, Dobson CM, Weitz DA. (2011) Proc. Nat. Acad. Sci. 108:14746-51
63. Xue W-F, Homans SW, Radford SE. (2008) Proc. Natl. Acad. Sci. USA 105:8926-31
64. Goldsbury C, Kistler J, Aebi U, Arvinte T, Cooper GJ. (1999) J. Mol. Biol. 285:33-39
65. Kellemayer MSZ, Karsai, A, Benke M, Soos K, Penke B. (2008) Proc. Natl. Acad. Sci. 105:141-44
66. Hoyer W, Cherny D, Subramaniam V, Jovin T. (2004) J. Mol. Biol. 340:127-39
67. Zhang L, Zhong J, Huang L, Wang L, Hong Y, Sha Y. (2008) J. Phys. Chem. B 112:8950-54

CHAPTER 2

Nanomechanical properties of single amyloid fibrils

Amyloid fibrils are traditionally associated with neurodegenerative diseases like Alzheimer's disease, Parkinson's disease or Creutzfeld-Jacob disease. However, the ability to form amyloid fibrils appears to be a more generic property of proteins. While disease-related, or pathological, amyloid fibrils are relevant for understanding the pathology and course of the disease, functional amyloids are involved, for example, in the exceptionally strong adhesive properties of natural adhesives. Amyloid fibrils are thus becoming increasingly interesting as versatile nanobiomaterials for applications in biotechnology.

In the last decade a number of studies have reported on the intriguing mechanical characteristics of amyloid fibrils. In most of these studies atomic force microscopy and atomic force spectroscopy play a central role. AFM techniques make it possible to probe, at nanometer length scales, and with exquisite control over the applied forces, biological samples in different environmental conditions.

In this review we describe the different AFM techniques used for probing mechanical properties of single amyloid fibrils on the nanoscale. An overview is given of the existing mechanical studies on amyloid. We discuss the difficulties encountered with respect to the small fibril sizes and polymorphic behavior of amyloid fibrils. Especially the different conformational packing of monomers within the fibrils leads to a heterogeneity in mechanical properties. We conclude with a brief outlook on how we can use the knowledge of these mechanical properties of the amyloid fibrils can be exploited in the construction of nanomaterials from amyloid fibrils.

Sweers KKM, Bennink ML, Subramaniam V, accepted for publication in Journal of Physics: Condensed Matter.

INTRODUCTION

The term amyloid fibril was first introduced in 1854 and is usually associated with neurodegenerative diseases like Alzheimer's disease, Parkinson's disease or Creutzfeld-Jacob disease [1,2]. More recently, the ability to form amyloid fibrils was found to be a generic property of proteins [3,4]. Indeed, common food proteins, like β-lactoglobulin or ovalbumin, have the ability to form amyloid fibrils [5,6]. Amyloid is a general term for protein aggregates with the following three characteristics: (1) the fibrils are around 10 nm in diameter, (2) they bind to dyes such as Thioflavin T, and (3) the fibrils consists of cross β-strands stacked perpendicular to the fibril axis and exhibit intermolecular hydrogen bonds [1,2,7-9].

Disease-related amyloid fibrils are relevant for understanding the pathology, origin and progression of the disease. Moreover, amyloid fibrils, whether formed from disease-related or other proteins, are becoming increasingly interesting for applications in nanobiotechnology [10]. Most studies till now have focused on the morphological properties of the amyloid fibrils such as fibril length and fibril height, using technologies such as atomic force microscopy imaging or transmission electron microscopy. Other studies have addressed the twisting characteristics of amyloid fibrils [11,12]. Nuclear magnetic resonance or x-ray diffraction methods have been used to investigate the packing and assembly of monomer units within amyloid fibrils [8,13,14]. Despite a rather large body of literature (reviewed, for example in Gosal et al. [15]) a number of open questions remain regarding the structure of amyloid fibrils.

One particular characteristic observed with many amyloid fibrils, and which severely complicates the interpretation of the studies, is polymorphism. Polymorphism refers to the tendency of amyloid-forming proteins to form a variety of fibrils all having different structural characteristics [16-18]. An alternative method to shed some light on these open questions is to study the mechanical properties of these nanostructures. Mechanical properties of fibrils are often directly linked to the structure. This relation makes it possible to retrieve, from mechanical characteristics, information on shape and packing of the individual monomers within a fibril.

In the last decade a vast number of studies have reported on obtaining the mechanical characteristics of amyloid fibrils. Understanding the mechanical characteristics of disease-related amyloid fibrils may yield insight into the formation and structure of amyloid nanostructures, and eventually into the mechanisms of cellular toxicity. Amyloid fibrils are found to be stiffer than cytoskeleton components such as actin filaments (1.8 GPa) [19,20], microtubules (600 MPa) [21,22] or intermediate filaments (6.4 MPa) [23]. So although the fibrils themselves often appear not to be toxic compared to the

intermediate oligomeric aggregation states, the mechanical properties of amyloid fibrils could interfere with cytoskeletal dynamics. The modulus of elasticity values of amyloid fibrils are in the range of collagen fibrils (1-5 GPa) [24,25], which suggest that in the extracellular space (where for example, Aβ fibrils are found), these fibrils could have fewer mechanical consequences for cell motility.

Amyloid fibrils are also increasingly found naturally in functional roles. Recently, over 30 human peptide hormones were found that are stored in amyloid-type granules for long-term use [26]. This could be translated into a system to overcome the short-term delivery problems of drugs by using amyloid as a controlled drug release system [27]. Bacteria, like Salmonella and Escherichia coli, and algae use functional amyloid to modulate surface adhesion [28,29]. The interest in mechanical properties for these kinds of amyloid is mainly in their adhesive properties. Sullan et al. studied the adhesive properties of polymerized barnacle glue, consisting also of amyloid, which is a large contributor to the fouled areas on marine ship hulls [30]. Deeper insights into the specific mechanical properties of amyloid could be used to create new surfaces with a monolayer of amyloid fibrils with specific adhesive properties.

Due to the self-assembly property of amyloid fibrils, these nanostructures are also interesting as templates to create filaments of other materials that do not have this capability. Many protein peptides can be functionalized with, for instance, fluorescent dyes or metal nanoparticles to create functionalized wires. For instance, Scheibel et al. covalently linked gold particles to fibrils formed by a modified NM Sup35 (N-terminal and middle region of yeast prion Sup35) peptide. These coated fibrils displayed conductive properties [31]. Also diphenylalanine fibrils are of interest for this purpose. Because of the hollow core, these fibrils can be functionalized inside and outside creating a coaxial type nanowire [32]. Aside from the light and electron transport properties, the need to know mechanical characteristics is important when these nanowires are used in the construction of larger light-harvesting complexes or nano-electronics.

Atomic force microscopy and atomic force spectroscopy play a central role in most existing studies of mechanical properties of amyloid fibrils. Atomic force microscopy allows probing biological samples with very low and controlled forces in different environmental conditions. Three different approaches can be distinguished (Figure 1). The first approach is nanoindentation, where the AFM tip acts as an indenter. The modulus of elasticity can be extracted from the force-displacement curve using elastic contact models. The second approach involves bending experiments in which the amyloid fibril is suspended over a channel and the AFM tip is used to bend the fibril. In the third and last method, amyloid fibrils are deposited on a surface after which they are imaged. From these images the bending rigidity can be determined by analyzing the curvature

of the individual fibrils using statistical mechanical theory of semi-flexible polymers, for instance with end-to-end distances.

In this review we first briefly introduce the different AFM-based methods for probing mechanical properties of single amyloid fibrils. We give an overview of the existing studies so far, in relation to all the different challenges (like small size, anisotropy and heterogeneity) are associated with these AFM-based mechanical studies of nanoscale fibrils.

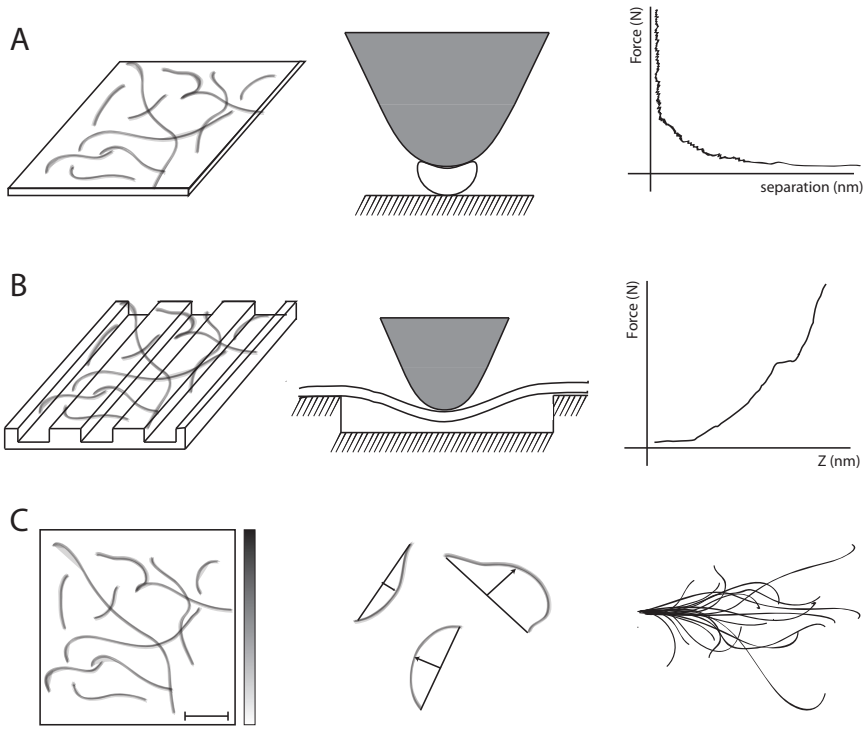

FIGURE 1; Overview of three different AFM-based methods to measure mechanical properties of single fibrils. Panel (A) depicts the AFM-based nanoindentation to probe for spring constants or stiffness values with nanometer-scale spatial localization. The tip acts as an indenter and pushes into the fibril. This results in a force-distance curve that can be analyzed for elastic properties. Panel (B) shows bending experiments, which use the same AFM configuration as for nanoindentation, only the fibrils are suspended on channels to determine modulus of elasticity along the fibril axis. The force curve displays the elastic properties and eventually a breaking point. (C) Here the fibril mechanical properties are derived from the 2D AFM images of the individual fibrils. The fibrils are traced and a contour of each fibril is generated. From the curvature of the contour, the bending rigidity of the fibril can be calculated using statistical mechanical theory of semi-flexible polymers by determining the distance between the midpoint of the fibril to the straight rod ground state. Comparing groups of fibril contours formed by different proteins could already shed light on different mechanical properties.

METHODS FOR PROBING NANOMECHANICAL PROPERTIES OF AMYLOID FIBRILS

In 1986 the first atomic force microscope (AFM) was realized as a variant of the scanning tunneling microscope [33,34]. In AFM a 3D reconstruction of the sample topography is made by scanning the sample. The sample is moved in x, y and z direction with respect to the AFM tip, sample-scanning method, or vice versa in a tip-scanning set up. The AFM tip is at the end of a leaf spring or cantilever that bends according to the sample topography and interaction forces (like short-range van der Waals forces, or long-range electrostatic forces). This bending of the cantilever, and thus interaction between tip and sample, is monitored with a laser beam reflected from the back of the cantilever onto a position sensitive photodiode. Since the AFM is a force-measuring technique, it is not only an excellent technique for analyzing morphological parameters by creating 3D topography maps, but is also very suitable for determining mechanical characteristics which can provide additional insights into the structure and assembly of amyloid fibrils.

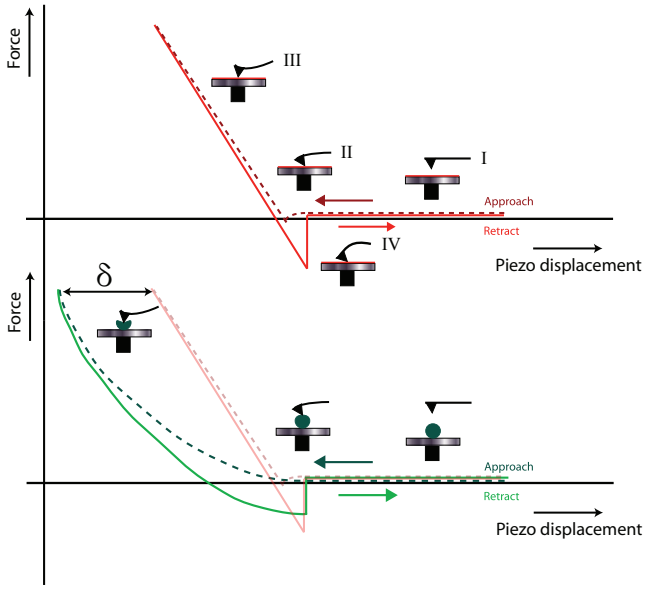

FIGURE 2; Typical approach and retract curve. Different regions are highlighted: where the tip is above the sample (I), the tip snaps in onto the sample due to Van der Waals forces (II), the tip presses on the sample leading to cantilever deflection (III), and finally, when the tip is retracted again, the tip sticks to the sample due to adhesion forces before finally snapping free (IV). The small difference between the approach and retract curve is called contact hysteresis which is caused by friction effects between the tip and the sample [35]. The red curve indicates a force-distance curve on a hard reference sample and the green curve represents indentation on a soft sample. The difference δ between both curves is the indentation.

NANOINDENTATION

Nanoindentation on the AFM is done by atomic force spectroscopy where the ability of the AFM to precisely measure the interaction forces between the tip and sample is used. In nanoindentation mode the AFM tip approaches and is pushed into the sample until a predefined force is reached; at this point the tip is retracted again. During this complete cycle the position of the tip as well as the force exerted on the cantilever are accurately monitored, resulting in a force-distance curve (Figure 2). For most biological samples, the AFM tip acts as a stiff indenter, and can therefore be used to measure the mechanical properties of the sample. The stiffness of the sample can be extracted from the part of the curve where the tip is in contact with the sample (Figure 2).

CONTACT MECHANICS MODELS

Contact mechanics models are needed to relate the stiffness extracted from the force curves to an actual modulus of elasticity. There are several contact models to analyze force curves generated by a nanoindentation experiment. We will briefly discuss here three models, namely the Hertz, JKR and DMT models, which mathematically looks like:

$$Hertz: F = \frac{4}{3} E^* \sqrt{R} \delta^{3/2}$$

$$DMT: F = \frac{4}{3} E^* \sqrt{R} \delta^{3/2} - 2\pi R\gamma$$

$$JKR: F = \frac{9}{4} E^* \sqrt{R} \delta^{3/2} \cdot \Delta\gamma\pi$$

$$\frac{1}{E^*} = \frac{1-\upsilon_m^2}{E_m} + \frac{1-\upsilon_i^2}{E_i}$$

where F is force, δ is indentation, R tip radius and E* the reduced elastic modulus and γ the work of adhesion, defined as in Eq (1) , The reduced elastic modulus is comprised of the modulus of elasticity and Poisson ratio of the to be indented material, E_m and ν_m, and the modulus of elasticity and Poisson ratio of the indenter, E_i and ν_i, here the AFM tip. Ideally, the indenter has an infinite modulus of elasticity and a low Poisson ratio, which renders the second term zero.

The Hertz model assumes a non-adhesive contact between two contacting bodies. In case there is adhesion between the two bodies the JKR and DMT model are most often used for the interpretation of nanoindentation data. The DMT model assumes the contact area between the tip and the material as in the Hertz model, but includes an additional constant adhesion term, representing adhesive forces outside the contact area. This means that the contact profile remains the same but an additional adhesive

force is added outside the area of contact, so the curve is identical to that of the Hertz model with an offset (adhesion) in force. In contrast to the DMT model, the JKR model assumes adhesion inside the area of contact [36-38].

In order to determine the elasticity modulus, irrespective of the model used, the contact area must be determined. In the equations above, the contact area is calculated assuming a spherical tip with radius R, assuming the contact to be modeled by that of a sphere touching an infinitely large plane. Since the diameter of a typical amyloid fiber is about 10 nm, which is about the same order of magnitude as the tip radius, this condition is not valid. Using an equivalent tip radius in the above equations can compensate for this point. The equivalent tip radius, R_e, is defined by Equation 2, in which the AFM tip is assumed to be a sphere with radius R_t indenting an infinitely long cylinder, that represents the fibril, with radius R_f:

$$R_e = \sqrt{\frac{\left(R_t^2 R_f\right)}{\left(R_t + R_f\right)}}$$

SURFACE PROPERTY MAPPING TECHNIQUES

As explained in the previous section, nanoindentation can be performed at one specific point of the sample in order to locally probe the mechanical properties with nanometer resolution. It is also possible to perform nanoindentation in a raster-pattern such that mechanical properties, like modulus of elasticity, adhesion or energy dissipation are determined for each pixel of a surface. This mode is known as force-volume mode and creates a set of images for all parameters [39]. The force-volume mode is very helpful in mapping the heterogeneous properties of amyloid fibrils. However, with each individual nanoindentation experiment taking about 1 second, this method can be very time consuming. Recently novel methods have been developed to probe for mechanical properties at much higher speeds, which significantly decrease the imaging time [40-42]. Examples of such methods are Harmonic Force Microscopy, Pulsed Force Microscopy, or Peakforce QNM. Peakforce QNM is an imaging mode in which the cantilever is oscillated at a frequency of 1 kHz, with each oscillation resulting in a single force-distance curve. From this force-distance curve elastic parameters can be extracted. The feedback is applied on the maximum force that is applied to the sample, ensuring the sample is probed with the same force at each position. HarmoniX is based on the nonlinear dynamic behavior of a cantilever in tapping mode due to repulsive and attractive forces caused by the specific material characteristics of the sample acting on the tip [43,44]. By using cantilevers on which the tip is positioned off-center, the interaction between the tip and sample also induces a torsional mode. This torsional mode acts as a high bandwidth force sensor in which all the higher harmonic signals

from the vertical deflection can be measured. From this a force-distance curve can be reconstructed, and mechanical properties can be extracted.

SINGLE MOLECULE SPECTROSCOPY

One aspect that has not been extensively discussed above is the use of atomic force spectroscopy for single molecule pulling. Single molecule force spectroscopy is frequently used to determine the fold of single proteins and peptides, see for reviews [45,46]. Force curves can predict whether amino acid chains are folded, for instance in β-sheet conformation or unstructured. Further, the persistence length of amino acid chains can be determined. Although, this approach does not yield results on the mechanical properties of full-length assembled amyloid fibrils, it can be applied to provide insight into the intermolecular forces involved in fibril assembly, and possibly the folding transition it undergoes as a protein monomer is assembled into the fibril structure.

In the context of amyloid fibrils, when the AFM tip is specifically or aspecifically bound to individual monomers within the fibril, these monomers can be pulled out of the fibril. This nanoscale pulling experiments gives a force-distance curve, potentially with different steps that could indicate β-sheet unzipping, and eventually leads to a final rupture force [28,47].

SINGLE FILAMENT BENDING EXPERIMENTS

AFM-based nanoindentation only probes very local mechanical properties by exerting a force in a direction perpendicular to the amyloid fibril axis. Amyloid fibrils, however, have an anisotropic structure and are therefore expected to display anisotropic mechanical properties. To study the mechanical properties along the fibril axis a different type of experiment must be performed, for example, a bending experiment. Here, an individual amyloid fibril is suspended over a micro- or nanometer sized channel and the AFM is used to accurately measure the force needed to bend the freely suspended part of the fibril.

Nanoscale fibrils that are supported over channels can be modeled as a simple supported beam in which the force from the AFM tip is assumed to be a single point load P in the middle of the beam. Depending on the boundary conditions, there are two models that can be used. The first model is that of a simple supported beam. As the load is applied to the beam, the beam can bend and freely rotate on the points where it is supported. However, amyloid fibrils are known for their strong adhesive properties suggesting that this boundary condition is probably not valid. The second model is that of a statically indeterminate beam, where both ends of the beam are fixed. Assuming that the amyloid fibril is firmly attached to the edges of channels, this boundary condition would be the appropriate one.

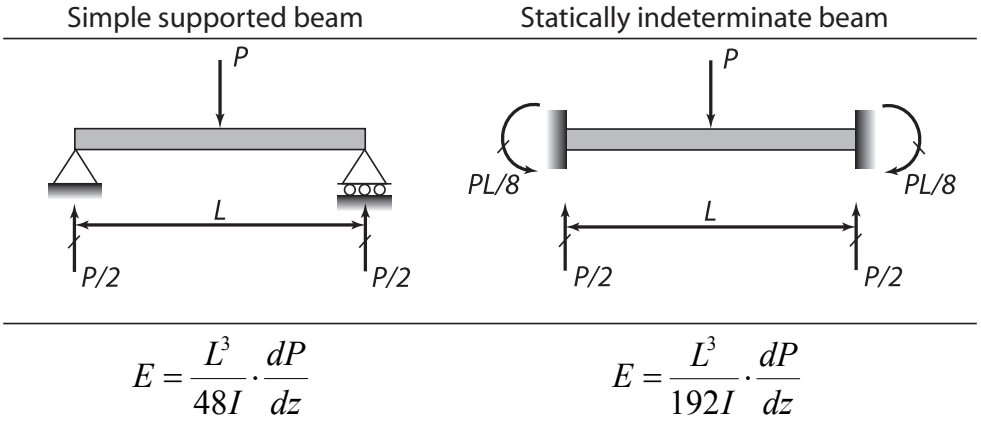

$$E = \frac{L^3}{48I} \cdot \frac{dP}{dz} \qquad E = \frac{L^3}{192I} \cdot \frac{dP}{dz}$$

FIGURE 3; Supported beam models for AFM bending experiments. Simple supported beam with at one side a pin support and at the other a roller support (left) and a statically indeterminate beam fixed at both ends (right), with the corresponding formulae for modulus of elasticity.

These two models are used for larger filaments like collagen [24], para-hexaphenylene nanofibers [48] or elastic fibers [49]. In these experiments typical channel widths were in the 1 to 10 μm range. For filament sizes that are larger than the AFM tip, as is the case for collagen fibers, it is valid to consider the size of the contact area as a point load. However, for amyloid fibrils, which are small compared to the AFM tip size, and are to be bent over much smaller channels (range of 50-200 nm), the size of the contact area can no longer be considered a point load. This load becomes a distributed load that is dependent on the tip size and shape. Obtaining a mathematical representation for this distributed load depending on the tip-shape and the small interaction forces that are involved can be challenging.

STATISTICAL ANALYSIS OF THERMAL FLUCTUATIONS

As mentioned above, bending experiments are very challenging for amyloid fibrils both from an experimental point of view and in the analysis and interpretation of the data. Another way that the elastic properties of amyloid fibrils reveal themselves is through the shape of the fibrils, and in particular by the curvature they exhibit when in solution or on a surface. By making topography images of these fibrils using either contact or tapping mode AFM, the fibril contours can be traced either manually or by using a tracing algorithm. From these traces it is possible to determine the end-to-end distance of a fibril, and its curvature or the deviation from a straight segment. Using statistical mechanical theory of semi-flexible polymers, it is possible to derive the bending rigidity or flexural rigidity of the amyloid fibril. This bending rigidity is proportional to the persistence length of a filament, which is the length of a filament over which

thermal bending becomes appreciable.

There are several approaches to measure persistence length or bending rigidity. For instance, the end-to-end distance can be measured. When any bending has occurred, this length is always smaller than the contour length of the filament. When the contour length of the filament is much smaller than the persistence length (L_p), the persistence length can be estimated by the fluctuations in shape [50]. This method is often used in case of amyloid fibrils. The bending rigidity (κ) of the semiflexible amyloid fibrils can be derived from the average magnitude of the thermally-induced shape deviations from a straight line connecting the end points [51-53] according to the following equations:

$$k_B T \times \frac{L^3}{48\langle v(x)^2 \rangle} \leq \kappa \leq k_B T \times \frac{L^3}{24\langle v(x)^2 \rangle}$$

where kB is the Boltzmann constant, T the temperature in Kelvin, L the contour length of the fibril segment and v(x) is the distance from the midpoint of the fibril segment to the secant line of the fibril segment. Eq(3) provides two outer limits for the bending rigidity, representing a situation in which the fibrils are irreversibly trapped when deposited onto the surface and a situation in which the fibrils are thermally equilibrated on the surface before they adhered more strongly.

One important aspect of these calculations is the choice of fibrils in the 2D image. One should only choose filaments which do not cross other filaments or particles on the surface. Crossing other fibrils or particles influences the shape of the fibril contour, subsequently affecting the results of the analysis.

MECHANICAL PROPERTIES OF AMYLOID FIBRILS

The number of mechanical studies on amyloid fibrils probed with AFM is rapidly increasing. These studies report on bending rigidities, moduli of elasticity, stiffness, and rupture forces of individual monomers within the fibrils, and often link these properties to structural information.

When determining mechanical properties with an AFM, all possible approaches are accompanied by their own specific calibration issues. Most important is the cantilever choice and cantilever stiffness calibration. For nanoindentation, the highest sensitivity is achieved if the spring constant of the cantilever is in the same range as the spring constant of the sample. The calibration of this spring constant can be done using the thermal noise method, which has associated errors of around 5%, or response methods like added mass method (10-20% error) [54-56]. Furthermore, for all calibration

methods the deflection sensitivity is needed, and also gives rise to a small error of 2% [55]. The accuracy of determining the tip radius can also influence the results greatly. All these issues have been described previously [56]. The only method that is relatively insensitive to these calibration issues is the bending rigidity determination approach, although this method also relies on assumptions like whether the samples are able to thermally equilibrate on the surface.

In addition to the experimental considerations mentioned above, specific structural characteristics of amyloid fibrils, such as size, polymorphism, and anisotropy, influence the mechanical properties of amyloid fibrils. In the next section we focus below on the consequences of these parameters and of environmental conditions on the accurate determination of amyloid mechanical properties.

AMYLOID FIBRIL SIZE

One of the most significant challenges of performing nanoindentation experiments on amyloid fibrils is the small diameter (~10 nm) of these fibrils. Firstly, the area of contact used in the elastic contact models (Eq. 2) is only correct if the indentation takes place precisely on top of the amyloid fibril. An accurate XY-feedback system is needed to precisely position the tip above the fibril. If this is not done correctly, the measurements will give incorrect results, as we have recently shown in a study using HarmoniX, which revealed an increased modulus of elasticity near the edges of fibrils [56]. Secondly, when performing nanoindentation measurements on these nanoscaled structures, whether by means of single-point experiments or the newly introduced surface property mapping techniques, an important issue to consider is the effect of finite sample thickness. These effects come into play when the sample starts to compress and the AFM cantilever 'feels' not only the sample but also the underlying substrate up to a point where the sample is completely compressed and only the substrate accounts for the signal. In the initial 20% of the total height of a sample these effects are thought to be negligible when the sample is relatively large compared to the tip [30]. However, when indenting amyloid fibrils, this 20% value is only ~2-3 nm, which makes it more difficult to analyze the indentation curves. The AFM tip is approximately the same size as or larger than the fibril. It is difficult to indicate the precise point of contact and indeed to determine whether actual contact has occurred, or if the signal measured is only due to long-range repulsive or attractive forces. Akhremitchev et al have developed a correction factor depending on the sample size, sample modulus of elasticity, and the maximum applied force (Figure 4) [57].

Guo et al. used this method to correct for finite sample thickness effects while determining the modulus of elasticity of insulin fibrils, which decreased the elastic modulus

one order of magnitude from 141 MPa to only 14 Mpa after correction [58]. Others also adopted this correction method, for instance when measuring the modulus of elasticity of different types of poly(ValGlyGLyLeuGly) fibrils (3.7-7.1 MPa) and bovine elastin fibrils (1.1 MPa) [59]. Here the correction factor was ~4-5 due to the softness of the sample; however also stiffer amyloid fibrils made of the protein α-synuclein did show a small decrease in the modulus of elasticity after correction for finite sample thickness effects to 1.3 GPa (correction factor ~1.3) [56].

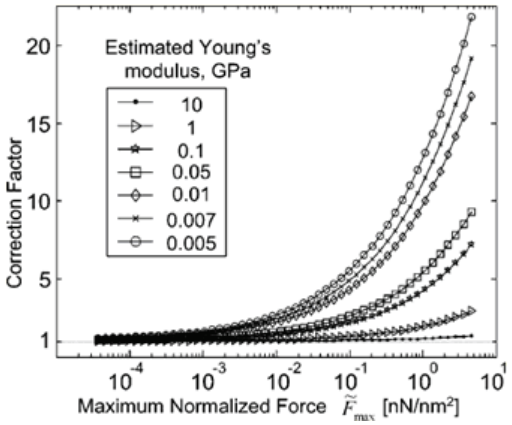

FIGURE 4; Correction factors for the finite sample thickness effect. The graphs show the dependence of the correction factors on the maximum normalized force. The correction factors were calculated for several samples with different Young's moduli. An apparent value of the Young's modulus for each line is indicated in the insert. [With permission from ref. 58]

The bending experiments are also challenging for these small length scale fibrils. As discussed in the instrumental section the load applied on the fibril is probably not a point load but a distributed load that is challenging to model. Also the channel size plays a role; when a fibril is rather flexible or the channel is very wide, it is often easy for adsorption forces to pull the fibril in to the channel. We attempted several channel patterned surfaces for this purpose and often observed fibrils which were aligned with the channels or, when crossed the channels, were completely sunken in to the channels. When the fibril completely sinks into the channel, or follows the contours of the channel, it is no longer possible to perform the bending experiments. Successful bending experiments on insulin fibrils have been performed on gold patterned surface with channels between 50 and 100 nm [53]; these surfaces are not commonly available and require special fabrication using advanced strategies.

AMYLOID FIBRIL STRUCTURE

The ultrastructure of amyloid fibrils also plays a significant role in determining the

modulus of elasticity. For the bending experiments and bending rigidity method the moment of inertia is required to determine the modulus of elasticity. This moment of inertia is dependent on the cross-sectional area of a fibril. Amyloid fibrils display a large degree of polymorphism, or variation in their morphologies. Earlier studies suggested that the hierarchically twisted filament model could be a generic model for all amyloid [60]. However, recently also twisted, laterally-associated filaments have been reported for β-lactoglobulin amyloid fibrils. These fibrils show increasing persistence lengths when the number of filaments increases, from 1 μm for a single filament to almost 4 μm for 5 filaments [61]. The packing of filaments within a fibril could account for a large difference in results. Adamcik et al. already described a linear dependence of the moment of inertia on fibril height when the number of filaments increases. In Figure 5A we show an example of a 6-fold difference between moments of inertia when a fibril is assumed to be a circular rod or consists of 4 laterally-associated filaments which twist. Aside from the packing, the conformation of the monomer also plays a role. For simplicity many studies use a circular conformation for the moment of inertia [24,49,53,61]. However, β-sheet folded proteins are probably not circular. For α-synuclein the fold is believed to be trapezoid shaped [13]. A roughly two-fold change in moment of inertia is found depending on whether the primary sequence of the monomer is assumed to follow this trapezoid shape or a circular shape (Figure 5B) [13,62].

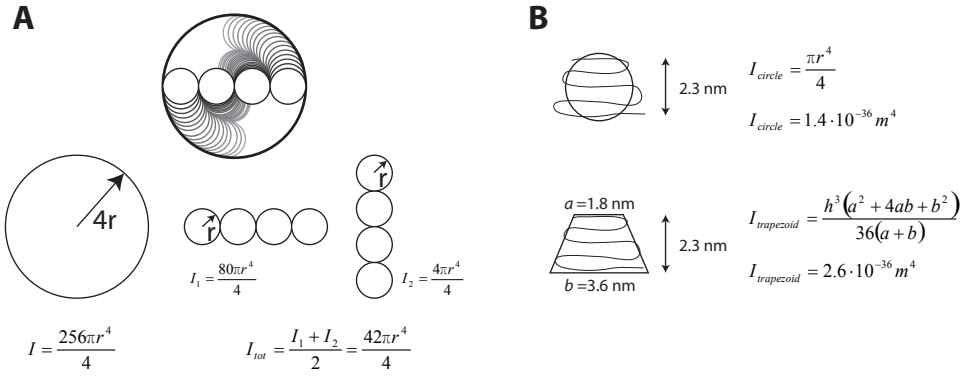

FIGURE 5; Examples of cross-sections of amyloid fibrils with their corresponding second moments of inertia. (A) Difference between moments of inertia when a fibril is assumed to be a circular rod or consists of 4 lateral associated filaments that twist results in a roughly 6-fold difference in moment of inertia. (B) Shape of α-synuclein monomer with 5 in size increasing β-strands [13]. A circular shape reduces the moment of inertia roughly 2 fold when the same dimensions, like a monomer height of 2.3 nm, are used as for a trapezoid shape.

Several studies have demonstrated that amyloid fibrils can demonstrate significant variations in morphologies (polymorphism), see for reviews references [16-18,63]. $A_{\beta 1\text{-}40}$ fibrils for instance, show both twisted fibrils and laterally associated filaments

depending on the aggregation conditions [11]. However, morphological differences can also lead to differences in mechanical characteristics. Aβ fibrils comprised of different peptide length monomers give different fibrils with different rupture forces [64,65]. Fibrils comprised of α-synuclein can lead to curly fibrils with a persistence length of 0.17 μm after several filtration-like steps during aggregation or, when the aggregation is not interfered with, to straight fibrils with persistence lengths of up to 140 μm [66]. β-lactoglobulin fibrils aggregated with or without the presence of ethanol also exhibit very different persistence lengths (2.3 μm versus 0.003 μm respectively) [67]. Also, β-lactoglobulin fibrils made with different agitation methods lead not only to morphological differences, but also differences in rupture forces measured by single molecule force spectroscopy [68].

Sometimes, one aggregation reaction produces multiple fibril species. These fibril species can have similar mechanical properties, like periodic and non-periodic α-synuclein fibrils that display the same bending rigidity values of around $1.5x10^{-24}$ Nm^2 [62]. However protofibrils formed by HypF-N did show two populations with different bending rigidities of $2.9\pm0.1x10^{-28}$ Nm^2 and $4.2\pm0.4x10^{-29}$ Nm^2 with no distinct morphological differences. This observation indicates that mechanically different protofibrils can exist, each of which could further exhibit differences in aggregation tendencies [69].

AMYLOID FIBRIL HETEROGENEITY AND ANISOTROPY

The twisted morphological feature of amyloid fibrils, already discussed above, could lead to anisotropic and heterogeneous characteristics in the mechanical properties. For collagen fibrils it has already been shown that the ribbon-like morphological characteristics also display an almost two-fold difference in modulus of elasticity (1.2 GPa for gap region and 2.2 GPa for the higher overlap region) [70]. Simple AFM contact mode sideways scratching of α-synuclein fibrils on a surface already revealed that twisted fibrils were weaker at the twist sections [71]. Nanoindentation on glucagon fibrils also revealed different moduli of elasticity at different sections along the twist. The corresponding force-volume images showed that the fibril peaks were more compliant compared to the troughs. [72]. The recently introduced high-speed surface property mapping techniques facilitate the analysis of heterogeneous features. However, first results with Peakforce and HarmoniX did not reveal differences along the twist of α-synuclein fibrils [56]. Also, peakforce tapping on β-lactoglobulin did not reveal differences along the twist that were not induced by the underlying substrate [73]. Mechanical anisotropy of amyloid fibrils refers to a difference in mechanical properties when measured either radially or axially. Nanoindentation probes for mechanical properties perpendicular to the fibril axis, while bending experiments yield values for the axial direction. For

insulin fibrils the nanoindentation measurements resulted in values with an average of 14 MPa [58] while bending experiments or bending rigidity measurements from 2D images resulted in values up to 3.3 and 6.3 GPa respectively [53]. Nanotubes formed by the diphenylalanine peptide display similar differences between the axial modulus of elasticity compared to the elasticity measured radially. However, this difference was less pronounced compared to insulin. Nanoindentation measurements resulted in a spring constant of 160 N/m for the tubes which was calculated with finite element analysis to correspond to a modulus of elasticity of ~19 GPa [74]. However, bending experiments on similar tubes gave an average modulus of elasticity of 27 ± 0.4 GPa [75]. A study of poly(ValGlyGlyLeuGly) fibrils freely suspended over two underlying fibrils for bending experiments and indentation studies on the same fibril resting on the surface also showed a difference in axial stiffness compared to the radial stiffness [76].

ENVIRONMENTAL CONDITIONS

Environmental conditions are often of importance in AFM studies. Morphological features like size and periodicity already appear to change upon drying or when using different scanning buffers [12,77]. The high modulus of elasticity values for amyloid fibrils compared to other biological materials, for example dragline silk, which has values up to 10 GPa [78], already indicate a tight, densely-packed, fibril core. This suggests that one could expect little difference between modulus of elasticity values measured by nanoindentation in air or liquid. This hypothesis is verified by Peakforce QNM measurements on the same α-synuclein fibrils in air and liquid, which did not result in significant differences [56].

For bending rigidity measurements from topography images, the surrounding medium will influence the interaction of the fibrils with the surface. This interaction will determine whether the fibrils on the surface are thermally equilibrated or whether they are irreversibly trapped. More specifically the ion concentration determines the strength of this interaction. When imaging DNA in solution the Mg^{2+} ion concentration is responsible for the ability of DNA to move on the surface. This ability to move is important to make sure that the sample is in thermal equilibrium for persistence length analyses [79]. However, in the case of amyloid fibrils with their stron g adhesive properties this is difficult. Several studies claim that amyloid fibrils are in thermal equilibrium on the surface (often mica surfaces) [51,53]. A study on HypF-N fibrils also indicated that the fibrils equilibrate after deposition on mica [69]. Recent work of bending rigidity analysis of alpha-synuclein fibrils on fluid phase lipid membranes compared to the same fibrils on mica supports these claims. The fibrils did not strongly bind to the membrane and were still able to move around, clearly suggesting that they are thermally equilibrated on the surface when imaged. Mechanical analyses did not show differences in bending rigidity

values between the fibrils on mica and the loosely bound fibrils on the membrane [80]. Also, imaging amyloid fibrils in ambient air environment did not give different bending rigidity values compared to fibrils imaged in solution [62].

TOWARDS HIGHER ORDERED STRUCTURES

The increasing interest in mechanical properties of amyloid fibrils is summarized in Figure 6, from a recent article by Knowles and Buehler [81]. This Figure collates all available values of bending rigidities and moduli of elasticity of amyloid and compares these mechanical characteristics to other biological and non-biological materials. As shown in panel (B) the range of modulus of elasticity values found for amyloid fibrils is rather large. This is most likely attributable to the different approaches used to calculate these values, and reflect, for instance, the anisotropic differences that are shown by nanoindentation and bending measurements (section 3.3). Also, polymorphism results in differences in elastic moduli due to different conformations within the fibrils leading to different moments of inertia (section 3.2). The bending rigidities depicted in panel (A) are experimentally less susceptible to calibration errors and small size issues. It is most instructive to compare bending rigidities of amyloids to other biological structures in their native form. Mechanical characteristics of amyloid could lead to new insights in disease-related processes, for instance by directly relating the mechanical properties of amyloid to cytoskeleton properties. However, the nanomechanical properties of amyloids are also related to amyloid growth kinetics. It has been suggested that longer fibrils have a greater propensity towards fracture [82, 83]. This creates more fibril ends increasing the overall aggregation reaction by generating new growth sites due to fragmentation [84]. The Knowles group has treated in a comprehensive theoretical manner, the issue of nucleated polymerization with secondary pathways [85-87]. An experimental study has demonstrated that prion protein fibrils with a lower fracture rate can lose their ability to propagate as prions [88]. However, prion fibrils with a high propensity towards fracture propagate more effectively, and could result in a more rapid onset of disease symptoms. Furthermore, mechanical characteristics in the form of moduli of elasticity or stiffness are useful to investigate the use of amyloid fibrils for nanomaterials, especially for construction of larger, more complex, supramolecular assemblies.

The propensity of protein peptides to self-assemble into amyloid fibrils crosses over into self-assembly of fibrils into higher ordered structures like gels, crystals or films. The mechanical properties of these higher ordered assemblies depend on the mechanical properties of the single amyloid fibrils as well as on the packing density, packing structure, and cross linking of these fibrils or proteins within the structure. Insulin crystals display a modulus of elasticity measured with nanoindentation of 164 MPa, a

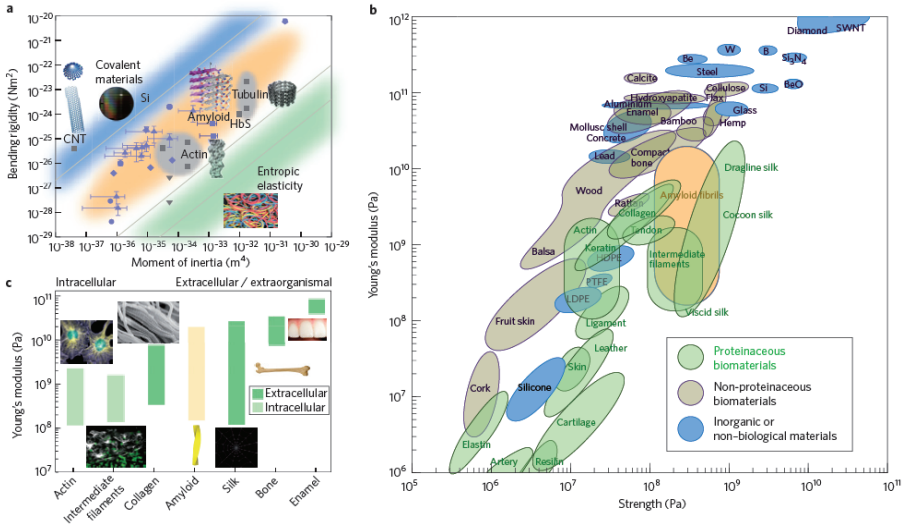

FIGURE 6; Mechanical properties of amyloid fibrils in comparison to biological and inorganic or non-biological materials. Panel A shows bending rigidities versus moments of inertia for materials with covalent bonds (blue region), non-covalent bonds such as hydrogen bonds (orange region) and weak non-covalent interactions (green region). Blue and grey symbols are values for different type of amyloid fibrils measured experimental or from simulations. Panel B indicates modulus of elasticity versus strength for different types of materials. Panel C represents different modulus of elasticity ranges for different classes of biological materials. [Permission requested from ref 81].

value that is almost 10-fold lower compared to the nanoindentation results on single insulin fibrils [57,89]. Gels formed with insulin fibrils show moduli ranging from 4 Pa to above 20 Pa depending on concentration and the aggregation kinetics [90]. Gels formed with TSS1 fibrils (three-stranded β-sheet) show storage moduli of 2 to 9 kPa depending on the pH in which the gels are formed [91]. The tunable mechanical properties of the (hydro)-gels mentioned above makes these structures even more interesting for usage in tissue regeneration. Studies with collagen films with different mechanical properties already show that muscle cells spread and proliferate more extensively on softer collagen fibrils compared to stiffer fibrils where the cells hardly show movement [92]. The mechanical properties of the underlying substrate influences not only movement and growth of cells, but is also reported to affect the differentiation of stem cells. Naive mesenchymal stem cells have been shown to differentiate towards neuronal cells when cultured on scaffolds mimicking the mechanical properties of brain tissue, whereas when cultured on stiffer collagenous bone-like scaffolds they become osteogenic [93]. A few studies report the use of amyloid used as scaffolds for tissue regeneration purposes [94,95]. A scaffold made of peptide nanofibers seemed to regenerate axons and knit brain tissue together, leading to functional return of vision in small mammals after

completely severing the optic tract [94].

CONCLUDING REMARKS

Measuring and understanding the mechanical characteristics of single amyloid fibrils could thus give insights into many different biological contexts. For the disease related amyloids, these mechanical properties may shed light on the pathology and mechanism of the disease. Functional amyloids often have remarkable mechanical properties, for instance natural adhesive amyloids, which could be exploited for newly developed biological adhesives. Furthermore, amyloids are already proven to be useful in constructing functionalized nanowires or in larger network-type materials. Tuning the mechanical properties of amyloid-based nanostructures thus offers the potential for further functional applications of amyloids as novel nanobiomaterials.

REFERENCES

1. Sipe JD, Cohen AS. (2000) J. Struct. Biol. 130:88-98
2. Dobson CM. (2003) Nature 426:884-890
3. Chiti F, Dobson CM. (2006) Annu. Rev. Biochem. 75:333-66
4. Fowler DM, Koulov AV, Balch WE, Kelly JW. (2007) TRENDS in Biochem. Sci. 32:217-24
5. Sagis LMC, Veerman C, van der Linden E. (2004) Langmuir 20:924-27
6. Kroes-Nijboer A, Venema P, van der Linden E. (2011) Food & Funct. DOI: 10.1039/C1FO10163C
7. Nelson R, Sawaya MR, Balbirnie M, Madsen AØ, Riekel C, Grothe R, Eisenberg D. (2005) Nature 435, 773-78
8. Ban T, Hamada D, Hasegawa K, Naiki H, Goto Y. (2003) J. Biol. Chem. 278: 16462-5
9. Sunde M, Serpell LC, Bartlam M, Fraser PE, Pepys MB, Blake CCF. (1997) J. Mol. Biol. 273, 729-39
10. Cherny I, Gazit E. (2008) Angew. Chem. Int. Ed. 47:4062-69
11. Petkova AT, Leapman RD, Guo Z, Yau W, Mattson MP, Tycko R. (2005) Science 307:262-265
12. Adamcik J, Mezzenga R. (2011) Soft Matter 7:5437-43
13. Villar M, Chou H, Luhrs T, Maji SK, Riek-Loher D, Verel R, Manning G, Stahlberg H, Riek R. (2007) Prot. Natl. Acad. Sci. 105:8637-8642
14. Heise H, Hoyer W, Becker S, Andronesi OC, riedel D, Baldus M. (2005) Prot. Natl. Acad. Sci. 102:15871-76
15. Gosal WS, Myers SL, Radford SE, Thomson NH. (2006) Prot. Pept. Lett. 13:261-70
16. Fändrich M, Meinhardt J, Grigorieff N. (2009) Prion 3:2 89-93
17. Kodali R, Wetzel R. (2007) J. Structt Biol. 17:48-57

18. Kumar S, Udgaonkar JB. (2010) Curr. Sci. 98:5 639-56
19. Kojima H, Ishijima A, Yanagida T. (1994) Proc. Natl. Acad. Sci. 91:12962-12966
20. Claessens MMAE, Bathe M, Frey E, Bausch AR. (2006) Nature Materials 5:748-753
21. Van Buren V, Cassimeris L, Odde DJ. (2005) Biophys. J. 89:2911-2926
22. Schaap IAT, Carrasco C, Pablo PJ de, Mackintosh FC, Schmidt CF. (2006) Biophys. J. 91:1521-1531
23. Fudge DS, Gardner KH, Forsyth VT, Riekel C, Gosline JM. (2003) Biophys. J. 85:2015-2027
24. Yang L, van der Werf KO, Koopman BFJM, Subramaniam V, Bennink ML, Dijkstra PJ, Feijen J. (2007) J. Bio. Mat. Res. 82:160-68
25. Heim AJ, Matthews WG. (2006) Appl. Phys. Lett. 89:181902
26. Maji SK, Perrin MH, Sawaya MR, Jessberger S, Vadodaria K, Rissman RA, Singru PS, Nilsson PR, Simon R, Schubert D, Eisenberg D, Rivier J, Sawchenko P, Vale W, Riek R. (2009) Science 325:328
27. Maji SK, Schubert D, Rivier C, Lee S, Rivier JE, Riek R. (2008) Plos Biol. 6:e17
28. Mostaert AS, Higgins MJ, Fukuma T, Rindi F, Jarvis SP. (2006) J. Biol. Phys. 32:393-401
29. Barnhart MM, Chapman MR. (2006) Annu. Rev. Microbiol. 60:131-47
30. Sullan RMA, Gunari N, Tanur AE, Chan Y, Dickinson GH, Orihuela B, Rittschof D, Walker GC. (2008) Biofouling 253:263-275
31. Scheibel T, Parthasarathy R, Sawicki G, Lin X, Jeager H, Lindquist SL. (2003) Proc. Natl. Acad. Sci. 100:4527-32
32. Carny O, Shalev D, Gazit E. (2006) Nanoletters 6:1594-97
33. Binnig G, Rohrer H. (2000) (reprinted from 1986) IBM J. Res. Develop. 44:279-93
34. Binnig G, Quate CF. (1986) Phys. Rev. Lett. 56:930-33
35. Hih JH, Engel A. (1993) Langmuir 9:3310-12
36. Hertz H. (1882) J. Reine Angewandte Math. 94:156–71.
37. Derjaguin BV, Muller VM, Toporov YUP. (1975) J. Coll. Interf. Sci. 53: 2
38. Johnson KL, Kendall K, Roberts AD. (1971) Proc. R. Soc. London A 324:301-313
39. Van der Werf KO, Putman CAJ, de Grooth BG, Greve J. (1994) Phys. Lett. 65:1195-97
40. Pittenger B, Erina N, Su C. (2010) Application Note Veeco Instruments Inc
41. Rosa-Zeiser A, Weilandt E, Hild S, Marti O. (1997) Meas. Sci. Technol. 8:1333-38
42. Sahin O. (2007) Rev. Sci. Instrum. 78:103707
43. Garcia VJ, Martinez L, Briceno-Valero JM, Schilling CH. (1997) Probe Microsc 1:107-116.
44. Burnham NA, Behrend OP, Oulevey F, Germaud G, Gallo PJ, Gourdon D, Dupas E, Kulik AJ, Pollok HM and Briggs GAD. (1997) Nanotechnology 8:67-75
45. Borgia A, Williams PM, Clarke J. (2008) Annu. Rev. Biochem. 77:101-25
46. Puchner EM, Gaub HE. (2009) Curr. Opin. Struc. Biol. 19:605-14
47. Fukuma T, Mostaert AS, Jarvis SP. (2006) Trib. Lett. 22:233-37
48. Kjelstrup-Hansen J, Hansen O, Rubhan HG, Bøggild P. (2006) small 2: 660-66

49. Koenders MMJF, Yang L, Wismans RG, Van der Werf KO, Reinhardt DP, Daamen W, Bennink ML, Dijkstra PJ, Van Kuppevelt TH, Feijen J. (2009) Biomaterials 30:2425-32
50. Howard J. (2001) Mechanics of motor proteins and the cytoskeleton. Sinauer Associates, Sunderland MA, USA
51. Knowles TP, Fitzpatrick AW, Meehan S, Mott HR, Vendruscolo M, Dobson CM, Welland ME (2007) Science 318:1900-3
52. Whang JC, Turner MS, Agarwal G, Kwong S, Josephs R, Ferrone FA, Briehl RW. (2002) J. Mol. Biol. 315:601-612
53. Smith JF, Knowles TPJ, Dobson CM, MacPhee CM, Welland ME. (2006) Prot Natl. Acad. Sci. 103:15806-15811
54. Ohler B. (2007) Rev Sci Instrum 78:063107
55. Cook SM, Schäffer TE, Chynoweth KM, Wigton M, Simmonds RW, Lang KM. (2006) Nanotechnology 2006, 17:2135-2145
56. Gibson CT, Smith DA, Roberts CJ. (2005) Nanotechnology 16:234-238.
57. Akhremitchev BB, Walker GC. (1999) Langmuir, 15:5630-5634
58. Guo S, Akhremitchev BB. (2006) Biomacromolecules 7:1630 1636
59. Mercato del LL, Maruccio G, Pompa PP, Bochicchio B, Tamburro AM, Cingolani R, Rinaldi R. (2008) Biomacromolecules 9:796-803
60. Khurana R, Ionescu-Zanetti C, Pope M, Li J, Nielson L, Ramirez-Alvarado M, Regan L, Fink AL, Carter SA. (2003) Biophys. J. 85:1135-1144
61. Adamcik J, Jung J, Flakowski J, De Los Rios P, Dietler G, Mezzenga R. (2010) Nature Nanotech. 5:423-428
62. Chapter 6;
63. Makin O, Serpell LC. (2005) FEBS Journal 272:5959-61
64. Karsai Á, Mártonfalvi ZS, Nagy A, Grama L, Penke B, Kellermayer MSZ. (2006) J. Struct. Biol. 155:316-26
65. Miklós SZ, Kellermayer MSZ, Grama L, Karsai Á, Nagy A, Kahn A, Datki ZL, Penke B. (2004) J. Biol. Chem. 290:8464-70
66. Bhak G, Lee S, Park JW, Cho S, Paik SR. (2010) Biomaterials 31:5986-95
67. Jordens S, Adamcik J, Amar-Yuli I, Mezzenga R. (2011) Biomacromolecules. 12:187-193
68. Dunstan DE, Hamilton-Brown P, Asimakis P, Ducker W, Bertolini J. (2009) Soft Matter 5:5020-28
69. Relini A, Torrassa S, Ferrando R, Rolandi R, Campioni S, Chiti F, Gliozzi A. (2010) Biophys. J. 98:1277-84
70. Minary-Jolandan M, Yu M. (2009) Biomacromolecules 10:2565-70
71. Segers-Nolten I, Van der Werf K, Van Raaij M, Subramaniam V. (2007) Proceedings of the IEEE Conf Eng Med Biol Soc 6609-6612
72. Zhou X, Cui CY, Zhang J, Liu J, Liu J. (2010) Chi. Sci. Bull. 55:1608-12
73. Adamcik J, Berquand A, Mezzenga R. (2011) Appl. Phys. Lett. 98:193701

74. Kol N, Adler-Abramovich L, Barlam D, Shneck RZ, Gazit E, Rousso I. (2005) Nanoletters 5:1343-46
75. Niu LJ, Chen XY, Allen S, Tendler SJB. (2007) Langmuir 23:7443-46
76. Flamia R, Zhdan PA, Castle JE, Tamburro AM. (2008) J. Mater. Sci. 43:395-97
77. Moreno-Herrero F, Perez M, Baro AM, Avila J. (2004) Biophys. J. 86: 517-525
78. Verhoff T, Glišović A, Schollmeyer H, Zippelius A, Salditt T. (2007) Biophys. J. 93:4425-32
79. Mücke N, Kreplak L, Kirmse R, Wedig T, Herrmann H, Aebi U, Langowski J. (2004) J. Mol. Biol. 335:1241-50
80. Chapter 4;
81. Knowles TPJ, Beuhler MJ. (2011) Nat. Nanotech. 6:469-79
82. Shorter J, Lindquist S. (2006) Mol. Cell 23:425-38
83. Paparcone R, Buehler MJ. (2011) Biomaterials 32:3367-74
84. Cohen SIA, Vendruscolo M, Dobson CM, Knowles TPJ. (2011) I. J. Mol. Sci. 12:5844-52
85. Cohen SIA, Vendruscolo M, Welland ME, Dobson CM, Terentjev EM, Knowles TPJ. (2011) J. Chem. Phys. 135:065105
86. Cohen SIA, Vendruscolo M, Dobson CM, Knowles TPJ. (2011) J. Chem. Phys. 135:065106
87. Cohen SIA, Vendruscolo M, Dobson CM, Knowles TPJ. (2011) J. Chem. Phys. 135:065107
88. Wang Y, Buell AK, Wang X, Welland ME, Dobson CM, Knowles TPJ, Perret S. (2011) J. Biol. Chem. 286:12101-107
89. Guo S, Akhremitchev BB. (2008) Langmuir 24:880-87
90. Manno M, Giacomazza D, Newman J, Martorana V, San Biagio PL. (2009) Langmuir Letter 26:1424-26
91. Rhugani RV, Salick DA, Lamm MS, Yucel T, Pochan DJ, Schneider JP. (2009) Biomacromolecules 10:1295-1304
92. McDaniel DP, Shaw GA, Elliott JT, Bhadriraju K, Meuse C, Chung K, Plant AL. (2007) Biophys. J. 92:1759-69
93. Engler AJ, Sen S, Sweeney HL, Discher DE. (2006) Cell 126:677-89
94. Ellis-Behnke RG, Liang Y, You S, Tay DKC, Zhang S, So K, Schneider GE. (2006) Prot. Natl. Acad. Sci. 28:5054-59
95. Holmes TC, De Lacalle S, Su X, Liu G, Rich A, Zhang S. (2000) Prot. Natl. Acad. Sci 97:6728-33

PART I

SURFACE INFLUENCES

CHAPTER 3

Atomic force microscopy study of substrate influences on morphologies of α-synuclein amyloid fibrils

Atomic force microscopy (AFM) is a powerful tool for obtaining nanoscale insights into structures and morphologies of biological samples. However, specific choices of experimental and scanning conditions can lead to differences in results. Here, we studied the morphological characteristics fibril height, periodicity and length of fibrils of the human α-synuclein protein on different underlying substrates. Hydrophobic highly ordered pyrolytic graphite (HOPG) substrates seem to break the fibrils during adsorption, while the commonly used hydrophilic mica showed long fibrils, with periodicities and heights comparable to other reports performed on mica substrates. However, on gold substrates a substantial fraction (25%) showed a deviating periodicity. The fibril affinity for these three substrates was higher than for glass and quartz, where fewer fibrils were present on the surface. In conclusion, our study shows distinct variations in fibril affinity and fibril morphological features on different substrates. We conclude that mica is an optimal surface for imaging amyloid fibrils with AFM, since it does not affect the morphology as some of the other surfaces do.

Sweers KKM, Bennink ML, Subramaniam V (2009) Proc. Ann. IEEE/EMBS Benelux Chapter p. 89-92

INTRODUCTION

The misfolding of proteins in fibrillar aggregates plays a key role in many neurodegenerative diseases [1]. Knowledge about the structure of these amyloid fibrils is an essential component of understanding the misfolding pathway. Atomic force microscopy (AFM) is a powerful technique to analyze the nanoscale morphology of these amyloid protein nanostructures and fibrils.

In order to get AFM images of amyloid fibrils representative of the fibril structure in solution, a proper choice of the underlying substrate is essential to avoid substrate-induced deformation of the fibrils. A frequently used substrate is freshly cleaved mica. Mica has a hexagonal crystallographic structure that is chemically relatively inert and atomically flat [2,3]. Upon cleaving it is very hydrophilic and negatively charged. The negative charge of mica is convenient for deposition of biological molecules on the surface. Most studies on morphological characteristics of amyloid fibrils formed by the protein α-synuclein are done on this surface [4-8]. α-synuclein is a small protein of 140 amino acids, and is involved in Parkinson's disease [1,9]. In AFM studies of α-synuclein fibril morphologies, the fibril height ranges from 7.5 nm [8] to 11 nm [4]. The periodicity of these fibrils depends strongly on specific protein mutant, ranging from above 100 nm for wild type α-synuclein to around 50 nm for E46K disease mutant α-synuclein [4,7,8]. Generally, the fibril diameters are well defined but there is much uncertainty about the way the protein monomers are organized within the fibril structure.

Here, we address the question whether the mica surface affects the morphology of the α-synuclein fibrils. To this end, we study the differences in morphology of α-synuclein fibrils on different underlying substrates, including mica, hydrophobic HOPG, glass, quartz, and gold. We conclude from our results that the deposition of α-synuclein amyloid fibrils on mica does not have a significant impact on the fibril structure.

MATERIAL & METHODS

EXPRESSION AND PURIFICATION OF SYNUCLEIN

We performed recombinant expression and purification of E46K disease mutant α-synuclein protein as previously described. [7]

AGGREGATION REACTION

A 100 μM monomeric E46K solution in 10 mM Tris-HCl, 50 mM NaCl, pH 7.4 was incubated at 70° C in Eppendorf tubes under constant shaking. After 27 hours,

the sample contained amyloid fibrils, which was verified by measuring the fluorescence intensity of the beta-sheet specific fluorescent dye ThioflavinT.

SUBSTRATES

Five different materials were used as substrates:

- Muscovite mica, V-1 Quality (Electron Microscopy Sciences, Hatfield PA, USA)
- Pyrolytic Graphite ZYH (Union Carbide Corporation, Cleveland OH, USA)
- Glass cover-slip (WillCo Wells BV, Amsterdam, The Netherlands)
- Quartz cover-slip (Electron Microscopy Sciences, Hatfield PA, USA)
- Gold, template stripped [10]

SAMPLE PREPARATION

AFM samples were prepared by placing on the substrate 50 µl of a fibril solution diluted 5x in 10 mM Tris-HCl, 50 mM NaCl, pH 7.4. The fibril solution was allowed to adsorb for at least 1 hour and then washed gently with 200µl buffer. For imaging, between 30 and 80 µl of fresh buffer solution was placed on the sample.

ATOMIC FORCE MICROSCOPY

We used a Bioscope II atomic force microscope (Veeco, Santa Barbara CA, USA) with a silicon probe (NSC36, tip C, 0.6 N/m, MikroMasch, Tallinn, Estonia) for imaging. Imaging was performed in a physiological buffer in tapping mode with low force settings (reduced to 3 nm, 80-90% of the free amplitude) to minimize interaction with the sample.

IMAGE MORPHOLOGY ANALYSIS

The surface root mean square (RMS) roughness was determined from nine scans of 400x400 nm for all surfaces using SPIP software (Image Metrology A/S, Lyngby, Denmark). The fibril affinity for the substrate was estimated from the AFM height images. The total number of fibrils was counted manually for each image and the number of fibrils per μm^2 was calculated for an area of at least 125 μm^2. Fibrils were analyzed for their heights and periodicities using SPIP software according to the procedure described in [7]. For both fibril affinity and fibril morphology, only fibrils longer than 100 nm were included in the analysis.

RESULTS

The RMS values (listed in Table 1) indicate that HOPG is the most flat. However, all surfaces have a maximum height difference smaller than the expected fibril diameter (around 8 nm). The glass surface reveals patches of around 1 nm in height.

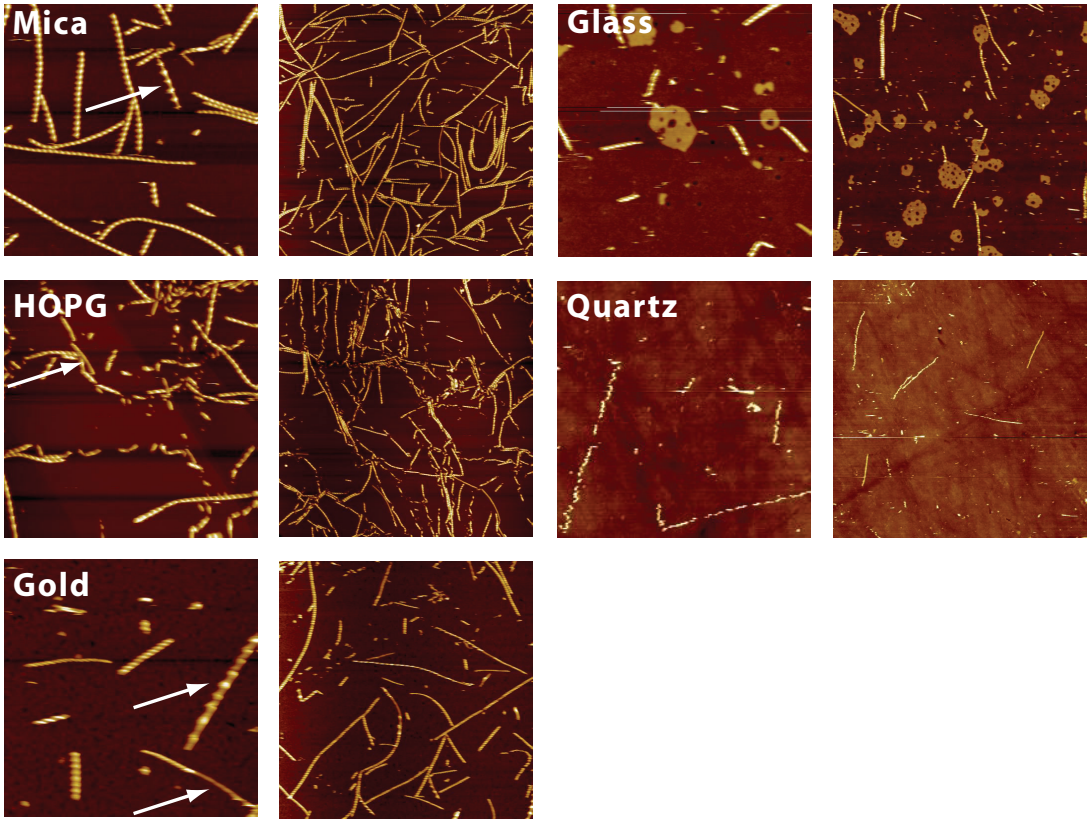

FIGURE 1; Typical images of fibrils on different substrates. The left panel presents 2x2 µm, the right panel 5x5 µm (512x512 pixels). The few fibrils with deviating periodicity or no periodicity at all on mica, HOPG and gold are indicated with arrows.

The number of fibrils per unit area found on the surfaces is inversely proportional to the surface roughness (Table 1). For every substrate, two typical images with fibrils are shown in Figure 1. The fibrils on HOPG often are segmented. Non-segmented fibrils seem to have a preference for the direction of the HOPG terraces. On the glass substrate, in addition to the fibrils, irregular patches of 5 nm in height are observed, similar to the smaller patches observed on the images made for the roughness analysis. However, fibrils are not found on top of the patches.

Fibrils are tightly bound to the surface; multiple scans over the same fibril did not

	Mica	*HOPG*	*Gold*	*Glass*	*Quartz*
RMS (nm)	0.0966	0.0546	0.1424	0.3568	0.3909
Fibrils (/μm²)	7.1	10.5	2.7	0.7	0.3
Nr of analyzed fibrils	147	116	116	82	-
Fibril height (nm)	7.9 ± 0.4	7.6 ± 0.6	7.7 ± 0.5	8.7 ± 0.9	-
Fibril periodicity (nm)	39.9 ± 2.3 (98%)	43.4 ± 4.2 (98%)	45.1 ± 3.1 (75%)	42.4 ± 3.7 (100%)	-
Fibril length (nm)	563 ± 366	251 ± 127	560 ± 363	513 ± 342	-

TABLE 1; The measured surface RMS values (measured before the deposition of fi-brils), number of fibrils per μm^2 and fibril morphological characteristics for the different surfaces. Although the number of fibrils on HOPG is high, the average fibril length is considerably smaller compared to the other surfaces. The differences between the fibril heights measured on mica compared to HOPG and gold are small but significant ($p<0.001$). For the fibril periodicity values the percentage of the total measured fibrils is given in parentheses.

move or break the fibrils. However, this was not the case for the quartz substrate on which fibrils remained loosely bound and were easily destroyed by the AFM tip during the first scan. Therefore, the fibrils on quartz were excluded from the morphology analysis.

Morphological characteristics of the fibrils were quantitatively analyzed for each substrate. The average fibril height for each substrate ranged between 7.6 and 7.9 nm with similar distributions, with the exception of the fibrils on glass, which were roughly 1 nm higher.

For mica, HOPG and glass, most fibrils show an average periodicity of around 42 nm, which is comparable to values that are reported in previous studies [4,8]. For gold the main population has a periodicity of 45 nm. However, a large fraction (25%) of fibrils displays a periodicity ranging from 70 to 140 nm, as shown in Figure 2.

DISCUSSION

Protein adsorption is driven by van der Waals forces, electrostatic double layer forces, and the hydrophobic effect [11,12]. Our data do not give insights into which of these interactions is more pronounced between the different substrates and the fibrils. However, a couple of observations can be made.

Firstly, considerably more fibrils per unit area are found on mica and HOPG

compared to the other three substrates. All fibrils were tightly bound to the surface except for quartz, where also very few fibrils were found.

Secondly, the average fibril lengths for mica, gold and glass are roughly comparable. However, the average fibril length for fibrils on HOPG is considerably smaller, and is ~250 nm compared to above 500 nm for the other substrates. The images indicate that the fibrils are broken during adsorption on the HOPG surface. Studies on monomeric protein adsorption indicate more conformational changes on adsorbing on hydrophobic surfaces than on hydrophilic surfaces [11,12]; our study suggests that this may also

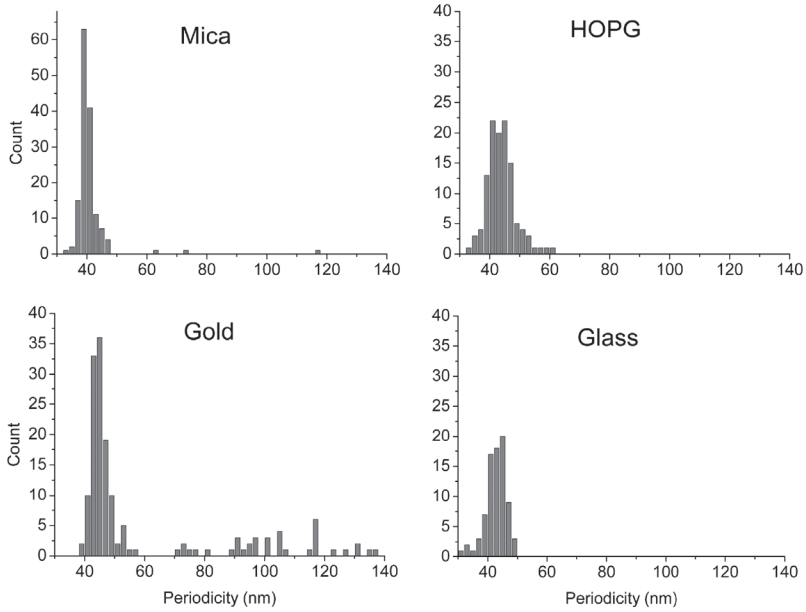

FIGURE 2; Periodicity distributions. All substrates show Gaussian distributions around 42 nm, with the exception of gold, which has additional components in the 70 to 140 nm range.

hold true for proteins in fibrillar form. The fragmentation of the fibrils could be induced by a hydrophobic interaction between the fibril and the surface.

Thirdly, the main fibril population found on the different surfaces has a periodicity of 42.7 nm. However, on gold a substantial number of fibrils (25%) had an average periodicity of 108 nm with a large distribution (STD = 28 nm). There are also fibrils present with alternate periodicities; see Figure 2. The different periodicities found on gold compared to the other substrates could be explained in two ways. The first explanation is that the periodicities found in amyloid fibrils are surface-induced. However, this scenario should give more different fibril populations on the different surfaces

when the differences between the crystallographic structures of the surfaces are taken into account. The other scenario is based on adding a selection criterion. It is a possibility that the aggregation product of proteins are, on a structural level, very diverse and that certain fibril populations only bind to surfaces that have a specific crystallographic structure. Although with different inter-atom distances, all substrates in this study have a hexagonal crystallographic structure. Gold is the only substrate with a face centered cubic crystallographic structure, which may explain our observation.

In contrast to differences found in periodicities, the fibril height is similar for all substrates. The fibril height is comparable to that reported in other studies [4,7,8]. However, the fibrils on glass are higher than on the other three substrates. This height difference could be caused by differences in interactions between substrate and tip [3].

When considering all parameters analyzed in this study, we can conclude that mica is a good choice for imaging amyloid fibrils. Both HOPG and mica show a high number of fibrils per unit area, but the fibrils on HOPG are fragmented. Although gold shows a substantial amount of fibrils with deviating periodicities, mica also shows a very small fraction of fibrils with deviating periodicities. The substrate characteristics of mica result in a high fibril adsorption without fragmenting the fibrils or altering their morphological characteristics compared to the other substrates.

CONCLUSION

Previous atomic force microscopy studies on amyloid fibril morphology, using mica as underlying substrate, have led to the proposing of fibril assembly models [5,6]. Although our results are still compatible with the morphological properties from these models, we wish to stress the importance of substrate choice in AFM imaging. The few fibrils with deviating periodicity found on mica can easily be discarded as outliers. However, the gold substrate revealed many more deviating fibrils.

When developing models of biological samples from AFM images, we recommend a greater awareness in substrate choice and suggest considering several different substrates. This study clearly shows that mica is a good choice for imaging amyloid fibrils, since it does not affect the structure of the fibrils.

ACKNOWLEDGEMENTS

The authors thank Kirsten van Leijenhorst-Groener for protein expression and purification, Ine Segers-Nolten for protein aggregation, and Kees van der Werf for expert advice on atomic force microscopy.

REFERENCES

1. Dobson CM. (2003) Nature 426:884-90
2. Adamcik J, Klinov DV, Witz G, Sekatskii SK, Dietler G. (2006) FEBS Letters 580: 5671-75
3. Noort van SJT, van der Werf KO, de Grooth BG, van Hulst NF, Greve J. (1997) Ultramicroscopy 69:117-27
4. Hoyer W, Antony T, Cherny D, Heim G, Jovin TM, Subramaniam V. (2002) J. Mol. Biol. 322:383-393
5. Jansen R, Dzwolak W, Winter R. (2005) Biophys. J. 88:1344-53
6. Khurana R, Ionescu-Zanetti C, Pope M, Li J, Nielson L, Ramirez-Alvarado M, Regan L, Fink AL, Carter SA. (2003) Biophys. J. 85:1135-44
7. Raaij ME van, Segers-Nolten IMJ, Subramaniam V. (2006) Biophys. J.: Biophys. Lett. L96-L98
8. Segers-Nolten I, van der Werf K, van Raaij M, Subramaniam V. (2007) Proc. 29th Ann. Inter. Conf. IEEE EMBS pp 6609-6612
9. Uversky VN, Fink AL. (2005) from: Mechanisms in Parkinson's Disease pp 1-30
10. Hegner M, Wagner P, Semenza G. (1993) Surf. Sci. 291:39-41
11. Müller DJ, Amrein M, Engel A. (1997) J. Struct. Biol. 119:172-88
12. Sherrat MJ, Holmes DF, Shuttleworth CA, Kielty CM. (2004) Biophys. J. 86: 3211-22

CHAPTER 4

Morphological and nanomechanical properties of α-synuclein fibrils on supported lipid bilayers investigated by atomic force microscopy

Atomic force microscopy (AFM) is an excellent tool to investigate morphological and mechanical characteristics of amyloid fibrils. An often-used method to determine mechanical characteristics of amyloid fibrils is to extract the bending rigidity of the fibrils, that is, to measure the average deviation of the fibril shape in AFM height images from a straight line connecting its ends and analyzing the results using statistical mechanical theories of semiflexible polymers. However, for this approach in particular, the choice of the underlying substrate is crucial to achieve meaningful values for the bending rigidity of the amyloid fibrils.

In this study we investigated the morphological and mechanical characteristics of α-synuclein fibrils. α-Synuclein is a small 140 amino acid protein that is involved in the neurodegenerative Parkinson's disease. We studied fibrils formed from the wild-type α-synuclein protein and from three different disease-related mutants on three different substrates: freshly cleaved mica, commonly used in AFM imaging, supported lipid bilayers of phosphatidylcholine, POPC, and supported lipid bilayers of a mixture of POPC and POPG (phosphatidylglycerol).

The ability of the fibrils to move around on the POPC membrane shows that the fibrils are in thermal equilibrium, thus allowing us to investigate bending rigidities of the α-synuclein fibrils without having to assume that the fibrils are in thermal equilibrium. We also demonstrated that α-synuclein fibrils indeed adsorb in thermal equilibrium on mica surfaces, considering that the bending rigidity values found on mica are similar to those on the POPC membrane where the fibrils were still able to freely move around. Furthermore, on the POPC-POPG mixture lipid bilayer we did not observe moving fibrils. This indicates that the fibrils are partly embedded into the lipid bilayer.

Sweers KKM, Stöckl M, Bennink ML, Subramaniam V. Manuscript in preperation

INTRODUCTION

α-Synuclein (αSYN) is a small protein implicated in the development of Parkinson's disease (PD) and is abundantly found in the human brain [1,2]. αSYN self assembles in amyloid fibrils where it adopts a cross-β structure, in which the β-strands are oriented perpendicular to the fibril axis [3-5]. These fibrils accumulate in cytosolic inclusions named Lewy bodies, which are the pathological hallmark of PD [6,7]. Another observation which leads to the hypothesis that the aggregation of αSYN is related to the development of PD are three disease-related point mutations in the protein, A30P [8], E46K [9], and A53T [10], all of which have a greater tendency to aggregate compared to the wild-type variant [11].

Atomic force microscopy (AFM) has proven to be ideally suited to investigate both morphological and mechanical characteristics of amyloid fibrils. Previous studies show the morphological differences and similarities between the different disease-related mutants [12,13]. Detailed AFM studies of fibril morphologies have resulted in general models of amyloid fibril structure and formation [14,15]. However, to get representative images of amyloid fibril structures with AFM, a proper choice of the underlying substrate is essential. A study of αSYN fibrils on different substrates, including commonly-used mica, highly ordered pyrolytic graphite, gold, and glass revealed different affinities of fibrils for the substrates, in which fibrils had a four-fold larger affinity for HOPG than for glass. However, the fibrils on HOPG appeared more fragmented compared to fibrils on the other surfaces. Morphological analysis of αSYN fibrils on the different substrates did not show significant differences [Chapter 3]. The influence of the underlying substrate on the mechanical characteristics of amyloid fibrils has not yet been thoroughly investigated. An often-used method to determine mechanical characteristics of amyloid fibrils is to interpret the average deviation of the fibril shape in AFM topography images from a straight line connecting its ends using statistical mechanical theories of semiflexible polymers [16,17]. This method has been used for several amyloid fibrils such as insulin fibrils [18], αSYN fibrils [Chapter 6], and HypF-N fibrils [19]. One major assumption with these studies is that the fibrils are in thermal equilibrium when adsorbing on the surface. The validity of this assumption could be verified by analyzing the data according to two different options for bending rigidity calculations, representing respectively a situation in which the fibrils are irreversibly trapped when deposited onto the surface and a situation in which the fibrils are thermally equilibrated on the surface before adhering more strongly. The calculation of the bending rigidity is in these cases performed on the complete dataset of all fibrils combined. When bending rigidities are calculated per fibril, to obtain for instance correlations between mechanical and morphological properties, the low number of datapoints can severely affect the accuracy in

the value of the bending rigidity, rendering this method less suitable.

In this study, we investigated the behavior of αSYN fibrils on a different kind of substrate compared to the previous study [Chapter 3], namely a supported lipid bilayer formed by phosphatidylcholine lipids (POPC). These membranes have been demonstrated to remain fluid when formed on a mica substrate because of the thin water layer trapped between the mica and the membrane [20].The fluidity of the membrane combined with the low affinity of αSYN for POPC membranes [21-23] is expected to allow fibril movement on the substrate. This substrate allowed to create a clear situation in which we know that the fibrils are thermally equilibrated on the surface before they adhered more strongly, without having to consider any trapping effects [24].

Aside from using this supported bilayer substrate to determine the correct bending rigidity of αSYN amyloid fibrils, the interaction between fibrils and lipid bilayers are furthermore interesting from a biological point of view. Recently, evidence was found that αSYN might be involved in regulating the size of synaptic vesicle pools [25-28]. Upon binding to phospholipid membranes, αSYN adopts a helical structure in the N-terminal region, which is in contrast to the cross-β structure it adopts in fibrils [29]. In both conformations the C-terminus of the protein is unstructured. All different disease-related mutants bind to phospholipid vesicles, however with a higher affinity to anionic lipids because of the positive net charge of the N-terminal region. A30P has a lower affinity for lipid vesicles compared to the other three αSYN mutants because of the mutation in the N-terminus, which causes local disorder in the α-helix [21,22,30-32]. Aside from monomer membrane interaction studies, the role of membranes in the aggregation reaction has been also investigated. These studies do not lead to a consensus. Some suggest that membranes promote αSYN aggregation [33-35] whereas others hypothesize that membranes could inhibit the reaction depending on the lipid protein ratio [35-37].

Here, we investigated the interaction between mature fibrils of wild-type, E46K, A53T and A30P αSYN and lipid membranes with atomic force microscopy. In comparison to the monomeric proteins, the fibrils do bind to the zwitterionic lipid (POPC) bilayer. The affinity for negatively-charged POPG membranes seemed even slightly higher. We found that the fibrils formed with the disease mutant A30P had less affinity for the lipid membranes. Because of the lower affinity of A30P fibrils, they were able to move on the membrane and formed larger clusters in the form of large film-like patches of fibrils on the membrane. We demonstrated that mature αSYN fibrils have affinity for phospholipid membranes. The absence of movement of the fibrils on the POPC-POPG lipid bilayer combined with the ~3 nm lower height measured on this bilayer suggests that the fibrils are incorporated in the membrane. However, the observation of the movement of the fibrils on the POPC membrane allowed us to unambiguously

determine the mechanical characteristics of the fibrils from AFM topography images. When comparing the bending rigidities of the fibrils obtained on the membranes with those on deposited on mica, we can conclude that there is no trapping effect for αSYN fibrils on mica, as we and others have hypothesized in earlier studies [Chapter 6, references 18,19,38].

MATERIAL & METHODS

ALPHA-SYNUCLEIN AND FIBRIL PREPARATION

Recombinant expression and purification of wild-type, E46K, A30P and A53T variant αSYN protein was performed as described previously [12]. To produce fibrils, 250 μM monomeric wild-type, E46K, A53T and A30P αSYN solution in 10 mM Tris-HCl, pH 7.4 were incubated at 70°C in tubes under constant shaking for 24 hours.

LIPID VESICLE PREPARATION

1-Palmitoyl-2-oleoyl phosphatidylcholine (POPC) and 1-Palmitoyl-2-oleoyl phosphatidylglycerol (POPG) stock solutions in chloroform (Avanti Polar Lipids Inc, Alabaster AL, USA) were mixed in the appropriate final molar concentration (1 mM). For the mixed membrane, a mixture of 65% POPC and 35% POPG was used. For vesicle preparation, a thin lipid film was formed by drying the phospholipid solution under a stream of nitrogen in a glass vial. The POPC films were rehydrated in 10 mM Tris-HCl buffer with 150 mM KCl, pH 7.4. The POPC-POPG mixture was rehydrated in 50 mM NaCl-only solution. Large unilamellar vesicles were prepared by extruding the solution 11 times through a 100 nm polycarbonate membrane filter (IsoporeTM Membrane Filters, Millipore, Billerica MA, USA).

SAMPLE PREPARATION

For AFM imaging of protein structures on mica the sample preparation was performed by placing 4 μl of a 20 times diluted protein solution on freshly cleaved mica and allowing it to adsorb for 2 minutes. The sample was washed gently with 200 μl MilliQ water and dried carefully under a gentle stream of nitrogen gas. For imaging in liquid the sample was washed with 200 μl of fresh buffer (10 mM Tris-HCl & 50 mM NaCl) and was not allowed to dry.

For the study of the protein structures on a phospholipid membrane, 200 μl of vesicle solution was placed on a sheet of freshly cleaved mica and left to adsorb for 30 minutes. In case of the POPC-POPG vesicles, the ion concentration was increased

from 50 mM to 1 M NaCl immediately after placement on the freshly cleaved mica. Subsequently the substrate was gently washed with fresh 50 mM NaCl buffer to remove the remaining vesicles in solution. The protein solution was added and left to adsorb for 30 minutes and washed with fresh buffer (10 mM Tris & 50 mM NaCl) and was not allowed to dry.

To check the uniformity of the bilayer, POPC was mixed with 1% rhodamine labeled DOPE. The vesicle solution was placed on freshly cleaved mica and left to adsorb for 30 minutes. Images were recorded using a 40x objective on a Nikon Eclipse TE-2000-U (Nikon Corporation, Tokyo, Japan). Rhodamine fluorescence was excited at 530±20 nm and recorded at 617±36.5 nm (dichroic mirror cut off at 562 nm).

ATOMIC FORCE MICROSCOPY

To check whether the aggregation resulted in mature fibrils, tapping-mode AFM imaging in ambient air conditions was performed on a home build system [39]. Tapping-mode AFM imaging in liquid environment was performed on Bioscope Catalyst (Bruker, Santa Barbara CA, USA). All measurements were made with a MSCT silicon nitride probe (MSCT, tip F, k=0.5 N/m, 10 nm nominal tip radius (Bruker, Santa Barbara CA, USA)). Imaging was performed in tapping mode with low force settings (80-90% of the free amplitude) to minimize interaction with the sample. The free amplitude in liquid was 2-3 nm compared to 100 nm in ambient air. The force settings during imaging on the fluid lipid membranes were even lower (95-98% of the free amplitude).

MORPHOLOGICAL ANALYSIS

For the morphological and bending rigidity analysis, the fibrils in the topography images were traced using a custom written script in Matlab using the DIPimage toolbox (version 2.3, TU Delft, Delft, The Netherlands). Morphological analysis was performed according to the procedure described in [12]. Only intact fibrils of at least 1 μm in length, not crossing other fibrils or particles that may influence the fibril shape, were included in the analysis. To be able to semi-quantitatively determine the affinity of the fibrils of the different variants to the POPC substrate, we recorded 40 images of 5x5 μm for each variant. On the POPC-POPG substrate we recorded 20 images. On these 40 (or 20) images those fibrils meeting the inclusion criteria were counted to determine the affinity of the 4 different αSYN variants for the POPC and POPC-POPG membranes.

BENDING RIGIDITY ANALYSIS

For the bending rigidity analysis we analyzed the traced fibril contours obtained with the custom written Matlab script. Only intact fibrils with the same specifications (at

least 1 μm and not crossing other fibrils or particles) as described in the morphological analysis were used in the bending rigidity analysis. Fibrils that appeared fragmented were also excluded from the analysis. The bending rigidity (κ) of the semiflexible αSYN fibrils was derived from the average magnitude of the thermally induced shape deviations from the straight line connecting the end points [16,17,38 and Chapter 6] according to the following equation:

$$\kappa = k_B T \times \frac{L^3}{48\langle v(x)^2 \rangle}$$

where kB is the Boltzmann constant, T the temperature in Kelvin, L the contour length of the fibril and v(x) is the distance from the midpoint the fibril segment to the secant line of the fibril segment. We calculated the bending rigidity for each individual fibril selected according to the criteria given above.

RESULTS

MONOMERS ON SUPPORTED BILAYERS

The binding of αSYN to lipid vesicles composed of different lipids and various sizes has been studied previously [21-23,32,40]. However, in these studies the lipids always exhibit a curvature due to the spherical shape of the vesicle which could influence the binding studies. To verify that the behavior of αSYN monomers is similar for supported lipid bilayers compared to the lipid vesicles we imaged the POPC and POPC-POPG membrane for at least an hour with monomeric αSYN in the surrounding medium. At t=0 a solution of monomeric αSYN is injected resulting in a final protein concentration of 30 μM. The results are displayed in Figure 1.

There is no significant monomer adsorption observed on the POPC layer, which is consistent with literature reports. αSYN in monomeric form does not have affinity for zwitterionic vesicles formed with POPC, but does exhibit affinity for negatively-charged POPC-POPG vesicles [21-23,32,40]. In contrast to POPC, protein monomers are seen adsorbing onto the POPC-POPG bilayer adsorption. This adsorption is a very rapid process, since protein nanostructures are already present on the membrane at time point zero. The surface roughness does not seem to change after 30 minutes, which suggests that no new monomers are adsorbing after 30 minutes.

ALPHA-SYNUCLEIN FIBRILS ON POPC SUPPORTED BILAYERS

Consecutively recording several AFM images of fibrils on the POPC substrate

demonstrates that the fibrils adsorb on the membrane and are able to move around (see Figure 2). This could be due to weak interaction of the fibrils with the POPC bilayer, but also because of the fluidity of the lipid layer itself. Fibrils appear to be fragmented, which is probably an artifact of the scanning. Due to the weak interaction, the AFM tip is able to push the fibrils back and forth as it is imaging the surface. This could appear in images as a fragmented fibril, whereas in a consecutive scan the fibril appears intact again. Some images also show horizontal stripes because of the fluidity of the membrane, this is also seen in Figure 1 with POPC only.

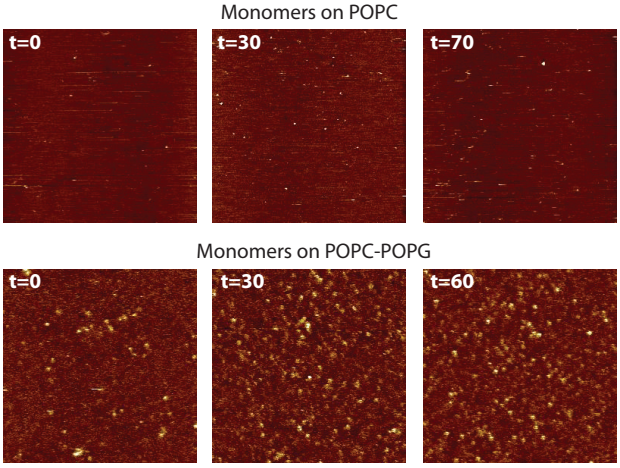

FIGURE 1; AFM height images of the a-SYN protein on POPC (top row) and POPC-POPG supported bilayers at different times after addition of the protein. Image size is 2x2 μm for all images and z-range is 2 nm for upper row and 5 nm for lower row.

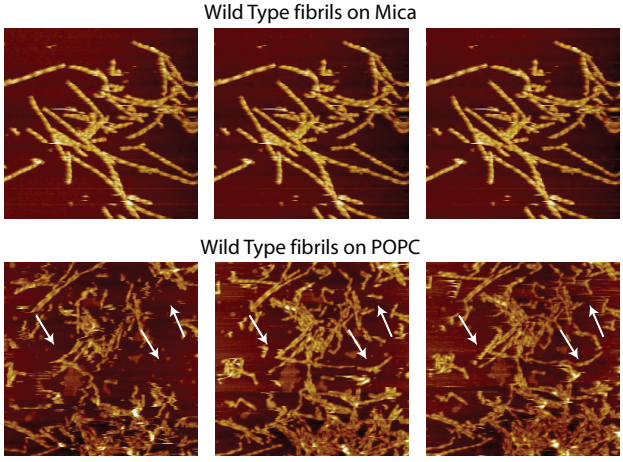

FIGURE 2; Consecutively recorded AFM height images of wildtype fibrils on mica (up-per row) and on the POPC supported bilayer (lower row). On the mica surface the fibrils appear intact and fixed onto the surface. On POPC the fibrils appear fragmented and loosely bound to the surface. They are able to move around, as indicated by the white arrows. AFM images were made in aqueous buffer, scan size 2x2 μm, z-range 17 nm.

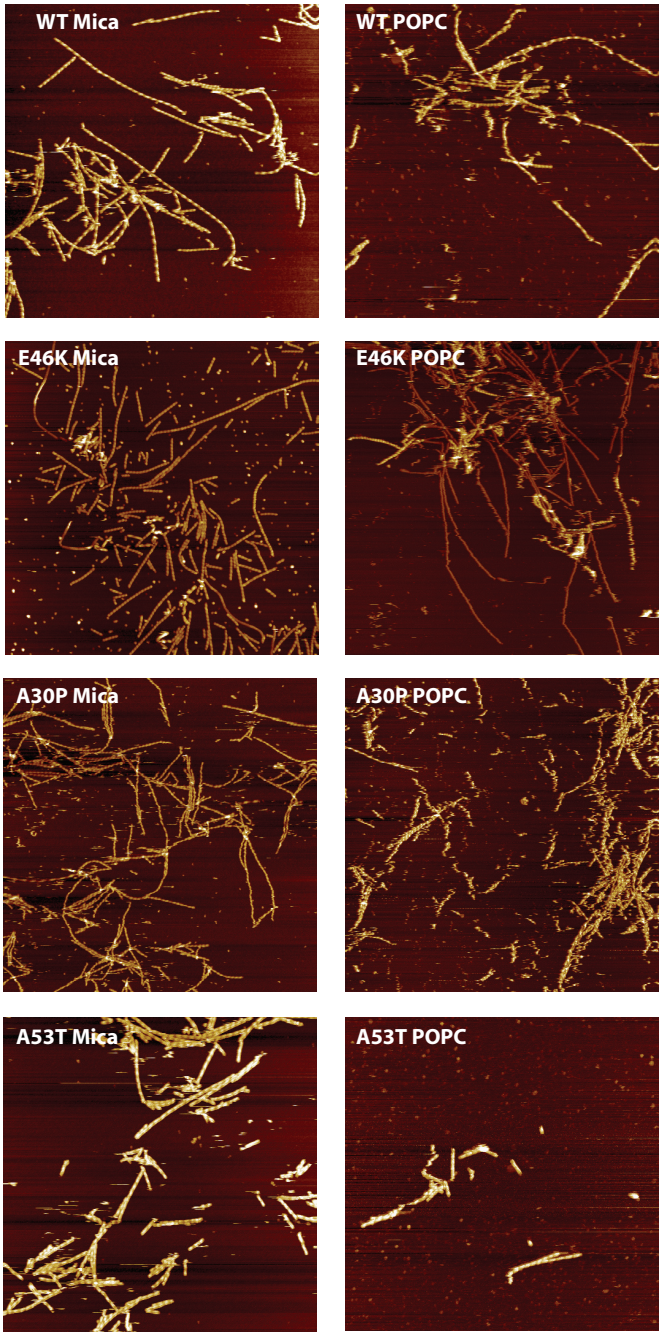

FIGURE 3; Typical AFM height images of fibrils made from wild-type and three different αSYN disease related variants fibrils on mica substrate (left column) and POPC bilayer (right column). AFM images were made in aqueous buffer, scan size 5x5 µm, z-range 20 nm.

For every αSYN variant, images were recorded in air (images not shown) and liquid on mica and in liquid on the POPC supported bilayer to systematically analyze fibril characteristics in different environments and on different surfaces. On the POPC bilayer 40 AFM images were recorded for every variant to get more insight into differences in affinity and binding of the 4 variants on POPC. Wild-type fibrils and the E46K mutant fibrils on the POPC layer showed no clear differences. The same number of fibrils (little over 70 fibrils, see also table 1) was found in 40 AFM images; these fibrils met the inclusion criteria of being longer than 1 μm and appeared not to be fragmented. However, the A30P mutant showed significantly less binding to the POPC substrate. Here in 40 images only 21 fibrils were found. Many of the A30P fibrils appear fragmented, which we attribute to the limited interaction with the POPC. A53T showed even less affinity for the POPC substrate. We needed a 10 times more concentrated protein solution to observe a similar number of fibrils (namely 70 fibrils, see table 1) on the POPC surface. Typical images are displayed in Figure 3.

Patch-like clusters of fibrils on the membrane were found for the wild-type protein and the 3 mutants (see Figure 4). The ability of the fibrils to move on the POPC surface most probably leads to clustering of the fibrils. The clusters had heights similar to those measured on individual fibrils, suggesting a monolayer of fibrils.

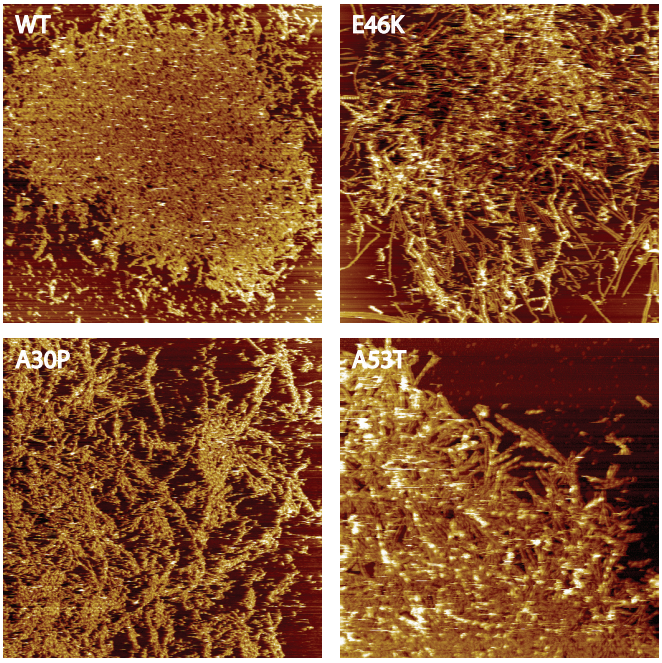

FIGURE 4; Clusters of αSYN fibrils found on the POPC bilayer, image size 5x5 μm, z-range 20 nm.

MORPHOLOGICAL ANALYSIS

The height and periodicity of the fibrils were analyzed (see Table 1). Fibril heights were consistently higher when measured in liquid on mica as compared to the heights measured in ambient conditions. The heights of the fibrils on the supported membrane were consistently lower when compared to the height obtained on mica for all fibril variants. This could suggest that the fibrils are somewhat incorporated in the membrane. Periodicities of the fibrils of all variants ranged from 65 to 140 nm. The periodicities of each variant fibril species did not change when measured on the different surfaces or under different environmental conditions.

	Mica Air	*Mica Liquid*	*POPC Liquid*
Wild-type	9.0 ± 1.2 nm (N=42)	9.3 ± 1.1 nm (N=70)	8.4 ± 0.8 nm (N=76)
E46K	8.0 ± 0.8 nm (N=30)	8.4 ± 0.9 nm (N=51)	6.2 ± 1.2 nm (N=77)
A30P	7.9 ± 0.7 nm (N=62)	9.0 ± 0.4 nm (N=48)	6.7 ± 0.9 nm (N=21)
A53T	8.8 ± 0.9 nm (N=60)	9.1 ± 1.0 nm (N=49)	8.7 ± 0.7 nm (N=70)

TABLE 1; Fibril heights of 4 different variants (wild-type, E46K, A30P and A53T) measured on a mica substrate in air and liquid. The decrease in fibril height from liquid to air was between 10% and 20%. Last column shows the fibril heights on POPC membrane in liquid conditions.

BENDING RIGIDITY ANALYSIS

For each of the four protein variants, the bending rigidity was systematically analyzed on the different substrates and environmental conditions (see Table 2). The bending rigidities were similar for all surfaces, environmental conditions and fibril variants. In liquid, a trend is visible for all mutants where the bending rigidity is slightly lower when measured on the POPC membrane compared to the mica surface. However, these differences are not statistically significant ($p<0.2$ by Wilcoxon signed-rank test).

	Mica Air	*Mica Liquid*	*POPC Liquid*
Wild-type	1.44	1.06	0.46
E46K	0.71	1.04	0.58
A30P	0.88	0.71	0.36
A53T	1.26	3.07	0.96

TABLE 2; Bending rigidities for each αSYN variant measured on the different substrates, mica and POPC, and under different environmental conditions. All numbers are in 10^{-24} Nm^2.

WILD-TYPE FIBRILS ON POPC-POPG SUPPORTED BILAYER

Thus far we used POPC supported lipid bilayers as a substrate to analyze morphological and especially mechanical properties of αSYN fibrils. However, POPC is zwitterionic and neutrally charged at the conditions used in this study. In a cellular environment membranes are often mixtures of several lipids. We therefore used a mixture of POPC-POPG to investigate the αSYN fibrils on a partly negatively charged lipid bilayer.

Wild-type αSYN fibrils showed similar affinity for the POPC-POPG bilayer as compared to the POPC-only bilayer. An analysis of 20 images on POPC-POPG yielded 31 fibrils, compared to 76 fibrils in 40 images on the POPC-only membrane. However, no fibril movement was observed on the surface, which could indicate a different binding mechanism. The fibrils on POPC-POPG bilayer are also considerably lower in height (~3 nm, see Table 3) compared to the fibril height on the mica and POPC-only surfaces. A typical image of wild-type fibrils on the mixed membrane is shown in Figure 5 and height data of wild-type fibrils on different surfaces is displayed in Table 3. The fibril height of 3 to 4 nm could imply that the fibrils are incorporated in the membrane.

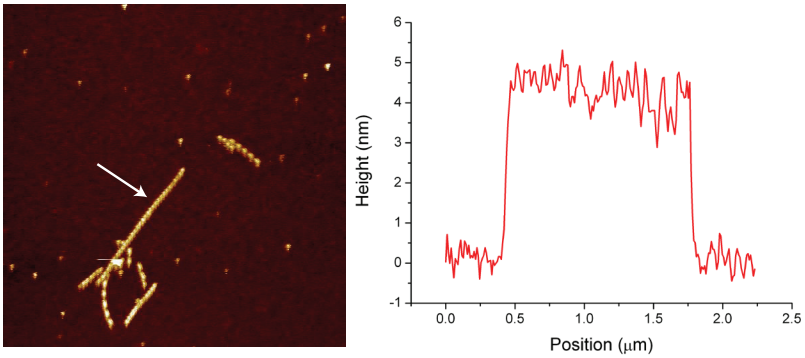

FIGURE 5; Typical AFM image of wild-type fibrils on a POPC-POPG supported bilayer with corresponding height profile of fibril indicated with arrow. Image size is 5x5 μm and z-range is 10 nm.

Surface	*Wild-type α-synuclein fibril height*
Mica (Liquid)	9.3 ± 1.1 nm (N=70)
POPC (Liquid)	8.4 ± 0.8 nm (N=76)
POPC-POPG (Liquid)	5.1 ± 1.5 nm (N=31)

TABLE 3; Wild-type αSYN fibril heights on the different surfaces; mica, POPC and POPC/POPG measured in liquid.

DISCUSSION

The POPC supported bilayer on mica was uniform and remained fluidic, verified by scratching the bilayer with the AFM tip and imaging the self repairing capabilities. The uniformity of the layer on mica was verified with fluorescence microscopy, see Figure 6.

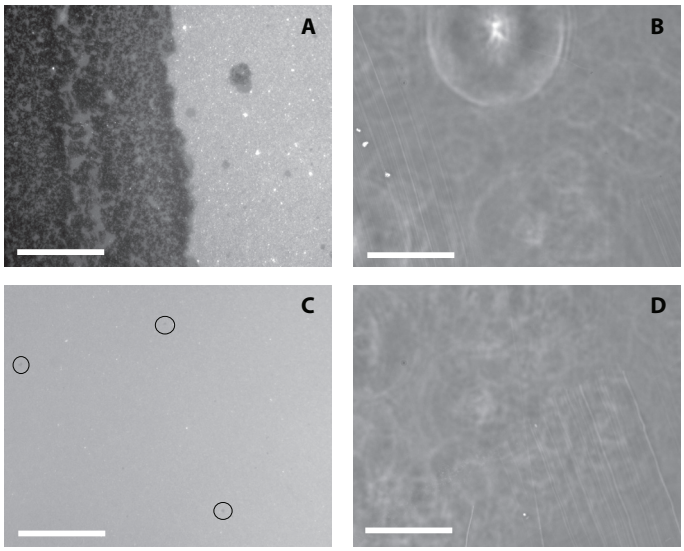

FIGURE 6; Fluorescence and corresponding light microscopy images of the POPC biayer on mica. The layer holds 1% fraction DOPE labeled with rhodamine. (A) Fluorescence microscopy image clearly shows the transition from mica (left) to the lipid bilayer (right), where in the corresponding white light image (B) no transition is to be seen. (C) shows a uniform fluorescent POPC bilayer (with corresponding white light image (D)) with three small defects (black circles). Scale bars are 100 μm.

AFM imaging at higher lateral resolution revealed small lipid patches on top of the bilayer (few 100 of nanometers in size), but otherwise the layer was uniform. These extra lipid patches were always around 4 nm in height (see Figure 7). The POPC-POPG membrane had multiple layers. From the height differences the thickness of these layers was determined to be ~4 nm corresponding to bilayers and not lipid monolayers, see Figure 7. Due to the fluidity and self-repairing capabilities of the membrane it was not possible to measure the height of the uniform layer by AFM. To verify whether the results measured on the supported lipid bilayers are comparable to other studies with vesicles we started this study by investigating the affinity of αSYN in monomeric form to the membranes. The behavior of αSYN in monomeric form on the supported bilayers was similar to that found before with vesicles, where αSYN does not show affinity for the POPC and does show affinity for the POPG-POPC mixed bilayer [21-23,32,40]. However, in the studies using bilayer vesicles the lipids always exhibit a curvature due to

the 3D shape of the vesicle which could influence the binding. So although, the affinity was found to be qualitatively similar, the interaction could still be very different due to the different packing of lipids.

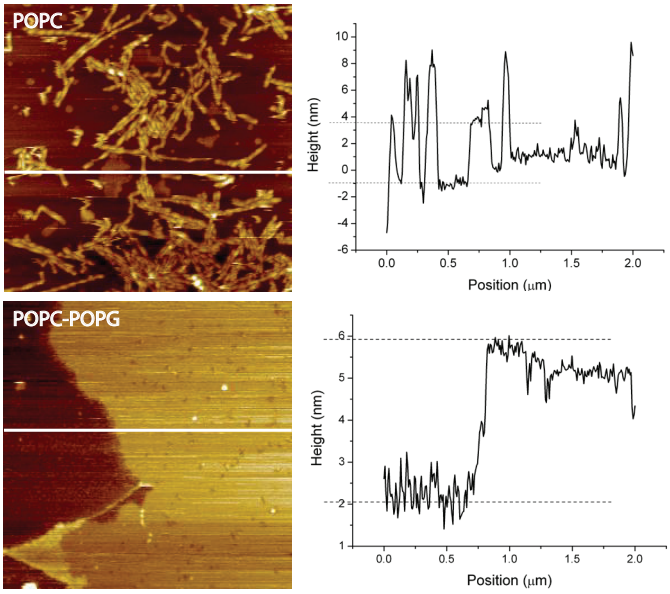

FIGURE 7; Patch height of both supported bilayers. The POPC bilayer was mostly uni-form however a few small patches (4-5 nm in height) were occasionally found. The POPC-POPG bilayer was less uniform and large multilayered parts were found, however always consisting of bilayers.

All four αSYN variant fibrils have affinity for the POPC membrane, however for A53T we needed significantly more fibrils to get the same surface coverage (2 times diluted compared to 10 or 20 times for the other variants). The binding to the membrane was for all four variants loose, seen by the apparently fragmented fibrils measured on POPC. Just as in monomeric form, A30P fibrils had a lower affinity for POPC when compared with the other three variants. This resulted in a lower number of fibrils on POPC bilayers for the analysis. This observation could indicate that also in fibrillar form the N-terminus plays a role upon lipid binding. The affinity of the wild-type fibrils for POPC-POPG appeared similar to the POPC membrane (31 fibrils on 20 images compared to 76 fibrils on 40 images). However, all fibrils were firmly bound, that is no fragmented fibrils were observed and all fibrils were considerably lower in height.

Morphological analysis of the fibrils showed no great significant differences compared to previous studies. Periodicities are slightly different compared to other studies, especially the E46K variant showed a larger periodicity (~70 nm) compared to the

often measured 45 nm. However the aggregation conditions (70° Celsius and no extra ions) are also different from other studies [12,13], which might explain this difference. Recently Adamcik et al. showed periodicity differences for amyloid fibrils when aggregated or adsorbed on the surface with different ion concentrations [41]. The heights are comparable to previous studies and also the height differences measured in liquid versus air (20%) have been observed previously [12,13 and Chapter 5 & 6]. There is a slight height difference between fibrils measured in liquid on mica compared to those on POPC bilayers. However, this height difference is below 1 nm, a difference that could also be attributed to AFM settings, like for instance the force setpoint, or environmental conditions [42 and Chapter 5]. On the POPC-POPG bilayer the fibrils were significantly lower in height (more than 3 nm) when compared to the fibrils on the mica substrate. Compared to the fibrils on POPC there was almost no movement of the fibrils on the POPC-POPG membrane. Combined with the height reduction of the fibrils this could mean that the fibrils are incorporated in the membrane. Previously, fibrils were found to be disruptive to POPG-only vesicles. Incorporation of fibrils in the membrane could be a reason for this vesicle disruption. Due to the strong interaction between the fibril and the lipids constituting the membrane, one can imagine that this induces a reorganization of the lipids in the bilayer leading to membrane thinning and even disruption [43]. Additionally, the absent movement of fibrils indicates that the lipids interacting with the fibrils do not diffuse freely anymore. Presumably the local enrichment of POPG and its interaction with fibrils leads to the formation of solid lipid domains, what also may be impair the membrane integrity.

The fluidity of the POPC membrane either alone or combined with the low adsorption of the fibril to the membrane most probably allows the fibrils to move around. The movement of the fibrils on the membrane created a monolayer of fibrils. This observation could suggest that fibrils do cluster into higher ordered assemblies in close proximity of membranes. Clustering and alignment of protein fibrils on different kind of surfaces has been seen previously [44]. More importantly, the ability to move around made it possible to unequivocally determine the bending rigidity of the amyloid fibrils. Direct comparison with data obtained from fibrils on mica showed that the assumption that the fibrils were in thermal equilibrium during the deposition was correct. Bending rigidity data shown in Table 2 are comparable to values measured previously for amyloid fibrils [38 and Chapter 6]. All bending rigidities found in different scanning environments or on the two different substrates are in the same range. The movement on the POPC bilayer confirmed that the fibrils are able to move and equilibrate freely on the surface. However, it also confirms that the fibrils are also adsorbed in a state close to thermal equilibrium when they adsorb on a mica surface.

CONCLUSIONS

In this study we report a systematic morphological and mechanical analysis of 4 different αSYN variants (wild-type, E46K, A53T and A30P) on supported lipid bilayers. Although the monomeric form of the protein does not bind to the POPC membrane, the fibrils do show affinity but do not seem to be incorporated within the membrane. On POPG-POPC mixed membranes the fibrils do seem to be incorporated, as can be inferred from their reduced height and lack of movement on this mixed lipid bilayer. These findings suggest that the fibrils partially embed into the lipid bilayer, thereby locally reorganizing the lipids, which could impair membrane integrity.

The ability of the fibrils to move around on the POPC membrane gave the opportunity to investigate unequivocally the bending rigidities of the αSYN fibrils without relying on any assumption on whether the fibrils are adsorbed in a thermal equilibrium state. This also made it possible to compare the bending rigidity values measured on mica to see whether the equilibrium assumption holds for mica surfaces. When comparing the bending rigidities of the fibrils obtained on the membranes with those on deposited on mica, we can conclude that there is no trapping effect for αSYN fibrils on mica.

REFERENCES

1. Goedert M. (2001) Nat. Rev. Neurosci. 2:492-501
2. Uversky VN, Fink AL. (2005) from: Mechanisms in Parkinson's Disease pp 1-30
3. Serpell LC, Berriman J, Jakes R, Goedert M, Crowther RA. (2000) Proc. Natl. Acad. Sci. 97:4897-4907
4. Vilar M, Chou H, Luhrs T, Maji SK, Riek-Loher D, Verel R, Manning G, Stahlberg H, Riek R. (2008) Proc. Natl. Acad. Sci. 105:8637-8642
5. Li L, Darden TA, Bartolotti L, Kominos D, Pedersen LG. (1999) Biophys. J. 76:2871-2878
6. Schultz W. (2006) Proc. Natl. Acad. Sci. 103:1661-1668
7. Spillantini MG, Schmidt ML, Lee VM, Trojanowski JQ, Jakes R, Goedert M. (1997) Nature 388:839-40
8. Kruger R, Kuhn W, Muller T, Woitalla D, Graeber M, Kosel S, Przuntek H, Epplen JT, Schols L, Riess O. (1998) Nat. Genet. 18:106-8
9. Zarranz JJ, Alegre J, Gomez-Esteban JC, Lezcano E, Ros R, Ampuero I, Vidal L, Hoenicka J, Rodriguez O, Atares B, Llorens V, Gomez Tortosa E, Del Ser T, Munoz DG, De Yebenes JG. (2004) Ann. Neurol. 55:164-73
10. Polymeropoulos MH, Lavedan C, Leroy E, Ide SE, Dehejia A, Dutra A, Pike B, Root H, Rubenstein J, Boyer R, Stenroos ES, Chandrasekharappa S, Athanassiadou A,

Papapetropoulos T, Johnson WG, Lazzarini AM, Duvoisin RC, Di Iorio G, Golbe LI, Nussbaum RL. (1997) Science 276:2045-47

11. Li J, Uversky VN, Fink AL. (2001)Biochemistry 40:11604-13
12. Raaij ME van, Segers-Nolten IMJ, Subramaniam V. (2006) Biophys. J.: Biophys. Lett. L96-L98
13. Segers-Nolten I, van der Werf K, van Raaij M, Subramaniam V. (2007) Proc. 29th Ann. Inter. Conf. IEEE EMBS pp 6609-6612
14. Khurana R, Ionescu-Zanetti C, Pope M, Li J, Nielson L, Ramirez-Alvarado M, Regan L, Fink AL, Carter SA. (2003) Biophys. J. 85:1135-1144
15. Jansen R, Dzwolak W, Winter R. (2005) Biophys. J. 88:1344-1353
16. Mücke N, Kreplak L, Kirmse R, Herrmann H, Aebi U, Langowski J. (2004) J. mol. Biol. 335:1241-1250
17. Whang JC, Turner MS, Agarwal G, Kwong S, Josephs R, Ferrone FA, Briehl RW. (2002) J. Mol. Biol. 315:601-6122
18. Smith JF, Knowles TPJ, Dobson CM, MacPhee CM, Welland ME. (2006) Proc. Natl. Acad. Sci 103:15806-15811
19. Relini A, Torrassa S, Ferrando R, Rolandi R, Campioni S, Chiti F, Gliozzi A. (2010) Biophys. J. 98:1277-84
20. Seu KJ, Pandey AP, Haque F, Proctor EA, Ribbe AE. et al. (2007) Biophys. J. 92:2445-50
21. Shvadchak VV, Falomir-Lockhart LJ, Yuschenko DA, Jovin TM. Wiley-VCH 2011
22. Pandey AP, Haque F, Rochet JC, Hovis JS. (2009) Biophys. J. 96:540-51
23. Rooijen van B, Cleassens MAE, Subramaniam V. (2009) Biochem. Biophys. Acta. 1788:1271-78
24. Rivetti C, Guthold M, Bustamante C. (1996) J. Mol. Biol. 264:919-932
25. Cabin DE, Shimazu K, Murphy D, Cole NB, Gottschalk W, Mcllwain KL, Orrison B, Chen A, Ellis CE, Paylor R, Lu B, Nussbaum RL. (2002) J. Neurosc. 22:8797-07
26. Giehm L, Oliveira CLP, Christiansen G, Pedersen JS, Otzen DE. (2010) J. Mol. Biol. 401:115-133
27. Murphy DD, Rueter SM, Trojanowski JQ, Lee VM. (2000) J. Neurosci. 20:3214-20
28. Chandra S, Gallardo G, Fernández-Chacón R, Schlüter OM. (2005) Cell 123:383-96
29. Jao CC, Hegde BG, Chen J, Haworth IS, Langen R. (2008) Prot. Nat. Acad. Sci. 105:19666-71
30. Jo, E.; Fuller, N.; Rand, R.P.; St George-Hyslop, P.; Fraser, P.E. Defective Membrane Interactions of Familial Parkinson's Disease Mutant A30P α-Synuclein. J. Mol. Biol. 2002, 315, 799-807
31. Georgieva ER, Ramlall TF, Borbat PP, Freed JH, Eliezer D. (2010) J. Biol. Chem. 285:28261-74
32. Stöckl M, Fischer P, Wanker E, Herrmann A. (2008) J. Mol. Biol. 375:1394-1404.
33. Lee HJ, Choi C, Lee SJ. (2002) J. Biol. Chem. 277:671–678.

34. Necula M, Chirita CN, Kuret J. (2003) J. Biol. Chem. 278:46674–80.
35. Beyer K. (200&) Biophys. J. 47:285–299.
36. Narayanan V, Scarlata S. (2001) Biochemistry 40:9927–34.
37. Zhu M, Fink AL. (2003) J. Biol. Chem. 278:16873–77.
38. Knowles TP, Fitzpatrick AW, Meehan S, Mott HR, Vendruscolo M, Dobson CM, Welland ME. (2007) Science 318:1900-1903
39. Van der Werf K, Putman C, de Grooth B, Segerink F, Schipper E, van Hulst N, Greve J. (1993) Rev. Sci. Instr. 64:2892-7
40. Rhoades E, Ramlall TF, Webb WW, Eliezer D. (2006) Biophys. J. 90:4692-4700
41. Adamcik J, Mezzenga R. (2011) Soft Matter 7:5437-43
42. Van Noort SJT, van der Werf KO, de Grooth BG, van Hulst NF, Greve J. (1997) Ultramicroscopy 69:117-127
43. Kayed R, Sokolov Y, Edmonds B, McIntire TM, Milton SC, Hall JE, Glabe CG. (2004) J. Biol. Chem. 279:46363–66
44. Paez, A.; Tarazona, P.; Mateos-Gil, P.; Vélez, M. (2009) Soft Matter 5:2625-37

PART II

FIBRIL STRUCTURE

CHAPTER 5

Atomic force microscopy under controlled conditions reveals structure of C-terminal region of α-synuclein in amyloid fibrils

Atomic force microscopy (AFM) is widely used to measure morphological and mechanical properties of biological materials at the nanoscale. AFM is able to visualize and measure these properties in different environmental conditions. However, these conditions can influence the results considerably, rendering their interpretation a matter of some subtlety. We demonstrate this by imaging ~10 nm diameter α-synuclein amyloid fibrils, focusing specifically on the structure of the C-terminal part of the protein monomers incorporated into fibrils. Despite these influences leading to variations in fibril heights, we have shown that by maintaining exquisite control of AFM settings we can quantitatively compare the morphological parameters of fibrils imaged in air or in buffer conditions. From this comparison we were able to deduce the semi-flexible character of this C-terminal region.

Fibril height differences measured in air and liquid indicate that the C-terminal region collapses onto the fibril core upon drying. The fibril height decreases upon increasing ion concentration, suggesting that the C-terminal tails collapse into more compact structures as a result of charge screening. Finally, Peakforce QNM measurements show an apparent heterogeneity of C terminal packing along the fibril length.

Sweers KKM, van der Werf KO, Bennink ML, Subramaniam V, submitted to ACS Nano

INTRODUCTION

Atomic force microscopy (AFM) is a powerful tool to investigate morphological and mechanical properties of nanoscale biological materials in their near-native environment. AFM-based approaches have yielded structural and functional insights into the aggregation of proteins into amyloid fibrils, reviewed, for example, in Gosal et al. & Knowles et al. [1,2]. Amyloid fibrils of several proteins are related to the development of neurodegenerative diseases. One example of such a disease-related protein is the human α-synuclein (αSYN) protein, which forms amyloid fibrils that are implicated in Parkinson's disease [3,4]. Several AFM-based morphological studies on αSYN fibrils have been reported in the literature, comparing fibrils formed from different mutants of αSYN. Different structural models have been derived from these data [4-7]. The height of fibrils formed from wild type αSYN found in several previously reported studies ranges from 5 to 15 nm, which can be attributed to the significant morphological diversity of the fibrils formed (polymorphism), but also to variations in the AFM scanning conditions, see Figure 1.

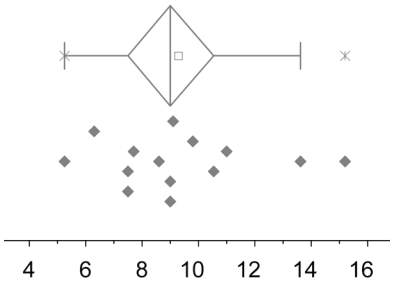

FIGURE 1; Box-and-whisker diagram indicating the spread of fibril height data found in literature measured with AFM or transmission electron microscopy for wild type α-synuclein [5-21]. Plot indicates sample minimum, maximum and median (vertical lines), outliers (starts) and the average of all data points (open square).

One aspect influencing the morphology of protein aggregates and other biological samples measured with AFM that is often neglected is the role of the underlying substrate and the surrounding medium. Substrate influences have been studied previously where for instance tuning the hydrophobicity of the surface alters the propensity for IAPP monomers to aggregate in amyloid fibrils [22]. In contrast to other nanometer-scale imaging techniques (such as electron microscopy), an innate advantage of AFM is its ability to image biological samples in physiologically relevant solutions. The AFM mode commonly used with biological samples is tapping or intermittent mode, which can be used both in ambient air and liquid conditions. However, tip-sample interactions

are very different for both media resulting in large morphological differences of nanometer scale features. As a result of this difference in interaction forces, different driving amplitudes and force setpoints have to be used to optimally image the fibrils. This leads to differences in morphological parameters, such as the fibril height. Furthermore the cantilever behavior is very different for both media. The hydrodynamic damping and the extra apparent mass attributed to the displaced liquid cause the resonant frequency to reduce three fold and lowers the Q-factor significantly [23]. In addition, when the cantilever is actively driven in a liquid cell, the liquid droplet and cell chamber could add more resonances, which requires some trial and error to find the correct resonant frequency for operation. These differences in operating frequencies can also induce differences in fibril morphology. For instance, the apparent amyloid fibril diameter has been reported to decrease in one study [24] and increase in another [25] when imaged in ambient air compared to liquid conditions. Also with piezoresponse force microscopy the apparent amyloid fibril height and width decreases significantly when imaged in air compared to liquid [26].

In this study we have imaged αSYN protein fibrils using tapping mode AFM imaging in different environmental conditions. We showed that with careful control of the operating parameters the fibril morphology measured in different environmental conditions could shed light on the structure of the C-terminal region in αSYN amyloid fibrils. Human αSYN is a small 140 amino acid protein associated with Parkinson's disease [2,3,27]. αSYN forms fibrils of around 10 nm in diameter and displays a periodic height variation along its length, attributed to a twisted structure. The C-terminal region is believed to be unstructured in both monomeric and fibrillar form and is highly negatively charged. The C-terminus consists of ~40 amino acids which, when fully extended, correspond to a length of ~15 nm. In this study we have studied the effect of the surrounding medium on the structure of the C-terminal part of the protein when aggregated into amyloid fibrils. To this end we used full-length wild type protein and the disease-related mutant E46K bearing a point mutation located in the fibril core [28]. The E46K mutant is expected to have a similarly unstructured C-terminus as the wild type protein. We furthermore investigated the fibrils generated from a C-terminally truncated variant, αSYN(1-108), comprising of amino acids 1-108.

We hypothesize that the C-terminus is unstructured and is exposed on the surface of the fibril, like a polymer brush (Figure 2A). The structure of the C-terminus within this polymer brush can be influenced by different environmental conditions (Figure 2B). Firstly, the C-terminal tail could collapse upon drying of the fibril. To measure this collapsing effect upon drying we measured the difference in fibril height of full-length and C-terminus truncated α-synuclein fibrils under different solution conditions. The

height reduction due to the C-terminal region collapsing on the fibril core is, as expected, more apparent in full-length variants, the wild type and E46K fibrils, than in the C-terminus truncated variants. Secondly, the C-terminal brush on the fibril exterior is likely to differ in size as a function of the extent of charge shielding by ions in the solution. This could create fibril height differences at different ion concentrations measured with AFM. Finally, we test whether the polymer brush is uniformly structured along the fibril length. We expect that different tip-sample interactions can partly be visualized by making force distance curves on the fibrils. In this study we used Peakforce QNM to rapidly acquire force distance curves and map different surface properties like modulus of elasticity according to the DMT model and adhesion [29,30]. This newly-introduced technique has already been used to characterize mechanical properties of polymers, nanosheets and amyloid fibrils [21,31-33]. Here, we use the method to map differences in interaction forces between the substrate and fibril, and along the fibril axis.

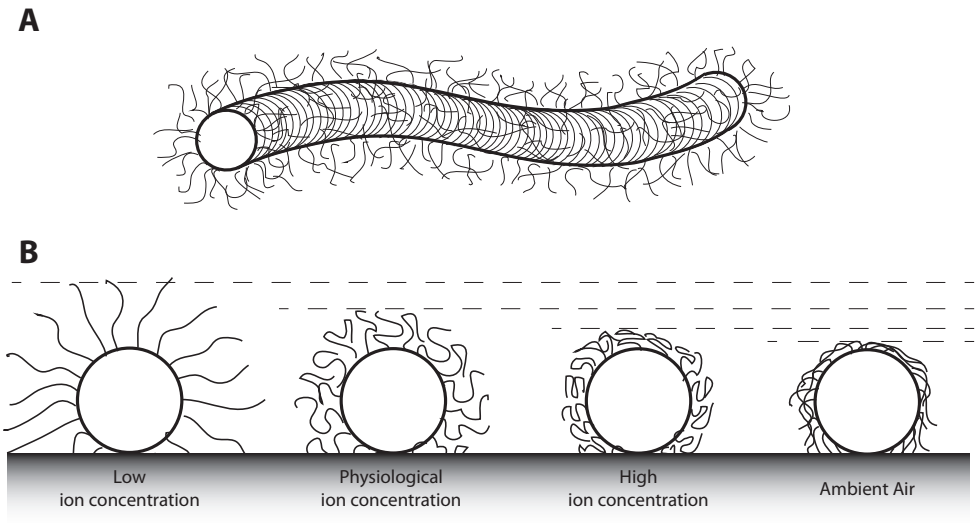

FIGURE 2; (A) Schematic representation of fibril with stacked β-sheet folded monomers perpendicular to the fibril axis and an unstructured C-terminus outside the fibril. (B) Different conformation of C-terminal tails outside the fibril core in liquid conditions with different ion concentrations and in ambient air.

MATERIAL & METHODS

EXPRESSION AND PURIFICATION OF ALPHA-SYNUCLEIN

We performed recombinant expression of wild type αSYN, the E46K disease mutant, and truncated αSYN(1-108) variants as described before [7,34]. The purification procedure of wild type and E46K αSYN is the same as previously reported [7].

However, for the 1-108 variant modifications in the standard purification protocol were essential. Firstly, the ammonium sulphate precipitate was dissolved in glycine pH 3.3 and the resulting protein solution was purified using a Resource S column (GE Healthcare Life Sciences, Little Chalfont, United Kingdom). Thereafter, the glycine buffer was exchanged with a desalting step for a 10 mM Tris-HCl pH 7.4 buffer.

AGGREGATION REACTION

For the height measurements in liquid and air 100 μM solutions of monomeric wild type, E46K and αSYN(1-108) in 10 mM Tris-HCl, 50 mM NaCl, pH 7.4 were incubated at 37°C in glass vials (duplicates) under constant shaking. The aggregation kinetics were monitored using a Thioflavin T fluorescence assay. Samples for AFM measurements were taken when the Thioflavin T fluorescence had just reached its maximum intensity [5,7].

For the height measurements at varying ion concentrations a second aggregation was performed for wild type αSYN in the same manner described above.

ATOMIC FORCE MICROSCOPY

AFM SAMPLE PREPARATION

AFM sample preparation was performed by placing 10 μl of a 5 times diluted protein solution on freshly cleaved mica and allowing it to adsorb for 2 minutes. The sample was washed gently with 200 μl MilliQ water and dried carefully under a gentle stream of nitrogen gas for imaging in air. For liquid imaging the sample was not allowed to dry, but was rinsed with the buffer solution. Around 100 μl of fresh buffer was placed on the sample prior to imaging.

AIR VERSUS LIQUID MEASUREMENTS

Atomic Force Microscopy images were made on a Bioscope II (Bruker, Santa Barbara CA, USA) equipped with a silicon probe (NSC36, MikroMasch, Tallin, Estonia) for topography imaging both in liquid and ambient air of the full-length and truncated variants. Imaging was performed in tapping mode in ambient air with low force settings (amplitude setpoint at 100 nm, 80-90% of the free amplitude) to minimize interaction with the sample. In liquid, the amplitude setpoint was set to 5 nm, which is 90-95% of the free amplitude. Resonant frequencies were 186 kHz in ambient air and 82 kHz in liquid, see Figure 3A.

HEIGHT MEASUREMENTS AT VARYING ION CONCENTRATIONS

For imaging the wild type fibrils at varying ion concentrations a custom-built AFM

system was used [35]. A silicon nitride MSCT probe, cantilever F (Bruker, Santa Barbara CA, USA) was used with a free amplitude between 1-2 nm (amplitude setpoint between 0.8-1.5 nm, 80-90% of the free amplitude). The sample is prepared as described above, however after adsorption the buffer was exchanged to a Tris-HCl buffer only. The ion concentration was then changed after imaging at least 60 fibrils that could be analyzed further. The buffer solution in which the sample is immersed was exchanged to a higher NaCl concentration and left to equilibrate for 30 minutes. At the higher ion concentrations the resonance frequency and the amplitude setpoint had to be adjusted due to the increase in density and viscosity to keep similar tapping amplitudes, see Figure 3B.

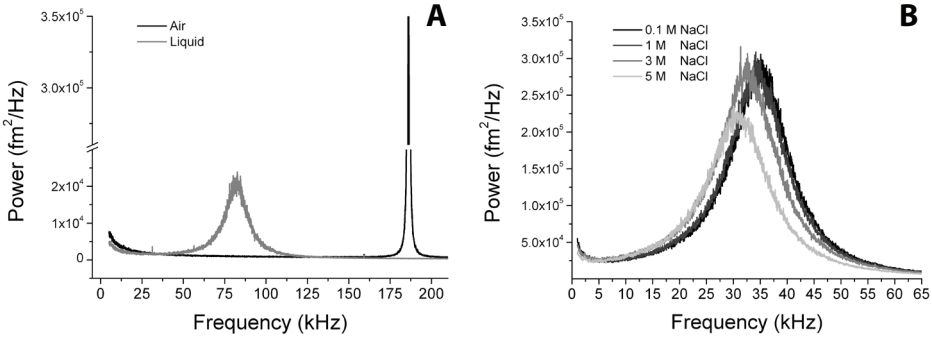

FIGURE 3; Frequency spectra of (A) NSC36 tip B in air and liquid, resonance frequency dropped from 186.1 kHz in air to 82.0 in liquid. (B) MSCT tip F in liquid in different ion concentrations. Black curve is in 10 mM Tris and 100 mM NaCl with a frequency of 34.9 kHz. Dark grey curve is at 1 M NaCl which gave a resonance of 34.2 kHz. 3 and 5 M NaCl gave both 2 kHz drops in frequency (32.4 and 30.7 kHz). The frequency is lowered due to the increased added mass (density increase) and the cantilever is also more damped (viscosity), resulting in a lower Q.

PEAKFORCE QNM MEASUREMENTS

Peakforce measurements were done on a Bruker Bioscope Catalyst microscope with a Nanoscope V controller (Bruker, Santa Barbara, CA, USA). The analysis software uses the DMT model [30]. The measurements the done in 0.1 M NaCl aqueous solution, 3M NaCl aqueous solution, and afterwards in ultrapure water. Buffer exchange was similar to the protocol described above in the varying ion concentration section. Previous Peakforce QNM studies on α-synuclein fibrils used a cantilever with a nominal spring constant of 2.8 N/m to determine the modulus of elasticity and maximum force setpoint of around 2 nN [21]. However, in this study we would like to measure the subtle differences in tip-sample interactions forces at different ion concentrations. Therefore, we use a less stiff cantilever MSCT tip F with a nominal spring constant of 0.5 N/m, and a force setpoint of only 500 pN to be sensitive to the tip-sample interaction forces rather than to the mechanical properties.

IMAGE MORPHOLOGY ANALYSIS

The heights of the protein fibrils were analyzed using SPIP software (Image Metrology A/S, Lyngby, Denmark) according to the procedure described in [7]. Only fibrils longer than 100 nm were included in the analysis.

RESULTS & DISCUSSION

WILD TYPE AND H08 ALPHA-SYNUCLEIN AGGREGATION

To obtain fibrils for wild type and E46K αSYN, and truncated αSYN(1-108), the monomeric protein was left to aggregate for 72 hours at 37° C. The aggregation kinetics were monitored using Thioflavin T (ThioT), which is a fluorescent dye that shows enhanced fluorescence upon binding to cross-β conformations characteristic of amyloid fibrils [36]. The aggregation reaction resulted in mature fibrils after 48 hours for both full-length and truncated variants, and was independently verified by AFM. In the ThioT intensity assay, a very small increase in ThioT fluorescence intensity was observed for the 1-108 variant compared to the full-length variants, see Figure 4. Previous studies have demonstrated that αSYN(1-108) aggregates significantly faster than wild type αSYN [16,34]. Although a lack of ThioT fluorescence is commonly interpreted as the lack of amyloid structure, it has been observed previously that not all amyloid stains efficiently with ThioT [37]. It is possible that the removal of the negative charges present on the C-terminus influence the electrostatic interaction of the positively charged ThioT with α-synuclein. The AFM data very clearly show fibrillar structure for both wild type and truncated protein; the latter have been demonstrated to have significant β-sheet content [16]. We thus believe the fibril cores for the wild type protein and the 1-108 variant to be similar. The αSYN(1-108) fibrils are considerably shorter than the wild type fibrils, but otherwise exhibited similar heights in liquid, (Figure 4 and Table 1). E46K αSYN formed fibrils in the same time frame as the wild type protein (kinetic data not shown).

AFM tapping mode images of fibrils formed with the full-length proteins and the truncated variant were recorded in buffer solution and ambient air conditions. Fibrils after 48 hours incubation were deposited on the surface and imaged. The measured heights for all variants and imaging conditions are listed in Table 1. Due to the very short lengths of fibrils formed by αSYN(1-108), it is difficult to obtain information on periodic height variations. In contrast, the wild type fibrils do show a height variation along their length with a periodicity of around 50 nm, while the twist found for the E46K variant was a little smaller, around 45 nm, which are similar to values reported previously [5,7].

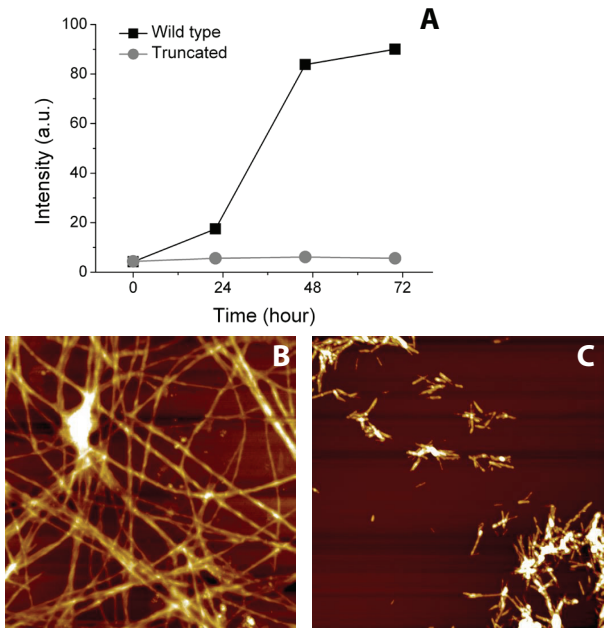

FIGURE 4: Aggregation of wild type protein and C terminally truncated αSYN(1-108). (A) Thioflavin T intensity curve shows hardly any intensity increase for αSYN(1-108). (B) Typical AFM image of wild type fibrils after 48 hours. (C) Typical AFM images of αSYN(1-108) fibrils after 48 hours. Both AFM images are 5x5 µm and z-range is 20 nm.

	Fibril height (nm) Liquid	*Fibril height (nm) Air*	*Height reduction (%)*
Wild type	7.9 ± 0.4 (N=150)	6.6 ± 0.9 (N=151)	16%
E46K	6.8 ± 1.3 (N=72)	5.6 ± 1.1 (N=62)	17%
1-108 A	7.6 ± 1.9 (N=105)	7.2 ± 1.8 (N=64)	5%
1-108 B	8.9 ± 2.3 (N=106)	8.7 ± 2.5 (N=72)	2%

TABLE 1: Fibril height data for wild type, E46K and αSYN(1-108) in two different scanning environments, liquid and ambient air. Height reduction is given in percentage of the height measured in liquid.

Fibril heights obtained for the wild type and E46K αSYN are similar to heights reported previously, see table 1 [5,7,20]. Whether the C-terminus of αSYN could serve as a polymer brush and thus increase the fibril height is not straightforward. The αSYN(1-108) duplicates differ by 1 nm in height, which led to the wild type αSYN heights being both higher and lower than those extracted from the individual measurement sets of the truncated variant. Murray et al. found no decreasing trend in αSYN fibril diameters with increasing C-terminal part truncation. They found a diameter decrease of around

3.8 nm for 1-110 αSYN compared to the full-length protein. However, the 1-130 variant was similar in size to 1-110 αSYN, while 1-120 αSYN showed an increase in diameter compared to both other truncated variants [16]. Zhang et al. found a 30% height decrease for both a C and an N-terminally truncated αSYN, however, the full-length fibrils already exhibited very low (6,5 nm) heights [19]. As seen in Figure 1, for wild type αSYN, the spread of fibril heights found by AFM or TEM is considerable. This variation is most likely partly due to differences in the structure of the fibrils as a result of different aggregation conditions like temperature, agitation methods, or buffers used. The other part is due to differences in AFM imaging conditions, such as the tapping amplitude, feedback settings, or environmental conditions. Even the choice of substrates onto which the fibrils are adhered could induce height differences [38]. Furthermore, the AFM tip radius can also influence height measurements, which are especially drastic for very small samples like DNA.

The differences in tip-sample interactions in ambient air and liquid conditions have been discussed in the literature [39]. One major difference is the thin water film on the substrate that is always present in dried samples (i.e. ambient air imaging) and whose thickness depends on the ambient humidity [40]. When imaging in liquid, the adhesion forces that the tip experiences is only from the interaction of the tip and the surface, while when imaging in air, the tip experiences an additional adhesion resulting from the capillary force of the thin water film. Furthermore, in liquid the Van der Waals forces are reduced ten-fold [39,41]. Both the absence of the water film and smaller Van der Waals forces in liquid allows for lower tapping amplitudes, and thus lower forces applied to the sample. The electrostatic forces depend on the charges of both the tip and the sample. In liquid this electrostatic interaction between the charges on the surface is modulated by counter-ions present in the solution, which form an electrostatic double-layer. This force can be tuned by changing the ion concentration in the solution [42].

The forces mentioned above influence fibril height measurements. We therefore systematically studied a number of different fibril samples (made from the full-length protein and the truncated version) using the same set of imaging parameters for all the measurements in air and another set of imaging parameters for all experiments in liquid. Different cantilevers are used for the air and liquid measurements. However, the were relatively blunt compared to the fibrils and were for all data sets around 85 ± 10 nm. Due to the larger sample size, around 8 nm, and the blunt tips with similar radii we assume the height difference effects between the different measuremetns caused by the tip-sample geometry, described by Santos *et al*, therefore similar for all datasets. This careful control of AFM settings allowed us to compare height reduction percentages between the different fibril species. The reduced fibril height obtained in air when

compared to a liquid environment is 17%, which is similar to that reported previously for paired helical filaments [24]. The 17% height reduction is attributed to the collapse of the C-terminus onto the fibril core upon drying (see Figure 2B). In contrast to the full-length fibrils we measured a negligible height reduction for the 1-108 variant. We believe that the fibril core of αSYN(1-108) is expected to have a similar structure to those formed from the full-length protein. Furthermore this structure is densely packed, leaving little room for water within the fibril core.

AFM MEASUREMENTS AT DIFFERENT ION CONCENTRATIONS; TAPPING MODE AND PEAKFORCE QNM

The strongly negatively charged C-terminus on the fibril exterior can be affected by the ionic strength of the buffer. When these negatively charged tails are charged and closely packed, the polymer brush, we expect the tails to stick out resulting in a larger fibril height. When the charges on the tails are screened the structure of the C-terminus is less affected by the neighboring tails resulting in a more condensed structure and thus a lower fibril height, see also Figure 2. To measure this effect we have measured the fibril heights as a function of ion concentration in the surrounding buffer. After initial deposition of the protein fibrils on the substrate the surrounding solution was exchanged with a 10 mM Tris-HCl buffer. AFM images were made of at least 60 fibrils. Next the buffer was exchanged to one with a higher NaCl concentration and left to settle as described in the material and methods and the same sample is imaged again. This was repeated for every ion concentration.

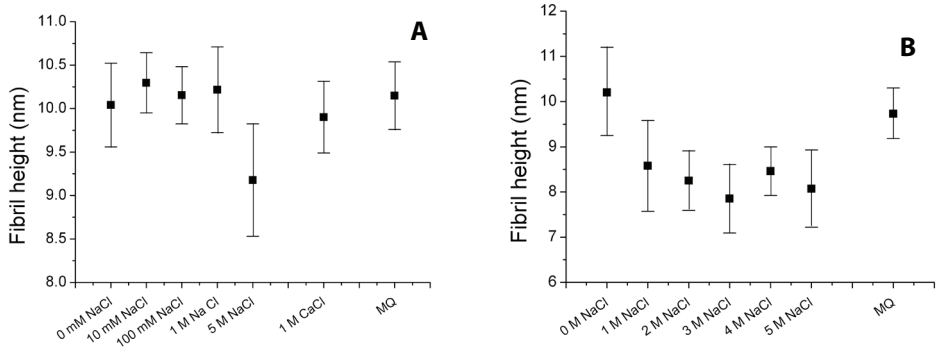

FIGURE 5; Wild type fibril heights at different ion concentrations. (A) Experiments at lower ion concentrations, where no differences in fibril heights are seen. A clear height difference is observed at 5 M NaCl and also a slight difference between 1 M NaCl and 1 M CaCl is seen. (B) Ion concentration series between 1 M and 5 M NaCl. The height reduction is reversible as shown by the last control experiment in MilliQ, which restores the height to the initial value.

As a first experiment, we varied salt concentrations from 0 to 1 M NaCl, for which the heights of the protein fibrils did not significantly change (Figure 5A). We then introduced 5 M NaCl; in these conditions the height of the fibril showed a clear decrease of more than 1 nm. We also observed a small fibril height difference of ~0.3 nm depending on whether 1 M monovalent or 1 M multivalent salts are used. In the second experiment we systematically explored higher salt concentrations, from 1M to 5M NaCl. As shown in Figure 5B, after 3 M NaCl there is no further height reduction found. To check whether these height differences are reversible, both experiments were terminated with measurements in ultrapure water, which restored the fibril height to the initial heights found at 0 M NaCl. Both experiments show a small variability between the same buffer conditions. Especially the difference at 1 M NaCl between both experiments is considerable. The small differences are maynly caused by the use of different AFM cantilevers which can influence the results slightly due to different contact areas leading to slight differences in tip-sample interactions. The 1 M NaCl concentration could be around the transition point where the ion-concentration is affecting the fibril height. It is a possibility that the local ion-concentration around the fibril for both esperiments were not the same causing the height difference between experiments at 1 M NaCl. At the higher concentrations, above 3 M NaCl, we do not observe any difference in height anymore. At these concentrations it is very well possible that the C-terminal tail is fully collapsed on the fibril due to salting-out of the protein

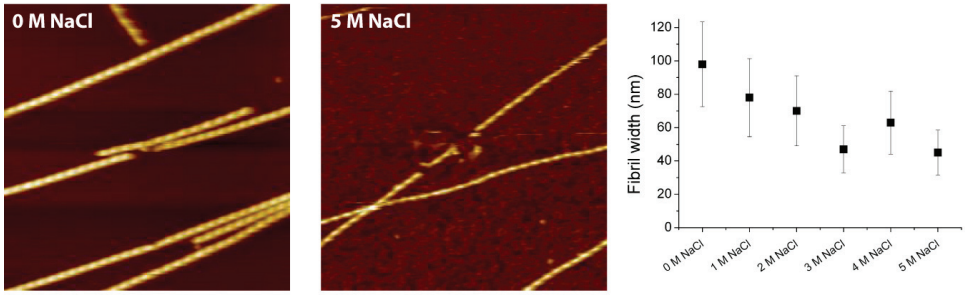

FIGURE 6; Typical images of wild type fibrils measured at 0 M and 5 M NaCl buffers and graph of fibril widths measured at different salt concentrations. The fibrils at 0 M NaCl appeared thicker compared to the fibrils measured at 5 M NaCl. Image size is 2x2 μm, 256 pixels and z-range of 20 nm.

We also observed an apparent increased lateral resolution of the images with increasing salt concentration (Figure 6). The fibrils not only decreased in height but also appeared thinner in the images, with diameters of on average 50 nm at above 2 M NaCl concentrations, compared to 100 nm at 0 M NaCl. The trend of decrease in fibril width is similar to the fibril height decrease seen in Figure 5B. The interaction between the tip and the fibril decreases the fibril height and therefore also the fibril width. However,

the fibril width decrease is more pronounced compared to the height (50 nm decrease between 0 M NaCl and 3 M NaCl). This extra width decreasing effect is caused by a decreased interaction between the negative tip and mica surface. On top of the fibril the interaction is only between the tip and the fibril, however at the sides of the fibril the interaction is a combination between tip, fibril and mica. At higher ion-concentrations, this makes it possible for the AFM tip to follow the surface and fibrils more closely, enhancing the apparent lateral resolution.

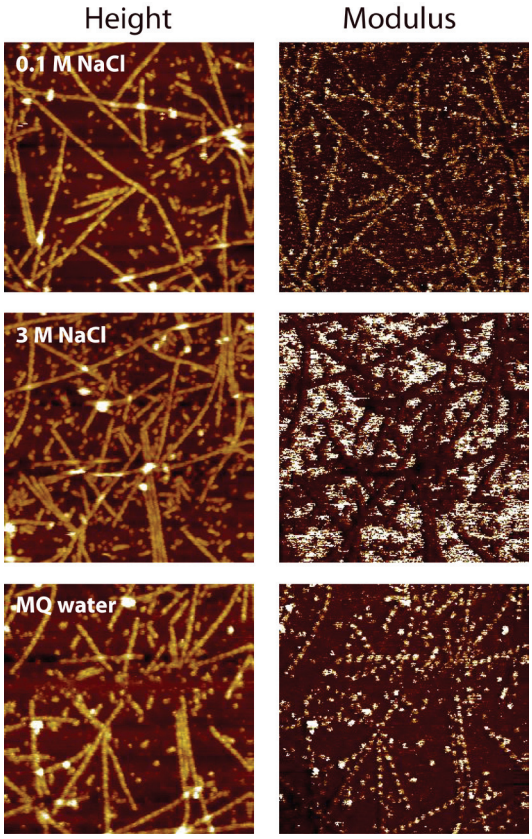

FIGURE 7; Height images and DMT modulus maps at the three different solution conditions. Images are 2x2 μm in size and Z-range of the height images are 20-40 nm. For 0.1 M NaCl (upper panel) and MilliQ water (bottom panel) the Z-range of the modulus map is 60 MPa, while for 3 M NaCl (middle panel) the Z-range is 500 MPa.

We also performed Peakforce QNM measurements of the same wild type fibril sample under two different ion concentration conditions, namely in Tris-HCl buffers containing 0.1 M NaCl and 3 M NaCl, and finally in ultrapure water. Peakforce QNM uses force-distance curves at a rate of 1 kHz to determine several properties like height, adhesion and DMT modulus [21,29]. The height images with corresponding DMT

modulus maps are displayed in Figure 7. The topography images show that the fibril heights are similar to those found with tapping mode. Also, the periodic height variations are visible. The DMT modulus maps show large differences between the 0.1 M NaCl and the high 3 M NaCl. The modulus value for the background mica changes from ~10 MPa at 0.1 M NaCl to ~500 MPa at 3M NaCl. This results in an apparent contrast inversion when increasing and decreasing the ion concentration. The modulus values of the fibrils at all three buffer conditions are similar. However, at 0.1 M NaCl (and also at 0M), the DMT modulus shows a variation along the fibril length, similar to that observed in topography, which is not observed in the presence of 3M NaCl.

Increasing ion concentration in the scanning buffer decreased the fibril height by 1 to 2 nm and increased the lateral resolution. This is potentially due to two different effects. Firstly, the ions shield the negative charges on the C-terminus, which decreases the repulsion between the different C-termini along the fibril length. This could cause the C-termini to collapse on to the fibril core. This observation could be due to the conformation of the C-terminus outside the fibril. Whether the C-terminus can actually serve as a polymer brush depends on the radius of gyration of the C-terminus and the surface area of the fibril. An αSYN fibril consists of β-strand folded monomers which are stacked perpendicular along the fibril length with 0.5 nm spacing, hydrogen bonds between the strands [43,44]. If we calculate the surface area of a small 0.5 nm in height cylinder with diameter of 10 nm, this surface area allows 2.6 to 3.9 nm^2 space per C-terminus. This depends on which packing model is used, 4 or 6 monomers per mature fibril. A 40 amino acid chain could have a radius of gyration from 1.6 nm up to almost 6 nm depending on the solvent conditions [45,46]. This indicates that we are at the boundary between a random coil and a polymer brush, where for different conditions the random coil formation of a C-terminal tail both does fit on the fibril core, leading to a random coil formation, or not which leads to a polymer brush conformation. Secondly, the increased ion concentration decreases the electrostatic double-layer repulsion forces between tip and sample. This phenomenon can also be seen in the Peakforce QNM measurements. Here, due to the increased repulsion force between the tip and sample at lower ion concentrations the negatively charged mica surface appears as soft as the fibrils. However, at the 3 M NaCl concentration, the mica appears stiffer compared to the fibrils. This effect has been shown before in various studies where the repulsion force is clearly influencing the slope of the force curve and is the same effect which causes the apparent lateral resolution in the high ion concentration tapping mode experiments [47-49]. Interestingly, the Peakforce QNM measurements also show, at low ion concentrations, variations along the fibril in both DMT modulus and adhesion, see Figure 8. At this point it is not clear whether this periodicity observed in the different channels is caused by the heterogeneity in the C-terminal brush or the contact area

between tip and sample or even a combination of both. However, with this mode it is maybe possible to shed light on the brush distribution from charge interactions or on the helical shape of the fibril from the tip-fibril contact area causing different adhesion forces.

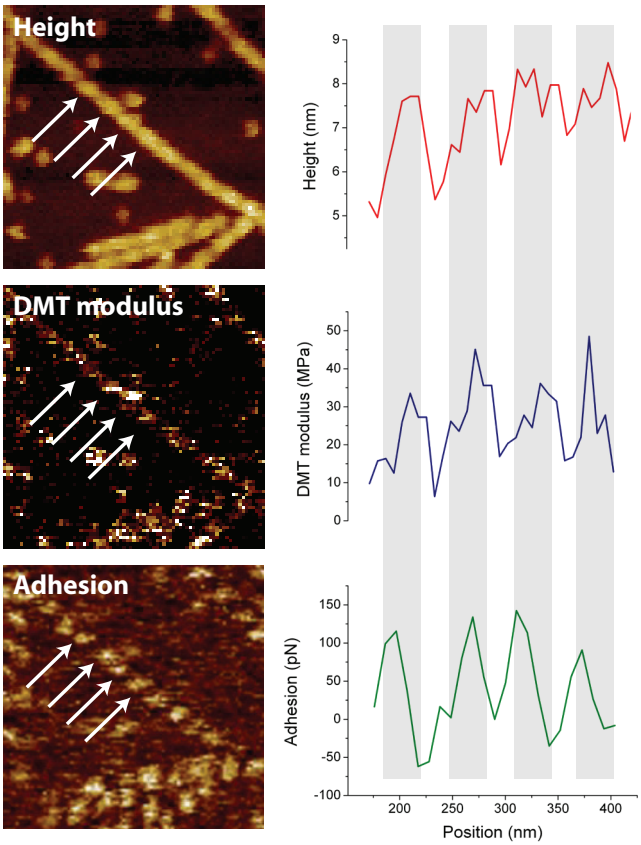

FIGURE 8; Height, DMT modulus, and adhesion map of fibrils measured at 0.1 M NaCl concentration with corresponding line profile over 4 periods of peaks and valleys of the fibril. Profiles indicate a higher DMT modulus and adhesion force at the peaks of the fibril compared to the valleys.

CONCLUSION

We observed that α-synuclein fibrils imaged in air appear around 17% lower in height compared to the same fibrils imaged in liquid environment. The truncated α-synuclein variant shows only up to 5% height decrease upon drying. This height difference of the α-synuclein fibrils is most probably the result by the collapse of the C-termini on the fibril core as the sample is dried.

Beside changes in the structure of the protein fibril as a result of a change in the environment, also the interactions between the tip and the sample does change for different environmental conditions which can lead to a different height when imaged with AFM. We show that the height decrease of α-synuclein fibrils imaged in different salt concentrations ranging from 0 to 5 M NaCl can be as much as 20%. This height decrease can be attributed to shielding of negative charge on the C-terminus. Aside from the height decrease the fibril appear also thinner due to different tip-sample interactions, especially between the tip and the mica surface. This effect is also shown with the recently introduced surface property mapping technique Peakforce QNM, where the mica surface has very different DMT moduli at different ion concentrations. Peakforce QNM measurements also revealed, in a nanoscale spatially resolved manner, different adhesion forces along the fibril axis. The higher adhesion forces at the peaks of the fibrils could indicate more C-terminal tails in the peaks compared to the valleys. This could indicate that the C-terminal brush on the fibril is either not evenly distributed along the fibril or that the monomers are differently orientated resulting in a heterogeneous brush.

Measuring morphological properties of amyloid fibrils with AFM should be done in liquid to avoid dehydration of the sample, depending on the humidity of the environment. Furthermore, the protein conformation might be more readily controlled under liquid conditions. However, even in liquid, comparison of results between protein fibrils is still influenced by environmental scanning conditions. However, we show that with careful consideration of all different parameters, both aggregation and AFM settings, these different results due to influences of scanning conditions can be used to determine structural and conformational information of biological samples at the nanoscale.

ACKNOWLEDGEMENTS

The authors thank Kirsten van Leijenhorst-Groener and Marloes ten Haaff-Kolkman for protein expression and purification.

REFERENCES

1. Gosal WS, Myers SL, Radford SE, Thomson NH. (2006) Prot. & Pept. Lett. 13:261-70
2. Knowles TPJ, Beuhler MJ. (2011) Nat. Nanotech. 6:469-79
3. Dobson CM. (2003) Nature 426:884-890
4. Schultz W. (2006) Proc. Natl. Acad. Sci. 103:1661-68
5. Segers-Nolten I, Van der Werf K, Van Raaij M, Subramaniam V. (2007) Proceedings of the IEEE Conf. Eng. Med. Biol. Soc. 6609-12

6. Khurana R, Ionescu-Zanetti C, Pope M, Li J, Nielson L, Ramirez-Alvarado M, Regan L, Fink AL, Carter SAA. (2003) Biophys. J. 85:1135-44
7. Raaij ME van, Segers-Nolten IMJ, Subramaniam V. (2006) Biophys. J: Biophys. Lett. 91:L96-L98
8. Apetri MM, Maiti NC, Zagorski MG, Carey PR, Anderson VE. (2006) J. Mol. Biol. 355:63-71
9. Barkhordarian H, Emadi S, Schulz P, Sierks MR. (2006) Prot. Eng. Des. Sel. 19:497-502
10. Bhak G, Lee S, Park JW, Cho S, Paik SR. (2010) Biomat. 31:5986-95
11. Conway KA, Harper JD, Lansbury Jr PT. (2000) Biochem. 39:2552-63
12. Crowther RA, Jakes R, Spillantini MG, Goedert M. (1998) FEBS letters 436:309-12
13. De Franceschi G, Frare E, Pivato M, Relini A, Penco A, Greggio E, Bubacco L, Fontana A, de Laureto PP. (2011) J. Biol. Chem. 25:22262-74
14. Gai WP, Pountney DL, Power JHT, Li QX, Culvenor JG, McLean CA, Jensen PH, Blumbergs PC. (2003) Exp. Neurol. 181:68-78
15. Kim HJ, Chatani E, Goto Y, Paik SR. (2007) J. Microbiol. Biotechnol. 17:2027-32
16. Murray IVJ, Giasson BI, Quinn SM, Koppaka V, Axelsen PH, Ischiropoulos H, Trokanowski JQ, Lee VMY. (2003) Biochem. 42:8530-40
17. Qin Z, Hu D, Han S, Hong D, Fink AL. (2007) Biochem. 46:13322-30
18. Volkova KD, Kovalska VB, Losytskyy MY, Veldhuis G, Segers-Nolten GMJ, Tolmachev OI, Subramaniam V, Yarmoluk SM. (2010) J. Fluoresc. 20:1267-74
19. Zhang F, Lin X, Ji L, Du H, Tang L, He J, Hu J. Hu H. (2008) Biophys. J. 368:388-94
20. Hoyer W, Antony T, Cherny D, Heim G, Jovin TM, Subramaniam V. (2002) J. Mol. Biol. 322:383-93
21. Sweers K, Werf K, Bennink M, Subramaniam V. (2011) Nanoscale Res. Lett. 6:270
22. Keller A, Fritzsche M, Yi Y, Liu Q, Li Y, Dong M, Besenbacher F. (2011) ACS Nano. 5:2770-78
23. Moreno-Herrero F, Perez M, Baro AM, Avila J. (2004) Biophys. J. 86:517-525
24. Chamberlain AK, MacPhee CE, Zurdo J, Morozova-Roche LA, Allen H, Hill O, Dobson CM, Davis JJ. (2000) Biophys. J. 79:3282-3293
25. Nikiforov MP, Thompson GL, Reukov VV, Jesse S, Guo S, Rodriguez BJ, Seal K, Vertegel AA, Kalinin SV. (2009) ACS Nano. 4:689-98
26. Song Y, Bhushan B. (2007) Ultramicroscopy 107:1095-1104
27. Goedert M. (2001) Nat. rev. neurosci. 2:492-501
28. Zarranz JJJ, Alegre JC, Gomez-Esteban E, Lezcano R, Ros I, Ampuero L, Vidal J, Hoenicka O, Rodriguez B, Atares V et. al. (2004) Ann. Neurol. 55:164–173
29. Pittenger B, Erina N, Su C. (2010) Application Note Veeco Instruments Inc
30. Derjaguin BV, Muller VM, Toporov YUP. (1975) J. Coll. Inter. Sci. 53:314-26
31. Young TJ, Monclus MA, Burnett TL, Broughton WR, Ogin SL, Smith PA. (2011) Meas. Sci. Technol. 22:125703(6pp)

32. Tan J, Saines PJ, Bithell EG, Cheetham AK. (2012) ACS Nano. 6:615-21
33. Adamcik J, Berquand A, Mezzenga R. (2011) Appl. Phys. Lett. 98:19370
34. Hoyer W, Cherny D, Subramaniam V, Jovin TM. (2004) Biochem. 43:16233-42
35. Van der Werf K, Putman C, de Grooth B, Segerink F, Schipper E, van Hulst N, Greve J. (1993) Rev. Sci. Instr. 64:2892-7
36. Ban T, Hamada D, Hasegawa K, Naiki H, Goto Y. (2003) J. Biol. Chem. 278:16462-5
37. Goldsbury C, Goldie K, Pellaud J, Seelig J, Frey P, Müller SA, Kistler J, Cooper GJS, Aebi U. (2000) J. Struct. Biol. 130:352-62
38. Van Noort SJT, van der Werf KO, de Grooth BG, van Hulst NF, Greve J. (1997) Ultramicroscopy 69:117-127
39. Weisenhorn AL, Hansma PK, Albrecht TR, Quate CF. (1989) Appl. Phys. Lett. 54:2651-3
40. Farshchi-Tabrizi M, Kappl M, Butt HJ. (2008) J. Adhesion Sci. Tech. 22:181-203
41. Goodman FO, Garcia N. (1990) Phys. Rev. B 43:4728-4731
42. Butt HJ, Capella B, Kappl M. (2005) Surf. Sci. Rep. 59:1-152
43. Villar M, Chou H, Luhrs T, Maji SK, Riek-Loher D, Verel R, Manning G, Stahlberg H, Riek R. (2007) Prot. Natl. Acad. Sci. 105:8637-42
44. Sunde M, Serpell LC, Bartlam M, Fraser PE, Pepys MB, Blake CCF. (1997) J. Mol. Biol. 273:729-39
45. Ghosh K, Dill KA. (2009) Prot. Nat. Acad. Sci. 106:10649-54
46. Fitzkee NC, Rose GD. (2004) Prot. Nat. Acad. Sci. 101:12497-502
47. Hoh JH, Revel J, Hansma PK. (1991) Nanotechnology 2:119-122
48. Senden TJ, Drummond CJ. (1995) Coll. Surf. 94:29-51
49. Ebeling D, van den Ende D, Mugele F. (2011) Nanotechnology 22:305706(10pp)

CHAPTER 6

Structural model for α-synuclein fibrils derived from high resolution imaging and nanomechanical studies using atomic force microscopy

A number of proteins form supramolecular protein aggregates called amyloid fibrils which self-assemble under appropriate conditions. We have used high-resolution atomic force microscopy to obtain detailed ultrastructural information on fibrils formed from the E46K mutant of the human α-synuclein protein, which is associated with Parkinson's disease. Two distinct fibril species were found; one with height of 6.0 nm exhibiting no periodicity along its length, and the other 7.4 nm high, revealing a periodicity of 46 nm, typical for the E46K mutant. We also determined the bending rigidity of these fibrils by analyzing the curvature of the fibrils from the 2D AFM images. By integrating the details of the fibril morphological features and their mechanical characteristics, we propose a structural model for α-synuclein fibrils, consisting of 6 filaments in two different packing configurations, consistent with the measured data.

Sweers KKM, Segers-Nolten IMJ, Bennink ML, Subramaniam V, Submitted to Soft Matter

INTRODUCTION

Several neurodegenerative diseases are accompanied by the appearance of protein deposits composed of fibrillar aggregates or amyloids in parts of the brain [1-3]. In Parkinson's disease the major component of these protein deposits, called Lewy bodies, is the protein α-synuclein [4-6]. α-Synuclein is a small protein of 140 amino acids that upon fibril formation adopts a cross-β structure oriented perpendicular to the fibril axis [7-9]. Although the process of fibril formation is apparently linked with the development of disease, the detailed mechanism of fibril formation has not yet been resolved.

Although all amyloid fibrils have similar gross morphological characteristics, the detailed substructure of the fibrils formed by different proteins is very diverse, a characteristic called polymorphism [10-13]. Fibrillar aggregates of a single protein species have also been found to display polymorphism [14]. Several morphological studies have been done on protein fibrils to investigate amyloid polymorphism in more detail [see for reviews references 10-13].

An explanation for amyloid polymorphism may be found by considering the different aggregation levels. First, the distinct morphologies found in the sample may be the result of specific lateral associations of protofilaments constituted of structurally identical monomers. In an AFM morphological study on β-lactoglobulin, five different fibril species containing different numbers of protofilaments were found [14]. Fibrils of various other proteins have also been proposed to be formed by lateral association of different numbers of filaments [15-19]. A few of these morphological AFM studies have yielded models describing the structure and assembly pathway of the fibrils from different proteins [15,20]. Second, the protofilaments may be composed of differently folded monomers, inducing morphological differences within one fibrillar population. Previous quantitative atomic force microscopy (AFM) studies described morphological characteristics of α-synuclein fibrils formed at different aggregation conditions or composed of disease-related mutants containing a single point mutation in the amino acid chain. The reported fibril heights vary from 7.5 nm to 10.4 nm; mutant-specific fibril periodicities have been observed [21-23]. Structural biology studies on the fold of the α-synuclein polypeptide and the fibril secondary structure yield inconsistent results. Solid state NMR on fibrillar α-synuclein has shown that the hydrophobic core region of the constituting primary amino acid chains is β-strand folded [8,24]. Based on variations in NMR spectra, one study identified two distinct fibril populations corresponding to two different fibril morphologies observed by EM [24]. Another solid state NMR spectroscopy report however proposes only a single fold for all morphologies [8]. The structure and assembly of alpha-synuclein fibrils thus remains an open question and is actively investigated by various spectroscopic techniques. [25-27]

In addition to the morphological and structural characteristics accessible to AFM or solid state NMR, the mechanical properties of fibrils also contain important information on the structure of the fibril. AFM bending experiments have been performed on biological nanostructures (~100 nm diameter), such as collagen fibrils [28], to derive Young's moduli [29,30]. Particularly for smaller diameter amyloid structures, like β-lactoglobulin and insulin fibrils, mechanical characteristics have been derived from the thermally induced shape fluctuations manifested in 2D AFM images. The bending rigidity and persistence length were derived from the average deviation of the fibril shape from a straight line connecting its ends using statistical mechanical theories of semiflexible polymers [31-36].

In this AFM study we used ultra-sharp probes for high resolution imaging of fibrils of the E46K mutant of α-synuclein. Fibrils of the E46K mutant are used because of their reproducible morphological characteristics. Two distinct fibril populations were found, one displaying no periodicity and the other with a periodicity of around 46 nm. We analyzed both fibril species for both their detailed morphology and their curvature in order to extract the bending rigidity. Based on the ultrastructural and mechanical information obtained from AFM images of the E46K fibrils we propose a general model for the structure of α-synuclein fibrils.

MATERIALS AND METHODS

EXPRESSION AND PURIFICATION OF ALPHA-SYNUCLEIN

Recombinant expression and purification of E46K disease mutant α-synuclein protein was performed as described previously [21].

AGGREGATION REACTION

A 100 μM monomeric E46K α-synuclein solution in 10 mM Tris-HCl, 50 mM NaCl, pH 7.4 was incubated at 37° C in glass vials under constant shaking. The aggregation kinetics was monitored using a Thioflavin T fluorescence assay. Samples for AFM measurements were taken when the Thioflavin T fluorescence had just reached its maximum intensity [21,22].

ATOMIC FORCE MICROSCOPY IMAGING

AFM sample preparation was performed by placing 4 μl of a 5 times diluted protein solution on freshly cleaved mica and allowing it to adsorb for 2 minutes. The sample was washed gently with 200 μl MilliQ water and dried carefully under a gentle stream

of nitrogen gas.

Atomic force microscopy images in ambient conditions were made on a custom built instrument equipped with an ultra-sharp silicon probe with a diamond-like tip (DP18, HI'RES series, 3.5 N/m, 1 nm nominal tip radius, (MikroMasch, Tallinn, Estonia)) and with a silicon nitride probe (MSCT, tip F, 0.5 N/m, 10 nm nominal tip radius (Bruker, Santa Barbara CA, USA)). Imaging was performed in tapping mode in ambient air with low force settings (reduced to 100 nm, 80-90% of the free amplitude) to minimize interaction with the sample.

Atomic force microscopy images in liquid were made on the Bioscope Catalyst (Bruker, Santa Barbara CA, USA) with the same cantilever as in air; MSCT silicon nitride probe (MSCT, tip F, 0.5 N/m, 10 nm nominal tip radius (Bruker, Santa Barbara CA, USA)). The same low force settings are used in liquid as in ambient conditions. The amplitude in liquid was 2-3 nm compared to 100 nm in air.

The actual tip radius was derived from the fibril height to width ratio of fibrils oriented perpendicular to the scan direction based on tip-sample convolution.

IMAGE MORPHOLOGY ANALYSIS

Fibrils were analyzed for their heights, periodicities and modulation depths using SPIP software (Image Metrology A/S, Lyngby, Denmark) according to the procedure described in [21]. Only fibrils longer than 10 times the periodicity (around 500 nm) were included in the analysis.

BENDING RIGIDITY

For the bending rigidity analysis 2D fibril traces were prepared manually using ImageJ software (Wayne Rasband, National Institutes of Health, Bethesda, MD, USA). Only intact fibrils of at least 1 μm in length, not crossing other fibrils or particles that may influence the fibril shape, were included in the analysis.

The bending rigidity (κ) of the semiflexible α-synuclein fibrils was derived from the average magnitude of the thermally induced shape deviations from the straight line connecting the end points [31,34,35] according to the following equation:

$$\kappa = k_B T \times \frac{L^3}{48\langle v(x)^2 \rangle} \qquad (1)$$

where kB is the Boltzmann constant, T the temperature in Kelvin, L the contour length of the fibril and v(x) is the distance from the midpoint the fibril segment to the

secant line of the fibril segment.

If the interaction between the protein fibrils and the substrate is too strong, the bending rigidity might be underestimated. This trapping effect has also been shown for DNA and intermediate filaments [32,37]. However for amyloid fibrils no trapping effect has been reported when deposited on mica [31].

From the bending rigidity the Young's modulus, E, is calculated using Eq. 2, where I is the moment of inertia.

$$E = \frac{\kappa}{I} \tag{2}$$

The moments of inertia were calculated by modeling the individual monomers as circles according to the hierarchical assembly model (HAM, see Figure 4) with Eq. 3, where A is the surface area of the circle and d the distance of the centroid of the surface area to the origin (middle of the complete structure).

$$I = \frac{\pi r^4}{4} + Ad^2 \tag{3}$$

RESULTS

FIBRIL MORPHOLOGY ANALYSIS

We compared the use of ultra-sharp and standard tips for the analysis of fibril morphology from AFM images. The tip radii, derived from the AFM images using deconvolution, were 34.7 ± 11.3 nm for the MSCT probe and 9.9 ± 3.9 nm for the ultra-sharp DP18 probe. Figure. 1 clearly indicates the higher lateral resolution obtained with the DP18 probe (Figure 1B) in comparison to the MSCT probe (Figure 1A), as shown quantitatively in the height profiles (Figure 1C). The apparent width of the fibril with periodic morphology from Figure 1C is 34 nm with the DP18 probe compared to 55 nm with the MSCT probe, both measured at a position with maximum fibril height (9 nm). Where the MSCT probe demonstrated only a periodic fibril appearance, the ultra-sharp DP18 probe additionally clearly revealed a right-handed twist, consistent for all periodic fibrils imaged.

Both AFM probes revealed the presence of populations of fibrils displaying periodicity (~60%) and with no periodicity (~40%) (Figure 1). We analyzed the periodic fibrils for their height, modulation depth and periodicity. The non-periodic fibrils were only analyzed for their heights (Table 1). A minor drawback of the ultra-sharp DP18

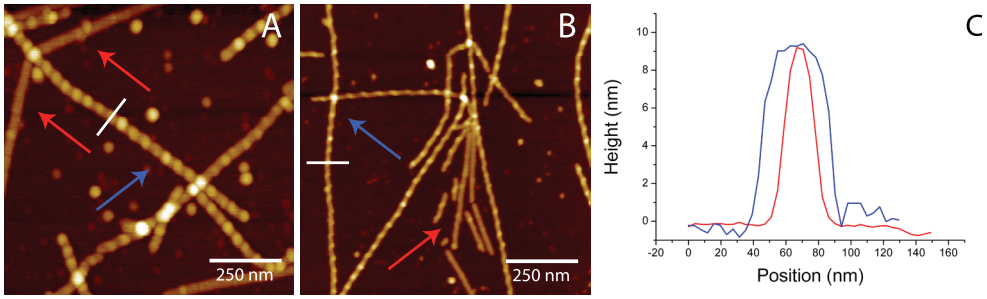

FIGURE 1; Representative AFM images of E46K α-synuclein fibrils from the same sample scanned with (A) the MSCT probe and (B) the HI'RES DP18 probe. The AFM images displaying periodic (blue arrows) and non-periodic E46K α-synuclein fibrils (red arrows). (C) Height profiles of equivalent fibrils obtained with the DP18 (red) and MSCT (blue) probe. The images are 1 x 1 μm , 256 x 256 pixels.

Probe	*DP18 Air*	*MSCT Air*	*MSCT Liquid*
Periodic fibrils	*(n=12)*	*(n=26)*	*(n=53)*
*Average fibril height**	7.4 ± 0.5 nm	8.2 ± 0.2 nm	8.9 ± 0.6 nm
Peak height†	8.4 ± 0.6 nm	8.7 ± 0.3 nm	9.4 ± 0.6 nm
Modulation depth‡	2.0 ± 0.4 nm	1.7 ± 0.2 nm	1.7 ± 0.5 nm
Periodicity†	46 ± 6 nm	46 ± 9 nm	55 ± 15 nm
Non-periodic fibrils	*(n=12)*	*(n=24)*	*(n=29)*
*Fibril height**	6.0 ± 0.4 nm	6.1 ± 0.3 nm	6.6 ± 1.4 nm

TABLE 1; Quantitative comparison of E46K α-synuclein fibril morphology obtained with different AFM probes in ambient air and liquid. Statistical difference between probe results: * $p<0.001$ † $p<0.5$ ‡ $p<0.01$ (wilcoxon signed-rank test)

probe is the fragility of the probe. Therefore, only a few images were recorded which resulted in only 12 measurable fibrils per population.

Quantitative analysis of the periodic population revealed comparable peak heights and periodicities when imaged with two different probes. Both these fibril characteristics were expected to be indeed independent of tip diameter. However, the average fibril height for periodic fibrils is lower when measured with the DP18 probe than with the MSCT probe. Also, the modulation depth is larger when imaged with the sharper DP18 tip. This indicates not only an improvement in the lateral resolution but also in axial resolution using ultra sharp tips to image the α-synuclein fibrils. The tip diameter of the MSCT probe (~70 nm) is large compared to the fibril periodicity (46 nm). Although the tip is still suitable to probe fibril periodicity, it is not able to reach the lowest point of the modulation completely. This results in an overestimation of the average fibril

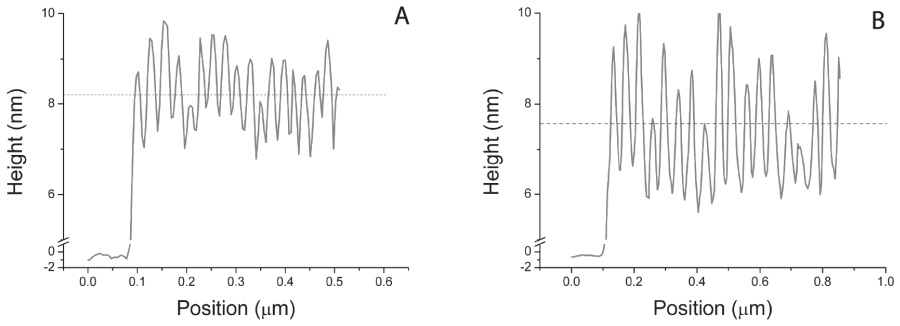

FIGURE 2; Representative height profiles of fibrils imaged with the MSCT probe (A) and DP18 probe (B). The dashed lines represent the average fibril heights, which is considerably lower for the DP18 probe due to the higher modulation depth (see also Table 1).

height. However, the DP18 probe with a diameter (~20 nm) of less than 50% of the fibril periodicity is more likely to reach this lowest point, resulting in more accurate determination of the average height and modulation depth. The fibril height profiles shown in Figure 3 clearly demonstrate a larger modulation depth and associated lower average fibril height when imaged with the sharper DP18 probe.

Identical heights were measured for non-periodic fibrils with both probes (Table 1). The heights were approximately 70% of the peak heights of periodic fibrils. The fibrils measured in liquid all show a slight height increase of 10% (Table 1) with Gaussian distributions (supplementary section).

ANALYSIS OF FIBRIL BENDING CHARACTERISTICS

We determined the contours for both periodic and non-periodic fibrils from the AFM images. Only fibrils longer than 1 μm and not crossing other fibrils or particles are used for this analysis. The curvature of this contour reflects the bending rigidity, a parameter that describes the type of interactions that stabilize the fibrils. We included data obtained with both the DP18 and MSCT probes because resolution is not a critical parameter in this analysis. In the determination of the Young's modulus we considered the non-periodic fibrils as single circular rods and the periodic fibrils as two intertwined circular rods (protofibrils) according to the HAM model [20]. The required moments of inertia were computed using the radii that followed from the AFM height measurements: 3.0 nm for the non-periodic fibrils and 2.1 nm for each of the two protofibrils constituting a mature periodic fibril (Table 2).

The bending rigidities for periodic and non-periodic fibrils were not significantly different ($p<0.5$). The bending rigidities obtained of α-synuclein fibrils are, including the rather large errors, in the same range as those determined for the extremely stiff

amyloid fibrils formed by the short TTR peptide from transthyretin [31]. Among the population of natural non-amyloid polymers, tubulin filaments have a bending rigidity comparable to α-synuclein fibrils [38]. With their relatively large radius the non-periodic fibrils have a greater moment of inertia, and thus a larger Young's modulus, than a single thinner protofibril within a periodic fibril.

The bending rigidities found for the E46K fibrils measured in liquid were 5.3 x 10^{-24} Nm^2 for periodic fibrils and 5.7 x 10^{-24} Nm^2 for the non-periodic fibrils. These values are also not significantly different ($p<0.45$). The bending rigidity analysis was also per-

		Periodic Fibrils	*Non-periodic Fibrils*
Bending Rigidity, κ	*(Nm^2)*	1.49 x 10^{-24}	1.57 x 10^{-24}
Moment of inertia , I	*(m^4)*	9.16 x 10^{-35}	6.36 x 10^{-35}
Young's modulus, E	*(GPa)*	16	24.7

TABLE 2; Mechanical properties of E46K α-synuclein fibrils derived from AFM images. Bending rigidity values from the AFM images, moment of inertia from the morphological analysis according to the HAM model and the Young's modulus calculated with both bending rigidity and moment of inertia according to equation (2). Periodic fibrils n = 50, non-periodic n = 33.

formed on wild-type α-synuclein. Here also both populations show similar bending rigidities (comprehensive data in Table S1, supplementary section).

DISCUSSION

FIBRIL MORPHOLOGY

The quantitative E46K α-synuclein fibril morphology data we obtained with either tip are in agreement with previous studies [21-23]. However, the average periodic fibril height measured with the DP18 probe is considerably lower. Obviously the DP18 probe diameter is small enough to better represent the modulation profile of the fibrils, resulting in a more accurate height measurement. This is supported by the fact that the modulation depth measured in air with the MSCT probe is 19% compared to 24% measured with the DP18 probe. Also, the DP18 images clearly reveal a twisted fibril appearance, information that cannot be extracted from images obtained with the larger diameter MSCT probe.

The fibril heights measured in air were lower than the heights measured in liquid by ~10%. This difference is slightly lower than that measured previously on Alzheimer paired helical filaments [39]. The measured height reduction in air is most likely caused

by drying artefacts of the fibrils and different AFM tapping conditions [39,40]. The modulation depth measured in liquid is also only 18% of the peak height, comparable to the measurements in air. Furthermore, the relative heights of periodic and non-periodic fibrils are similar to those found with the MSCT probe in air. This observation is consistent with drying effects which are similar for both fibril populations. The average fibril periodicity measured in liquid is also larger than the periodicity measured in air. The error range of the periodicity in liquid is considerably larger than that in air, and the air measurements do fall within the error range of the liquid measurements. Recently, evidence was found that periodicities of fibrils are influenced by buffers of different ionic strengths [41]. Although fibril preparation was identical for all measurements, the sample preparation for liquid and air samples is different. The difference in periodicity could thus be caused by drying artefacts or local changes of ionic strength due to evaporation during the liquid measurements [41].

Detailed images of non-periodic fibrils show irregular height fluctuations (Figure 3).

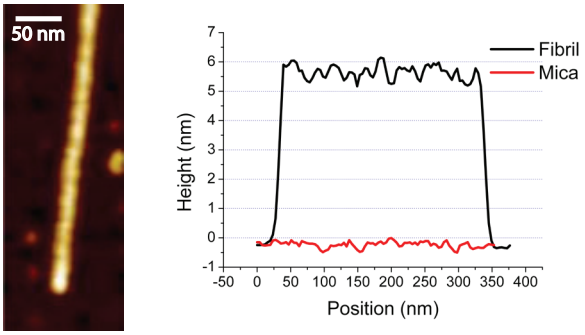

FIGURE 3; Detailed AFM height image and height profile of a non-periodic fibril obtained with the DP18 probe. Comparing the height profile of the fibril to the noise level measured on mica the profile of the non-periodic fibril suggests morphological features along the fibril height.

These height fluctuations are larger than the noise level of the AFM system and are only seen with the DP18 probe. Presumably, the assembly mechanism of the non-periodic fibrils results in small height fluctuations, clearly different from those observed in the periodic fibrils.

FIBRIL MECHANICAL CHARACTERISTICS

In search for additional information on the fibrillization mechanism, we analyzed the contours of the imaged fibrils in order to extract the bending rigidities. The very similar bending rigidities obtained suggest similar moments of inertias for the periodic and non-periodic fibrils. Assuming hierarchical assembly for the periodic fibrils, the

observed differences in fibril radii however lead to a different moment of inertia for each fibril population. Consequently, the Young's modulus of the periodic fibrils is with 16 GPa in the range of insulin amyloid fibrils and spider silk [36,42,43], while the modulus of the non-periodic fibrils is significantly higher (24.6 GPa). The bending rigidities measured in liquid leads to even larger increases in the Young's moduli. However, the difference between periodic and non-periodic fibril populations in solution did not change.

The calculated Young's moduli are dependent on the assumption that the fibrils are able to equilibrate on the surface. This equilibration process could easily be interrupted by fibrils touching each other or by shear forces during the drying process. However, in this study the preparation of the samples is the same and therefore all influences are the same for both fibril populations. Therefore, we believe it is valid to compare the Young's moduli for both populations. Considering our morphological and mechanical data, a self-consistent analysis can only be accomplished by assuming a different packing model that implies similar moments of inertia for both fibril types.

ALPHA-SYNUCLEIN PACKING MODEL

COMPARISON TO HIERARCHICAL ASSEMBLY MODEL

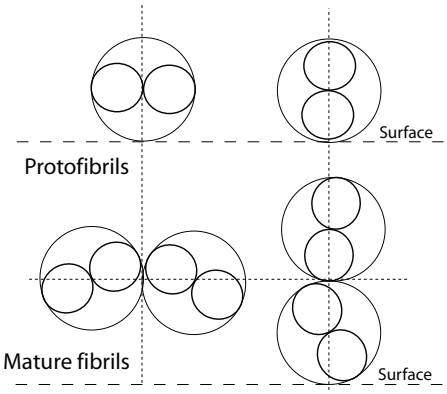

FIGURE 4; Schematic cross-sectional representation of the hierarchical assembly mod-el as proposed for α-synuclein fibril formation. Different possible orientations of the twisted fibrils with respect to the surface are represented, where the horizontally aligned twist section is assumed to be freely suspended in air. The horizontally aligned twist section is supported by adjacent vertically aligned twist sections which are adsorbed to the surface.

From the different existing models derived from morphological data, the hierarchical assembly model (HAM) is the prevalent model for α-synuclein [20]. This model suggests that at first a pair of thin protofilaments, consisting of stacked β-sheet structured

monomers, intertwine to form a protofibril, followed by twisting of two protofibrils to form a mature fibril (Figure 4).

Both our morphological and mechanical data are inconsistent with this model. The non-periodic fibrils are too high with respect to the periodic fibrils to be the protofibrillar species. Also, the equal bending rigidities found for periodic and non-periodic fibrils are not in agreement with the hierarchical assembly model. If the periodic fibrils consist of a pair of twisted non-periodic protofibrils, then the periodic fibrils are expected to have a two-fold higher bending rigidity than the non-periodic fibrils, assuming that the protofibrils within the periodic fibril are strongly bound. Even if the protofibrils are loosely bound the bending rigidity is expected to be 1.5-fold larger, and is called the wired rope effect [44].

Interestingly, the non-periodic fibrils were found at all stages of the aggregation process. However, if they were to be considered as protofibrils, these non-periodic structures would be expected to be absent in the later stages of aggregation because of complete association to form mature fibrils. Finally, we have never been able to image species that would correspond to the smaller diameter protofilaments constituting the protofibrils according to the hierarchical assembly model [20].

NEW PACKING MODEL

We hypothesize that the two fibril populations found are end products of different filament assembly pathways. We thus explored different filament packing possibilities yielding comparable moments of inertia and, by extension, similar Young's moduli (Figure 5). The configurations presented in Figure 5, panel E, represent a novel filament assembly model for α-synuclein fibrils that matches both our morphological data obtained with the ultra-sharp DP18 probe and the mechanical data. The comparison between morphological and mechanical measurements in ambient air and liquid showed that all drying effects are similar for both fibril populations. This observation allowed us to use the data from the ultra-sharp DP18 probe measured in ambient air to compose the new packing model. The similar bending rigidities for periodic and non-periodic fibrils from both the wild-type and the E46K disease mutant α-synuclein further suggests that this packing configuration could be a general feature for human α-synuclein fibrils.

We propose a packing model in which both periodic and non-periodic fibrils are composed of 6 differently arranged subfilaments (Figure 6). We assume the interactions between the monomers, linking the different filaments, to be the same in both situations. We continue to assume that the periodic fibrils are formed from a twisted pair of protofibrils. Now however, one protofibril consists of 3 subfilaments with circular cross sections, in contrast to 2 filaments in the hierarchical assembly model. The

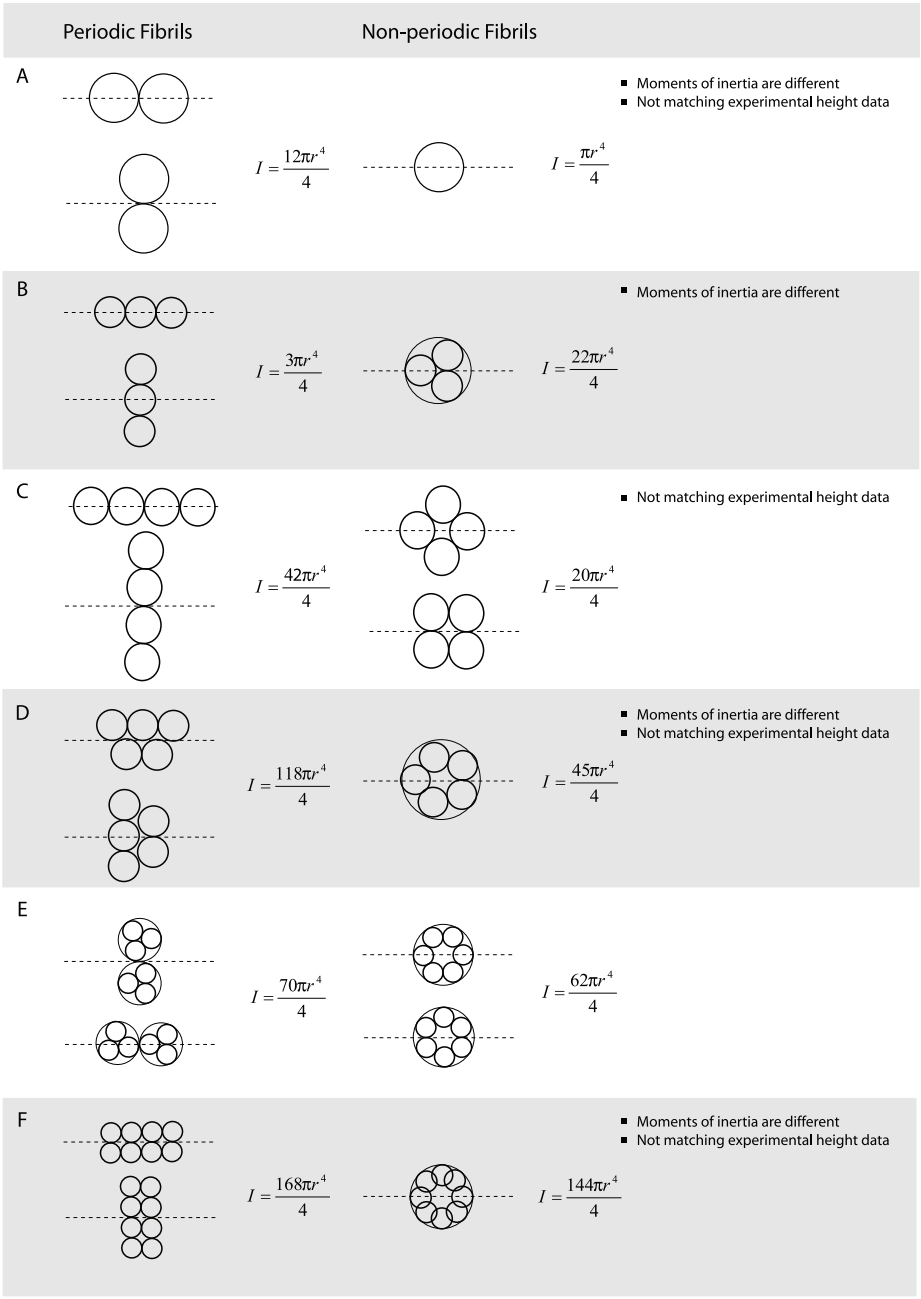

FIGURE 5; Different packing situations with corresponding moments of inertia, with r the filament radius. We depicted two criteria; firstly the conformation should give similar moments of inertia for the periodic and non-periodic fibril, secondly the conformations should fit the experimental morphological data. Model (E) is the only packing model matching both our morphological and mechanical data.

assumption of a twisted arrangement is essentially based on the morphology clearly revealed by the ultra-sharp DP18 probe. The expected modulation depth is 25% of the

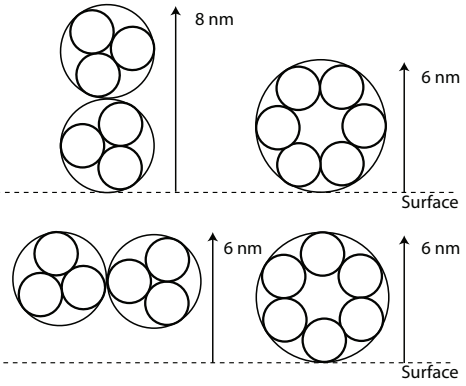

FIGURE 6; Cross-sectional filament packing model based on packing of 6 filaments, left are the periodic fibrils and right the non-periodic fibrils. Heights are indicated assuming a 1 nm filament radius, which fits the experimental morphological data. As shown in Figure 5 the moments of inertia are similar for both fibrils and this results in similar Young's moduli for both periodic and non-periodic fibrils.

peak fibril height, assuming free suspension from the mica at the fibril trough positions. This is in close agreement with the 24% modulation depth measured with the DP18 probe. The non-periodic fibrils are composed of 6 circularly arranged subfilaments. Still, the fibril may grow in a twisted fashion along its longitudinal axis. This twist could be responsible for the 0.5 nm height fluctuations found for the non-periodic species with the ultra-sharp DP18 probe.

With a radius of 1.0 nm for the individual subfilaments, our proposed model results in a peak height for the periodic fibrils of 8 nm and a fibril height of 6 nm for the non-periodic fibrils (Figure 6). These predictions are in good agreement with the measured data (Table 1). Based on these dimensions, the proposed assembly arrangement results in moments of inertia of around $4.9\text{-}5.5\times10^{-35}$ m^4 for both fibril populations. Then, the associated Young's moduli are 27.1 and 32.0 GPa for the periodic and non-periodic fibrils respectively. Apparently, the proposed configuration of subfilaments results in even higher Young's moduli than the hierarchical assembly model, indicating that circular subfilament cross-sections assumed may not be realistic.

Recently, NMR studies on α-synuclein amyloid identified five β-strands within the part of the folded monomer contained in the fibril core comprising residues 35 to 96 [8,24]. The lengths of the individual β-strands were calculated to be 1.8 nm for the shortest first strand and 3.9 nm for the longest last strand [8]. These strands are

folded in a trapezoid arrangement. To estimate a more realistic diameter for the E46K α-synuclein protofibrils, the distance between the intramolecular folded β-strands is required. In X-ray diffraction patterns of wild-type α-synuclein fibrils a weak reflection in the 1-1.1 nm region was interpreted as the intramolecular intersheet spacing of the β-sheets. However, for disease mutant α-synuclein fibrils no such diffraction could be detected [7]. Therefore, we assume optimal packing of β-strands, with the amino acid side chains protruding from the sheets forming a dry, tightly self-complementing steric zipper [45-47]. Accordingly, computation of distances between the β-strands from the dimensions of the amino acids, results in a minimum height of ~2.3 nm per monomer. These new trapezoid dimensions give a higher surface area, resulting in a larger moment of inertia. With these new moments of inertia for both periodic and non-periodic fibrils the Young's modulus was recalculated to be ~9 GPa, which is more realistic and well in the range of Young's moduli previously found for amyloid structures.

We note that solid-state NMR and EPR measurements have begun to address the fold of the protein within the fibrils [8,25,48-50], but do not yet provide unequivocal ultrastructural insights into the packing and assembly of α-synuclein fibrils. In the absence of detailed structural information on α-synuclein fibrils, we believe that the approach described in this manuscript, considering nanometer-scale morphological and mechanical properties in an integrated fashion, offers a viable alternative to derive information on the structure and assembly of amyloid fibrils.

CONCLUSION

We propose an alternative model for α-synuclein fibril assembly based on analysis of ultra high-resolution AFM data, integrating morphological fibril characteristics and associated mechanical properties. We used ultra-sharp AFM probes to enable extracting accurate data as a reliable basis for our model. The model describes a novel assembly mechanism where the subfilaments have different lateral associations for the different fibril morphologies observed, structures that cannot be explained by the previously proposed hierarchical assembly model.

Recently, evidence was found that α-synuclein associates with cytoskeletal components [51-53], like actin filaments (1.8 GPa) [54,55], microtubules (0.6 GPa) [38, 56] and intermediate filaments (6.4 MPa) [57]. The Young's moduli of these biopolymer structures are at least 5 times smaller than those obtained for α-synuclein fibrils. We speculate that amyloid fibril formation could therefore have a large impact on cellular constituents and processes, thereby contributing to the development of disease.

SUPPLEMENTARY MATERIAL

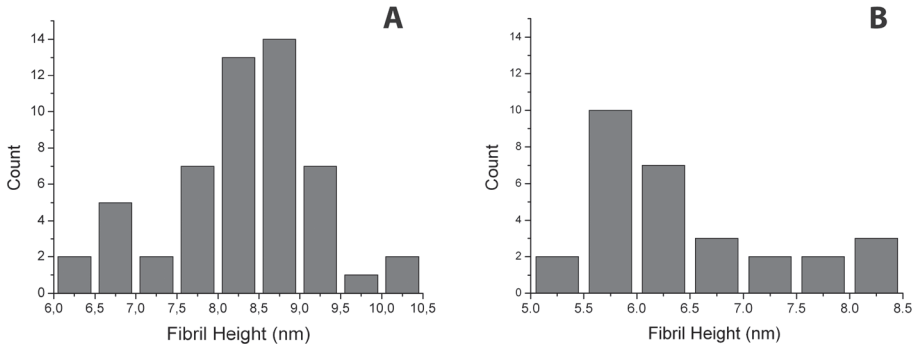

FIGURE S.1 Height distributions of periodic (left) and non-periodic fibrils (right)

Probe	*MSCT Air*
Periodic fibrils	*(n=42)*
*Average fibril height**	9.3 ± 1.2 nm
Periodicity	79 ± 7 nm
Bending rigidity†	8.25 x 10^{-24} Nm^2
Non-periodic fibrils	*(n=22)*
*Fibril height**	8.1 ± 1.7 nm
Bending rigidity†	9.6 x 10^{-24} Nm^2

TABLE S.1 Morphological and bending rigidity data of wild-type α-synuclein fibrils. Statistical difference between periodic and non-periodic fibril height and bending rigidity respectively: * $p < 0.01$, † $p < 0.5$ (Wilcoxon signed-rank test)

REFERENCES

1. Dobson CM (2003) Nature 426: 884-890
2. Sipe JD, Cohen AS. (2000) J.Struct. Biol. 130:88-89
3. Chiti F, Dobson CM. (2006) Annu. Rev. Biochem. 75:333-366
4. Schultz W. (2006) Proc. Natl. Acad. Sci. 103:1661-1668
5. Goedert M. (2001) Nat. Rev. Neurosci. 2 492-501
6. Uversky VN, Fink AL. (2005) from: Mechanisms in Parkinson's Disease pp 1-30
7. Serpell LC, Berriman J, Jakes R, Goedert M, Crowther RA. (2000) Proc. Natl. Acad. Sci. 97:4897-4907
8. Vilar M, Chou H, Luhrs T, Maji SK, Riek-Loher D, Verel R, Manning G, Stahlberg H,

Riek R. (2008) Proc. Natl. Acad. Sci. 105:8637-8642
9. Li L, Darden TA, Bartolotti L, Kominos D, Pedersen LG. (1999) Biophys. J. 76:2871-2878
10. Makin O, Serpell LC. (2005) FEBS Journal 272:5959-61
11. Fändrich M, Meinhardt J, Grigorieff N. (2009) Prion 3:2 89-93
12. Kodali R, Wetzel R. (2007) J. Structt Biol. 17:48-57
13. Kumar S, Udgaonkar JB. (2010) Current Science 98:5 639-56
14. Adamcik J, Jung J, Flakowski J, De Los Rios P, Dietler G, Mezzenga R. (2010) Nature Nanotech. 5:423-428
15. Jansen R, Dzwolak W, Winter R. (2005) Biophys. J. 88:1344-1353
16. De Jong KL, Incledon B, Yip CM, DeFelippis MR. (2006) Biophys. J. 91:1905-14
17. Dong M, Hovgaard MB, Xu S, Otzen DE, Besenbacher F. (2006) Nanotechnology 17:4003-09
18. Kad NM, Myers SL, Smith DP, Smith DA, Radford SE, Thomson NH. (2003) Biophys. J. 88:1344-53
19. Anderson M, Bocharova OV, Makarava N, Breydo L, Salnikov VV, Baskakov IV. (2006) J. Mol. Biol. 358:580-596
20. Khurana R, Ionescu-Zanetti C, Pope M, Li J, Nielson L, Ramirez-Alvarado M, Regan L, Fink AL, Carter SA. (2003) Biophys. J. 85:1135-1144
21. Raaij ME van, Segers-Nolten IMJ, Subramaniam V. (2006) Biophys. J. Biophys. L. L96-L98
22. Segers-Nolten I, Van der Werf K, Van Raaij M, Subramaniam V. (2007) 29th Annual International Conference of the IEEE EMBS 6608-6611
23. Hoyer W, Antony T, Cherny D, Heim G, Jovin TM, Subramaniam V. (2002) J. Mol. Biol. 322: 383-393
24. Heise H, Hoyer W, Becker S, Andronesi OC, riedel D, Baldus M. (2005) Proc. Natl. Acad. Sci. 102:44 15871-76
25. Comellas G, Lopez JJ, Nieuwkoop AJ, Lemkau LR, Rienstra CM (2011) J. Magn. Res. 209:131-35
26. Commellas G, Lemkau LR, Nieuwkoop AJ, Kloepper KD, Ladror DT, Ebisu R, Woods WS, Lipton AS, George JM, Rienstra CM. (2011) J. Mol. Biol. 411:881-95
27. Lemkau LR, Comellas G, Kloepper KD, Woods WS, George JM, Rienstra CM. (2012) J. Biol. Chem. In press doi:10.1074/jbc.M111.306902
28. Yang L, van der Werf KO, Koopman BFJM, Subramaniam V, Bennink ML, Dijkstra PJ, Feijen J. (2007) J. Biomed. Mater. Res. 82:160-168
29. Kjelstrup-Hansen J, Hansen O, Rubahn HG, Bøggild O. (2006) small 5:660-666
30. Isono Y, Namazu T, Taneka T. (2001) Proc. MEMS IEEE 135-138
31. Knowles TP, Fitzpatrick AW, Meehan S, Mott HR, Vendruscolo M, Dobson CM, Welland ME. (2007) Science 318:1900-1903

32. Mücke N, Kreplak L, Kirmse R, Herrmann H, Aebi U, Langowski J. (2004) J. mol. Biol. 335:1241-1250
33. Mickey B, Howard J. (1995) J. Cell Biol. 130:909-917
34. Whang JC, Turner MS, Agarwal G, Kwong S, Josephs R, Ferrone FA, Briehl RW. (2002) J. Mol. Biol. 315:601-612
35. Knowles TPJ, Smith JF, Craig A, Dobson CM, Welland ME. (2006) Phys. Rev. Lett. 96:238301-1-4
36. Smith JF, Knowles TPJ, Dobson CM, MacPhee CM, Welland ME. (2006) Proc. Natl. Acad. Sci 103:15806-15811
37. Rivetti C, Guthold M, Bustamante C. (1996) J. Mol. Biol. 264:919-932
38. Van Buren V, Cassimeris L, Odde DJ. (2005) Biophys. J. 89:2911-2926
39. Moreno-Herrero F, Perez M, Baro AM, Avila J. (2004) Biophys. J. 86:517-525
40. Liu Z, Li Z, Zhou H, Wei G, Song Y, Wang L. (2005) Microsc. Res. Techniq. 66:179-185
41. Adamcik J, Mezzenga R. (2011) Soft Matter 7:5437-5443
42. Gosline JM, Guerette PA, Ortlepp CS, Savage KN. (1999) J. Exp. Biol. 3303:3295-3303
43. Vollrath F, Knight DP. (2001) Nature 410:541–548
44. Gere JM, Timoshenko SP. (1999) Mechanics of Materials. Fourth SI edition, Stanley Thornes (Publishers) Ltd, Cheltenham
45. Nelson R, Sawaya, MR, Balbirnie M, Madsen AO, Riekel C, Grothe R, Eisenberg D. (2005) Nature 435:773-778
46. Eisenberg D, Nelson R, Sawaya MR, Balbirnie M, Sambashivan MR, Ivanova MI, Madsen Aø., Riekel C. (2006) Acc. Chem. Res. 39:568–575
47. Meersman F, Cabrera RQ, McMillian PF, Dmitriev V. (2011) Biophys. J. 100:193-197
48. Török M, Milton S, Kayed R, Wu P, McIntire T, Glabe CG, Langen R. (2002) J. Biol. Chem. 277:40810-15
49. Chen M, Margittai M, Chen J, Langen R. (2007) J. Biol. Chem. 282:24970-79
50. Shabestari MH, Segers-Nolten IMJ, Claessens MMAE, van Rooijen BD, Subramaniam V, Huber M. (2012) Abstracts of the Biophysical Society Annual Meeting, in press.
51. Esposito A, Dohm CP, Kermer P, Bahr M, Wouters FS. (2007) Neurobiol. Dis. 26:521-531
52. Alim MA, Ma Q, Takeda K, Aizawa T, Matsubara M, Nakamura M, Asada A, Saito T, Kaji H, Yoshii M, Hisanaga S, Ueda K. (2004) J. Alzheimers Dis. 6:435-422
53. Wersinger C, Sidhu A. (2007) Biochemistry 44:3612-13624
54. Kojima H, Ishijima A, Yanagida T. (1994) Proc. Natl. Acad. Sci. 91:12962-12966
55. Claessens MMAE, Bathe M, Frey E, Bausch AR. (2006) Nature Materials 5:748-753
56. Schaap IAT, Carrasco C, Pablo PJ. de, Mackintosh FC, Schmidt CF. (2006) Biophys. J. 91:1521-1531
57. Fudge DS, Gardner KH, Forsyth VT, Riekel C, Gosline JM. (2003) Biophys. J. 85:2015-2027

PART III

FIBRIL MECHANICS

CHAPTER 7

Nanomechanical properties of α-synuclein amyloid fibrils: a comparative study by nanoindentation, harmonic force microscopy, and Peakforce QNM

We report on the use of three different atomic force spectroscopy modalities to determine the nanomechanical properties of amyloid fibrils of the human α-synuclein protein. α-Synuclein forms fibrillar nanostructures of approximately 10 nm diameter and lengths ranging from 100 nm to several microns, which have been associated with Parkinson's disease. Atomic force microscopy (AFM) has been used to image the morphology of these protein fibrils deposited on a flat surface. For nanomechanical measurements, we used single-point nanoindentation, in which the AFM tip as the indenter is moved vertically to the fibril surface and back while the force is being recorded. We also used two recently developed AFM surface property mapping techniques: Harmonic force microscopy (HarmoniX) and Peakforce QNM. These modalities allow extraction of mechanical parameters of the surface with a lateral resolution and speed comparable to tapping-mode AFM imaging. Based on this phenomenological study, the elastic moduli of the α-synuclein fibrils determined using these three different modalities are within the range 1.3-2.1 GPa. We discuss the relative merits of these three methods for the determination of the elastic properties of protein fibrils, particularly considering the differences and difficulties of each method.

Sweers KKM, van der Werf KO, Bennink ML, Subramaniam V. (2011) Nanoscale Research Letters 6:270

INTRODUCTION

Amyloid fibrils are insoluble protein aggregates that have been associated with a range of neurodegenerative diseases, including Huntington, Alzheimer's, Parkinson's, and Creutzfeldt-Jakob disease [1]. The fibrils typically have a diameter ranging from 4 to 12 nm, and lengths from 100 nm up to several microns [2,3,4]. In this study, we investigated the nanomechanical properties of amyloid fibrils formed from the human α-synuclein protein, which is associated with Parkinson's disease. α-Synuclein amyloid fibrils are found in the brains of Parkinson's disease patients as components of larger plaques called Lewy bodies [5,6].

Atomic force microscopy (AFM) has been primarily used as an imaging tool to determine morphological parameters such as height and length of amyloid fibrils, such as those formed from α-synuclein [2,3,4], insulin [7], and β-lactoglobulin [8]. AFM is also a powerful technique for characterizing mechanical properties. With the ability to exert and measure forces up to the piconewton range, AFM is a particularly suitable tool to determine the nanomechanical properties of nanometer-sized biological structures, such as amyloid fibrils. Mechanical properties such as stiffness, rigidity, resistance to breakage or adhesive properties of these fibrils or individual monomers are interesting for the use of these fibrils as nanomaterials, for getting a better understanding of the physico-chemical properties of these fibrils, and to get more insight into their structure and growth [9-14].

Indentation-type AFM or single-point nanoindentation (SPI), for example, implemented as 'Point-and-Shoot' in the Veeco operating software, is the most widely used method to measure nanomechanical properties of a sample. In this mode, the tip approaches and indents the sample until a certain predefined force is reached. At this point the tip is retracted again. During this approach and retract cycle the force is continuously measured, resulting in a force versus distance graph. AFM nanoindentation has been performed on different biological substrates such as collagen [15], insulin fibrils, and crystals [16], but also on different polymeric materials, such as fibrils used for biodegradable scaffolds [17]. The approach-retract cycle is typically performed at a rate of 0.5 to 10 Hz, which makes this method inherently slow. To get an overview of the mechanical properties of a sample, nanoindentation can be used in a force-volume mode. Here, for every pixel in an image a complete force curve is recorded, which results in data acquisition times of up to hours for a single image.

Recently, several different surface property mapping techniques have become available that work at much higher speeds, leading to significantly increased data throughput [18-20]. Two commercially available approaches are PeakForce QNM and Harmonic

force microscopy or HarmoniX (Veeco, Santa Barbara, CA, USA). PeakForce QNM is based on the force-volume approach; however, the speed of taking the force curves is significantly increased (either at 1 or 2 kHz). In this mode the maximum force exerted on the sample is maintained constant, which is beneficial for soft delicate biological samples. Because of the recent introduction of the Peakforce QNM method, only a few studies have been reported, such as the stiffness mapping of polymer blends [18].

HarmoniX is another surface property mapping technique based on the nonlinear dynamic behavior of a cantilever in tapping mode due to repulsive and attractive forces caused by the specific material characteristics of the sample acting on the tip [21,22]. Because of the low bandwidth of the cantilever response, this information ends up in the phase image as obtained during tapping mode imaging. This phase signal is related to energy dissipation, which is determined by the viscoelastic and adhesive properties of the sample [21,23]. However, because of the convolution of multiple physical properties into one signal, interpretation of these images is not straightforward. The higher harmonic vibrations of the cantilever excited by these material properties can provide more information, but they are heavily suppressed and are difficult to measure. [21,24]. In HarmoniX, a torsional cantilever with the tip positioned off-axis solves this problem and acts as a high bandwidth force sensor [24]. HarmoniX has been applied to both polymers and biological features, for example, DNA [25,26].

We used these three different methods, SPI, PeakForce QNM, and HarmoniX, to determine the modulus of elasticity of protein nanofibrils, generated from the E46K mutant of the human α-synuclein protein. The resulting values for the elastic modulus are in the range between 1.3 and 2.1 GPa. We discuss the relative merits of the application of these three methods specifically for the determination of the elastic properties of protein fibrils in more detail, with particular emphasis on the differences and difficulties of each method.

METHODS

SAMPLE PREPARATION

E46K disease mutant α-synuclein was recombinantly expressed and purified as previously described [4]. A 100 μM monomeric E46K solution in 10 mM Tris-HCl, 50 mM NaCl, pH 7.4 was incubated at 70°C in Eppendorf tubes under constant shaking. After 27 h, well-defined protein fibrils were formed in solution, which was verified by a Thioflavin T fluorescence assay specific for cross-beta structures characteristic of amyloid fibrils.

Samples for AFM imaging in liquid were prepared by placing 50 µl of a 5x diluted solution containing fibrils on the mica substrate. This solution was allowed to adsorb for 10 min and then washed gently with 200 µl buffer. For imaging, 80 µl of fresh buffer solution was placed on the sample. We used the same buffer solution (10 mM Tris-HCl, 50 mM NaCl, pH 7.4) for both dilution and imaging. For the measurements performed in ambient air, a 10x diluted protein solution was placed on mica substrates and allowed to adsorb in the same manner as described above. Subsequently, the sample was washed with 200 µl milliQ water and dried with a gentle nitrogen stream.

AFM CANTILEVER AND TIP CHARACTERIZATION

The tip radius was determined with two different methods. First, from the AFM height images of protein fibrils the tip radius was derived from the fibril height-to-width ratio based on tip-sample convolution [21,31]. Only fibrils that were perpendicular to the scan axis were used. From the tip sample convolution method an average tip radius of 100 nm was determined. Second, the tip was imaged by scanning electron microscopy (Philips XL30 ESEM-FEG). With the SEM, the average tip radius was found to be approximately 80 nm. For both methods, the tip resulted in a considerably larger number than the nominal tip radius provided by the manufacturer. An average value of 90 nm was used in the analysis with an error of 30%.

The cantilever spring constants were determined with the thermal noise method implemented in the Veeco software and were assumed to have a 5% error [33].

SINGLE-POINT NANOINDENTATION

A Bioscope II microscope (Veeco, Santa Barbara, CA, USA) was used for the SPI experiments. In order to measure the fibril heights, AFM tapping mode images were recorded in a physiological buffer (10 mM Tris-HCl, 50 mM NaCl, pH 7.4) in tapping mode with low force settings (reduced to 3 nm, 80-90% of the free amplitude) to minimize interaction with the sample. We use silicon nitride probes (MSCT, tip F, 0.5 N/m, Veeco, Santa Barbara, CA, USA) for these measurements. The average fibril height measured in tapping mode is used to determine the surface contact area for all three indentation methods. The indentation measurements were performed with the "Point and Shoot" application in the NanoScope 7.30 (Build R2Sr1.) software. To locate the indentation locations we first imaged the fibrils in contact mode using another probe (MSCT, tip E, 0.1 N/m, Veeco, Santa Barbara, CA, USA). This probe was selected to, on one hand, minimize the forces during contact mode imaging and, on the other hand, to match the spring constant of the cantilever to the stiffness of the sample for the indentation measurements. Every fibril was indented approximately 8 times at different

positions along its length. Prior to fibril indentation, force curves were recorded on the mica substrate close to the fibril to determine deflection sensitivities of the cantilevers.

DATA ANALYSIS

The raw deflection curves, obtained in the SPI mode, were converted to a force separation curve using the deflection sensitivities and the spring constants of the cantilevers in a custom written Matlab program. To extract the elastic modulus from the force separation curve, the Hertz model was used to analyze the force curve [39]. This model, in the case of a spherical indenter on a cylinder shaped object, is given in Figure 1, where F is the load, v the Poisson ratio, δ the separation, and E the modulus of elasticity. The equivalent contact radius R_{eq} for a spherical indenter with radius R_t, with an infinitely long cylinder with radius R_f is given by the expression in Figure 1. The modulus of elasticity was determined from the slope of the curve where $F^{2/3}$ was plotted versus the separation. Small segments along this curve were fitted to a linear equation and the r^2 value was determined for every fit, yielding an elastic modulus as a function of separation. From the point the force increases, the r^2 value increases and only fits with an r^2 above 0.95 were used in the analysis. From the point of contact the modulus of elasticity values for the following 2 nm were averaged (20% indentation [12]).

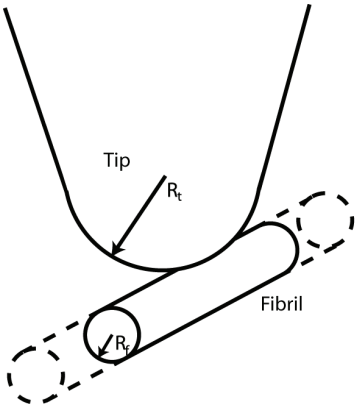

$$F = \frac{16E\sqrt{R_{eq}}}{9(1-\nu^2)} \cdot \delta^{\frac{3}{2}}$$

$$R_{eq} = \sqrt{\frac{(R_t{}^2 R_f)}{(R_t + R_f)}}$$

FIGURE 1; Schematic representation of equivalent contact radius. Schematic representation of the AFM tip as a spherical indenter and the protein fibril as an infinitely long cylinder.

Due to the finite thickness effects, the obtained modulus of elasticity is influenced by the stiff underlying substrate (mica). A correction factor for this effect was applied which was a function of the maximum applied force and the value of the uncorrected modulus of elasticity [16,36].

All analysis steps were implemented in a custom Matlab program. The algorithm analyzes both the force curve and the r2 curve to accurately determine the point-of-contact,

that is, the separation at which the tip starts indenting the fibril. This point is defined as the point where the force distance curve leaves the baseline, and r^2 adopts a value higher than 0.95.

HARMONIC FORCE MICROSCOPY

HarmoniX was performed under ambient conditions (that is, at room temperature without further control of humidity) on a Veeco Multimode microscope with a Nanoscope V controller (Veeco, Santa Barbara, CA, USA). The analysis software uses the DMT model [40]. Torsional cantilevers (TL01, MikroMasch, Tallinn, Estonia) with a nominal spring constant of 2 N/m were used. The measured vertical and torsional resonance frequencies were 111 kHz and 1.1 MHz, respectively. The system was calibrated with a reference sample (model PS-LDPE, Veeco, Santa Barbara, CA, USA) [20]. Since HarmoniX assumes a spherical tip that indents an infinitely large and thick flat elastic surface, the value for the modulus of elasticity needs to be corrected offline. The first correction factor applied is to account for the different geometry, which in these experiments is a spherical tip indenting an infinitely long cylinder, see Figure 1. The correction factor used here is 2.1. The second correction factor was applied to account for the finite sample thickness of the protein fibril. A correction factor of 1.3, determined by the SPI measurements, was used.

PEAKFORCE QNM

Peakforce measurements were done on a Veeco Bioscope Catalyst microscope with a Nanoscope V controller (Veeco, Santa Barbara, CA, USA). The analysis software uses the DMT model [40]. The measurements were done both in ambient conditions (uncontrolled humidity, temperature, and air pressure) and physiological buffer (10 mM Tris-HCl, 50 mM NaCl, pH 7.4). The manufacturer provides a list of optimal cantilevers to measure specific ranges of elastic moduli. For the ambient measurements the stiff RTESP cantilevers (26.9 N/m, Veeco, Santa Barbara, CA, USA) were used, due to the high adhesion forces observed for other, less stiff cantilevers. For the measurements performed in buffer we used a medium stiff cantilever: FMR-10 cantilevers (nominal spring constant 2.8 N/m, Nanoworld, Neuchâtel, Switzerland). Here, the elastic moduli are also corrected offline as described for the HarmoniX data (see Harmonic force microscopy).

IMAGE ANALYSIS

Using SPIP software (Image Metrology A/S, Lyngby, Denmark), a trace was drawn on top of the fibril to determine the average height from the height images or modulus of elasticity from the stiffness maps of the individual fibrils, according to the procedure

described in [4]. A point of potential confusion is that both HarmoniX and Peakforce QNM create so-called 'stiffness' maps, which in the software is expressed in units of Pa. Technically this is not correct, since stiffness is expressed in units of N/m. The parameter in these images is a modulus of elasticity which is expressed in Pa. In this manuscript we therefore refer to these values as moduli of elasticity. All images in this article are linewise corrected. Actual measurements are done on uncorrected images.

RESULTS

SINGLE-POINT NANOINDENTATION EXPERIMENTS IN LIQUID

α-Synuclein fibrils deposited on mica were scanned both in tapping mode and contact mode, respectively, for determining the height and finding the indentation points for the SPI measurements. We determined an average fibril height of 9.0 ± 0.4 nm (N=60) from the tapping mode images. This average height value was used to determine the effective contact surface in the indentation measurements according to the model shown in Figure 1. The fibril heights measured in contact mode imaging were considerably lower and were therefore not used in determining the average fibril height. This was attributed to the pressure from the tip on the sample. The force exerted on fibrils with the 0.1 N/m cantilever during scanning was between 0.5 and 1 nN.

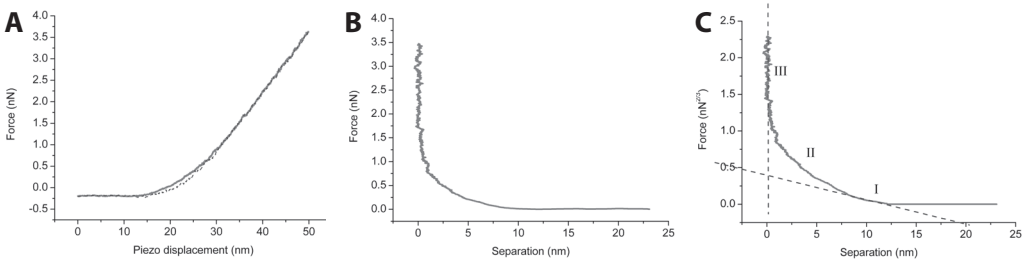

FIGURE 2; Typical force curves. (A) A typical force versus piezo displacement curve obtained from the measurement, with the approach curve (solid red) and the retract curve (dashed blue). (B) Force versus separation approach curve calculated from the force versus piezo displacement curve. (C) Force to the power of 2/3 versus separation approach curve, showing distinct transition from the tip only sensing the fibril (part I) to the part where the tip is sensing the mica under the fibril (part II) until the part where the tip is only pressing on the mica (part III). From the slope of part I, a modulus of elasticity of 1.2 GPa was calculated for the force curve presented here.

We performed nanoindentation experiments on five fibrils, each of which was indented 8 times at different locations along its length. A typical force distance curve resulting from this procedure is shown in Figure 2A. The absence of adhesion during

the measurements allowed the use of the Hertz model.

Although every fibril was indented 8 times, not all curves were suitable for analysis. For some curves, the r^2 values of the linear fit did not exceed 0.95 in the part where the tip was indenting the fibril (part 1 in Figure 2C). From the curves that were analyzed, an average elastic modulus of 1.3 ± 0.4 GPa (N = 31) was found for α-synuclein fibrils.

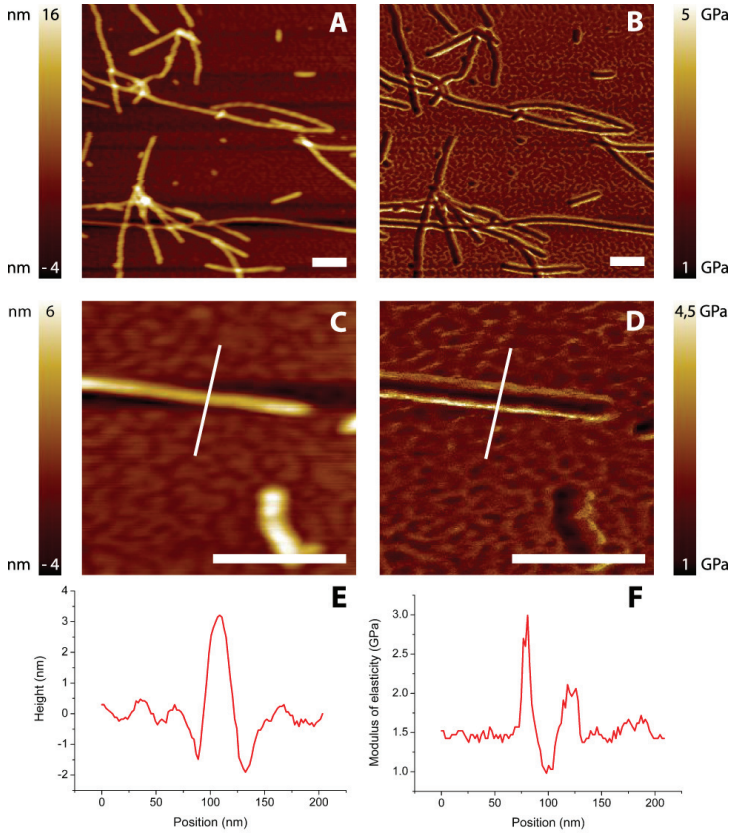

FIGURE 3; Harmonic force microscopy images. Height (A, C) and corresponding elas-ticity images (B, D) of α-synuclein fibrils on mica. E represents the cross-sections drawn over the fibril in C. F represents the cross-section from D and shows a few scan artifacts. The background, mica, has here a stiffness of ±1.5 GPa, probably caused by the limited range of elastic moduli which can be measured with the chosen cantilever. The peaks shown around 80 and 120 nm are edge effects caused by changing contact areas. The dip around 100 nm is assumed to be relevant for averaging and used to determine a modulus of elasticity. Scale bars are 250 nm.

HARMONIC FORCE MICROSCOPY

A sample of α-synuclein fibrils deposited on mica was scanned. Figure 3 shows two typical images recorded, with corresponding height and elasticity profiles. The fibrils

show considerably lower modulus of elasticity compared to the background. However, the edges of the fibril show increased modulus of elasticity values, also displayed in the cross-section of the fibril shown in Figure 3F. We attribute this effect is due to the changing contact area compared to the contact area shown in Figure 1 where the tip is indenting the middle of the fibril. This artifact is also visible in the height images derived from the harmonic force mode, shown in Figure 3E, and they are therefore not used in further analysis. For each individual fibril, the values for the elastic modulus measured along the fibril were averaged. The average value was 1.2 ± 0.2 GPa (N = 95).

PEAKFORCE QNM

The surface property mapping technique Peakforce QNM is able to image the sample both in ambient conditions and in buffer solution. Figure 4 shows height images and the corresponding elasticity maps obtained with Peakforce QNM of α-synuclein fibrils, obtained in buffer (Figure 4A,B) and in air (Figure 4C,D). These images were obtained with a high setpoint of around 15 nN and show that for both liquid and ambient conditions the height and elasticity ranges which can be obtained with Peakforce QNM are similar. However, this large setpoint causes the fibrils to break, especially in liquid, see Figure 4A.

To prevent damage to the α-synuclein fibrils, a lower setpoint of 1-2 nN was used. This resulted in intact fibrils with significant lower values of the elastic moduli (Figure 5). The elastic modulus for each fibril is determined from the average value of the DMT modulus obtained along the fibril length. This resulted in a modulus of elasticity of 1.3 ± 0.3 GPa (N = 57) for the fibrils in ambient conditions and 1.0 ± 0.2 GPa (N = 59) for those in liquid.

DISCUSSION

CHOOSING THE RIGHT CANTILEVER

In order to measure the elastic properties of a material, the choice of the cantilever is key. In nanoindentation the highest sensitivity (and thus accuracy) is achieved if the spring constant of the probe cantilever is identical to the effective spring constant of the sample (also referred to as contact stiffness), see Figure 6. If the spring constant of the cantilever is more than 10 times lower or higher than that of the sample, the sensitivity is about 3 times lower, see Figure 6, making the determination of the elastic modulus less accurate. Practically since one does not know the stiffness of the sample a priori, an estimation is necessary. This is also the case for the surface mapping methods. The nominal elastic modulus ranges accessible by HarmoniX and Peakforce QNM are

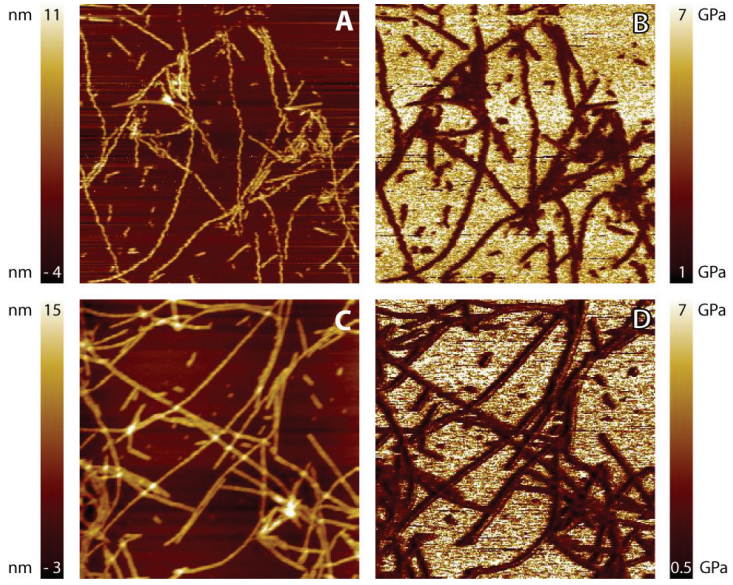

FIGURE 4; Peakforce QNM images in liquid and ambient conditions. Height (A, C) and corresponding elasticity maps (B, D) recorded with Peakforce QNM. Panels A and B are recorded in liquid (setpoint is 14 nN) and C and D in ambient conditions (setpoint is 16 nN). The fibrils have in these images an average modulus of elasticity of 3 GPa and mica between 6 and 7 GPa. Image size is 2x2 μm.

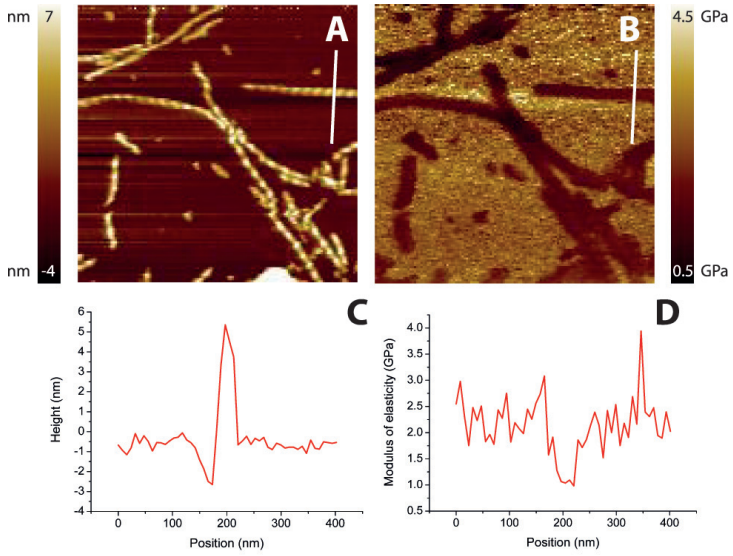

FIGURE 5; Peakforce QNM images. Height and stiffness map of fibrils obtained with a setpoint of 1 nN in liquid, images size is 1μm (A, B). C and D represent the cross-section of the fibril. Notice that in Peakforce QNM the artifacts at the edges of the fibrils seen in HarmoniX (Figure 3F) caused by changing contact areas are absent.

10 MPa-10 GPa and 0.7 MPa-70 GPa, respectively [18]. However, as noted above, this range depends on the cantilever that is used for the measurements and is in practice significantly smaller.

A second point to consider when choosing the cantilever is the adhesion between the tip and the sample. The spring constant of the cantilever should be sufficiently high to create enough force to come loose from the surface. In the PeakForce QNM experiments reported here on protein fibrils, performed in ambient air, an adhesion of few nanonewtons was observed. For reproducible and proper deflection curves in air we used in this case a cantilever with a spring constant of approximately 27 N/m. In the HarmoniX mode the fibrils are measured in a special tapping mode. In this mode reproducible results were obtained with cantilevers with medium stiffness of 2 N/m in ambient conditions. The cantilever used for the nanoindentation measurements (0.1 N/m) showed an incredibly large artifact in both approach and retract curves at the 1 kHz ramp rate in Peakforce QNM in liquid, which was not seen in the nanoindentation measurements. This artifact could be induced by the impact of the effective mass and damping forces at the working frequency of 1 kHz. These hydrodynamic forces acting on the cantilever are frequency-dependent [27, 28]. Although we do not know how the Peakforce QNM software compensates for this, it is possible these effects in liquid could interfere with the measurements. Scanning with stiffer cantilevers with nominal spring constant 2.8 N/m yielded reproducible results.

Finally, in addition to choosing the optimal cantilever stiffness, it is also important to ensure that the resonance frequency for Peakforce QNM imaging is above 10 kHz, in order not to interfere with the 1 kHz ramping.

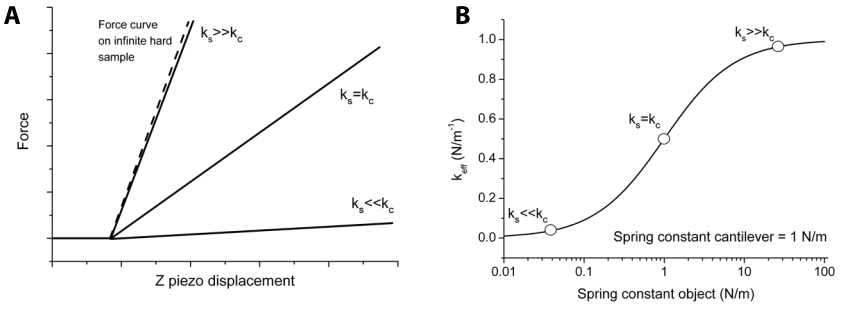

FIGURE 6; Effective spring constant as a function of sample stiffness. (A) Force versus z piezo displacement curve in case of sample spring constant larger, the same or lower compared to the spring constant of the cantilever. (B) Effective spring constant (keff, representing the slope of the force curves in A) as a function of the stiffness of the sample. From the slope of this curve it is clear that the maximum sensitivity is achieved when both spring constants are of the same order of magnitude.

CALIBRATION

The calibration of all three methods is difficult and consists of several steps. For all methods one needs the deflection sensitivity, the spring constant of the cantilever and the tip radius. For the SPI experiments the tip radius can be determined afterwards. Both surface mapping methods need the tip radius as an input parameter before measuring. For HarmoniX, in addition to this tip radius, some additional parameters, such as the torsional frequency, are needed. An alternative way of calibration of the surface mapping methods was done with the reference sample (see "Methods" section). In this study, this reference sample is only used in the HarmoniX measurements.

ANALYSIS OF RESULTS

ERROR ANALYSIS

All three techniques use a contact mechanics model which is based on assumptions and parameters which can only be determined with a limited accuracy. The first assumption starts with the Poisson ratio for these protein fibrils. For small biological samples this ratio between lateral strain and axial strain is not known. The theoretical upper limit is 0.5 and concrete as a material has a value between 0.1 and 0.2. In this study we used 0.3, because we assumed the fibrils to be in the same range as polymers [29]. This Poisson ratio has only a small influence on the actual modulus of elasticity values (Poisson ratio change from 0.3 to 0.4 gives a 5% change in modulus of elasticity).

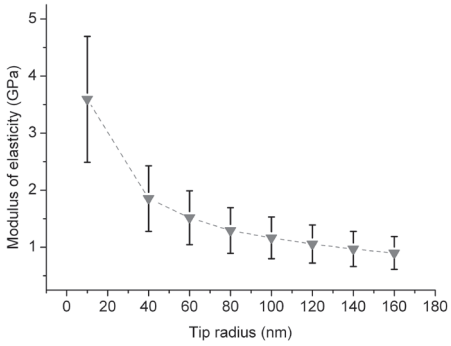

FIGURE 7; Dependence of modulus of elasticity in tip radius. The force curve data obtained with SPI measurements are used to calculate the modulus of elasticity with variable tip radii while all other parameters are kept constant.

The tip radius has, compared to the Poisson ratio and fibril radius, a large impact on the results. It is therefore important to measure the tip radius after the experiments. The tip radius is in our experience in practice always larger than the manufacturer

specification, both before and after the experiment. Figure 7 shows the impact of the tip radius on the results of the SPI measurements on the α-synuclein fibrils when all the other parameters are kept constant. The dependence is less significant at larger tip radii.

However, even when using blunt tips there are measurement errors which have to be considered. The radius of the tip in indentation studies is often determined by scanning electron microscopy [16] after the indentation experiments where the tip shape could be influenced by wear [30]. Another method is to determine the tip radius from tip sample convolution models [21,31]. From previous studies the error from the tip sample convolution method is around 30% [32].

An additional important step is the calibration of the cantilever spring constant. There are a number of techniques available to determine the spring constant, each with their own uncertainties [33-35]. In this study, cantilevers were calibrated with the thermal noise method, which has an associated average error of 5% [33].

All three methods described here are susceptible to relatively large systematic errors arising from the compounding of errors inherent to the different calibration and characterization techniques. Using the law of propagation of errors, we estimate that this systematic error combined with the above-mentioned and the previously described 2% error in the deflection sensitivity measurements [34] yields an uncertainty of approximately 39% of the average measured value. In addition to these errors, experimental data are also influenced by the expected statistical variation due to heterogeneity of a large sample set.

FINITE SAMPLE THICKNESS

When indenting small fibrillar features with a relatively large tip radius one has to take the finite sample thickness effects into account. As shown in Figure 2C the force curve displays distinct regimes: from being free in air above the sample to the initial fibril indenting section where the tip 'only' feels the fibril (Figure 2C, part I), to where the mica underneath starts to play a role (Figure 2C, part II), and finally to the last section where only the hard surface is felt by the tip (Figure 2C, part III). The initial 20% of the total height of a feature is thought to be unaffected by these final sample thickness effects for large objects relative to the tip radius [12]. However, at the typical size scales of these nanofibrils, a correction for these effects is necessary [16,36]. In the Peakforce QNM software these effects are not considered and therefore not compensated for [18]. In HarmoniX there is also no correction for these effects. However, the question is whether these effects are nearly as pronounced in HarmoniX because of the small indentations that are made with this technique. In the SPI measurements from this study the correction factor was small (~1.3) because of the rather high modulus of elasticity.

DISCUSSION OF RESULTS

All methods used in this study yielded moduli of elasticity between 1.3 and 2.1 GPa (see Table 1), which is close to values found for collagen and other amyloid fibrils [10,15]. These values are somewhat smaller than those obtained for films made with fibrillar networks of β-lactoglobulin (5.2-6.2 GPa) and lysozyme (6.7-7.2 GPa) [37], and potentially reflect the differences in experimental conditions. We also measured insulin and lysozyme amyloid fibrils using HarmoniX under ambient conditions. The values measured, 1.4 ± 0.2 GPa for lysozyme fibrils and 1.4 ± 0.1 GPa for insulin, were commensurate to that measured for α-synuclein. The modulus previously found for insulin fibrils measured with SPI in liquid, which is at a lower working speed, is three orders of magnitude lower [16]. However, Smith et al. [11] have found a value of 3.3 GPa for insulin fibril using force spectroscopy on suspended fibrils. Note that in this work all the methods result in relatively similar values, although they all have very different operation speeds.

Method	*Environment*	*Operation frequency (Hz)*	*Uncorrected modulus of elasticity (GPa)*	*Modulus of elasticity (GPa)*
Nanoindentation	Liquid	1	–	1.3 ± 0.4
Peakforce QNM	Liquid	10^3	1.0 ± 0.2	1.6 ± 0.3
Peakforce QNM	Air	10^3	1.3 ± 0.3	2.1 ± 0.5
HarmoniX	Air	10^5	1.2 ± 0.2	1.9 ± 0.3

TABLE 1; Overview of results from different methods under different environmental conditions, 4th column represents the corrected values for modulus of elasticity. This correction is the same as done in the analysis of the indentation measurements; the contact area is changed to a spherical indenter on an infinite cylinder (average fibril height of 9.0 ± 0.4 nm, measured in AFM tapping mode) and is corrected for the finite sample thickness as described in the "Methods" section.

The spread in the SPI measurements is also comparable to earlier work. The reason for this spread, besides the previously mentioned errors, has been related to heterogeneity in the internal packing of amyloids [1,16,38].

Both surface contact area and finite sample thickness corrections were performed offline on the HarmoniX and Peakforce QNM data, see Table 1, which results in higher values. The finite sample correction value found in the analysis of the SPI of 1.3 and the relation for a spherical indenter on an infinite long cylinder are used. The high modulus of elasticity of the fibrils suggests a high packing density. The difference between liquid and ambient air conditions becomes more significant after correction. With the

uncorrected values the difference is lower, which suggests little room for water within the fibril, but the corrected results could point to an observed drying effect.

However, the large spread, seen in Table 1 and in previous studies, combined with the large systematic error of 39% calculated above makes interpreting these results very difficult.

CONCLUSIONS

The nanometer scale diameters of α-synuclein protein fibrils pose some serious challenges for interpretation of the data obtained with SPI, HarmoniX and Peakforce QNM. The typical size scales of the fibrils give rise to finite sample thickness effects [16,36]. Furthermore, these fibrils cannot be described as a flat film on a surface for which all the standard models are valid [39,40]. Finally, these samples have strong adhesive properties which results in choosing cantilevers that possibly result in less contrast between the fibrils and the surface, because of the mismatch between cantilever and sample stiffness. All these difficulties are addressable with the conventional nanoindentation measurements, where the analysis is mostly done offline and in custom-written algorithms. For the surface property mapping techniques it is at this point only possible to customize the analysis in a limited manner. The methods come with specific conditions in which the analysis is valid. First, the tip should be a hard sphere compared to the sample. Second, only elastic deformation is taken into account. Last, the sample should not be confined vertically (finite sample thickness effect) or laterally (by surrounding material) [18]. For protein fibrils the second condition is not actually known, after indentation with high forces (>3 nN) the fibrils appear to be broken, while with lower forces they stay intact (<2 nN). The third condition is not met in case of the protein fibrils. For HarmoniX it is also good to keep in mind that theoretically one needs an infinite number of frequency components to reconstruct the real time interaction between the tip and the surface [18].

To obtain in a short amount of time quantitative modulus of elasticity for protein fibrils the surface property methods are relatively easy to use and fast. However, recording individual curves on the fibrils during scanning is necessary to analyze the curves for all the conditions that are not met in these methods. In case of the measurements done on the protein fibrils the differences are within each others error ranges. This may not be the case for other biological structures. It is essential to understand the limitations of each method and carefully analyze the data, including the individual force curves, according to the valid conditions for the specific structures.

ACKNOWLEDGMENTS

The authors thank Kirsten van Leijenhorst-Groener for protein expression and purification and Sissi de Beer for advice on HarmoniX.

REFERENCES

1. Dobson CM. (2003) Nature 426:884-890
2. Hoyer W, Antony T, Cherny D, Heim G, Jovin TM, Subramaniam V. (2002) J. Mol. Biol. 322:383-393
3. Segers-Nolten I, Van der Werf K, Van Raaij M, Subramaniam V. (2007) In proceedings of the IEEE Conf Eng Med Biol Soc pp 6609-6612
4. van Raaij ME, Segers-Nolten IMJ, Subramaniam V. (2006) Biophys. J.: Biophys. Lett. 91:L96-L98.
5. Schultz W. (2006) Proc. Natl. Acad.Sci. 103:166-168
6. Goedert M. (2001) Nat. Rev. Neurosci. 2:492-501
7. Jansen R, Dzwolak W, Winter R. (2005) Biophys. J. 88:1344-53
8. Adamcik J, Jung JM, Flakowski J, Rios De Los P, Dietler G, Mezzenger R. (2010) Nanotechnol. 5:423-28
9. Cherny I, Gazit E. (2008) Angew. Chem. Int. Ed. 47:4062-69
10. Knowles TP, Fitzpatrick AW, Meehan S, Mott HR, Vendruscolo M, Dobson CM, Welland ME. (2007) Science 318:1900-03
11. Smith JF, Knowles TPJ, Dobson CM, MacPhee CM, Welland ME. (2006) Proc. Natl. Acad. Sci. 103:15806-11
12. Sullan RMA, Gunari N, Tanur AE, Chan Y, Dickinson GH, Orihuela B, Rittschof D, Walker GC. (2008) Biofouling 25:263-275
13. Yu J, Malkova S, Lyubchenko YL (2008) J. Mol. Biol. 384:992-1001
14. Dong M, Hovgaard MB, Mamdouh W, Xu S, Otzen DE, Besenbacher F. (2008) Nanotechnology 19:384013
15. Heim AJ, Matthews WG. (2006) Appl. Phys. Lett. 89:181902
16. Guo S, Akhremitchev BB. (2006) Biomacromolecules 7:1630-36
17. Tan EPS, Lim CT. (2005) Appl. Phys. Lett. 87:123106
18. Pittenger B, Erina N, Su C. Application Note Veeco Instruments Inc. [http://www.bruker-axs.com/uploads/tx_linkselectorforpdfpool/Quantitative_Mechanical_Property_Mapping_at_the_Nanoscale_with_PeakForce-QNM_AFM_AN128.pdf]
19. Rosa-Zeiser A, Weilandt E, Hild S, Marti O. (1997) Meas. Sci. Technol. 8:1333-38
20. Sahin O. (2007) Rev. Sci. Instrum. 78:103707
21. Garcia VJ, Martinez L, Briceno-Valero JM, Schilling CH. (1997) Probe Microsc. 1:107-16

22. Burnham NA, Behrend OP, Oulevey F, Germaud G, Gallo P-J, Gourdon D, Dupas E, Kulik AJ, Pollok HM, Briggs GAD. (1997) Nanotechnology 8:67-75
23. Cleveland JP, Anczykowski B, Schmid AE, Elings VB. (1998) Appl. Phys. Lett. 72:2613-15
24. Sahin O, Magonov S, Su C, Quate C F, Solgaard O. (2007) Nat. Nanotechnol. 2:507-14
25. Sahin O, Erina N. (2008) Nanotechnology 19:445717
26. Dong M, Husale S, Sahin O. (2009) Nat. Nanotechnol. 4:514-17
27. Tamayo J, Calleja M, Ramos D, Mertens J. (2007) Phys. Rev. B. 76:180201
28. Pirzer T, Hugel T. (2009) Rev. Sci. Instrum. 80:035110
29. Grellman W, Seidler S. (2001) Deformation and Fracture Behavior of Polymers: First edition. Berlin: Springer-Verlag
30. Wang Y, Chen X. (2007) Ultramicroscopy 107:293-98
31. Zenhausern F, Adrian M, Heggeler-Bordied BT, Eng LM, Descouts P. (1992) Scanning 14:212-17
32. VanLandingham MR, Juliano TF, Hagon MJ. (2005) Meas. Sci. Technol. 16:2173-85
33. Ohler B. (2007) Rev. Sci. Instrum. 78:063107
34. Cook SM, Schäffer TE, Chynoweth KM, Wigton M, Simmonds RW, Lang KM. (2006) Nanotechnology 17:2135-45
35. Gibson CT, Smith DA, Roberts CJ. (2005) Nanotechnology 16:234-38
36. Akhremitchev BB, Walker GC. (1999) Langmuir 15:5630-34
37. Knowles TPJ, Oppenheim TW, Buell AK, Chirgadze DY, Welland ME. (2010) Nat. Nanotechnol. 5:204-207
38. Paparcone R, Keten S, Buehler M. (2009) J. Biomech. 43:1196-01.
39. Hertz H. (1882) J. Rein. Angew. Math 94:156-71
40. Derjaguin BV, Muller VM, Toporov YUP. (1975) J Colloid Interf. Sci 53:314-26

CHAPTER 8

Spatially resolved frequency-dependent elasticity measured with pulsed force microscopy and nanoindentation

Recently several atomic force microscopy (AFM)-based surface property mapping techniques like pulsed force microscopy (PFM), harmonic force microscopy or Peakforce QNM®, have been introduced to measure the nano- and micro-mechanical properties of materials. These modes all work at different operating frequencies. However, complex materials are known to display viscoelastic behavior, a combination of solid and fluid-like responses, depending on the frequency at which the sample is probed. In this report, we show that the frequency-dependent mechanical behavior of complex materials, such as polymer blends that are frequently used as calibration samples, is clearly measurable with AFM. Although this frequency-dependent mechanical behavior is an established observation, we demonstrate that the new high frequency mapping techniques enable AFM-based rheology with nanoscale spatial resolution over a much broader frequency range compared to previous AFM-based studies. We further highlight that it is essential to account for the frequency-dependent variation in mechanical properties when using these thin polymer samples as calibration materials for elasticity measurements by high-frequency surface property mapping techniques. These results have significant implications for the accurate interpretation of the nanomechanical properties of polymers or complex biological samples.

Sweers KKM, van der Werf KO, Bennink ML, Subramaniam V. (2012) Nanoscale 4:2072-2077

ABSTRACT (CONTINUATION)

The calibration sample is composed of a blend of soft and hard polymers, consisting of low-density polyethylene (LDPE) islands in a polystyrene (PS) surrounding, with a stiffness of 0.2 GPa and 2 GPa respectively. The spring constant of the AFM cantilever was selected to match the stiffness of LDPE. From 260 Hz to 1100 Hz the sample was imaged with the PFM method. At low frequencies (0.5 – 35 Hz), single-point nanoindentation was performed. In addition to the material's stiffness, the relative heights of the LDPE islands (with respect to the PS) were determined as a function of the frequency. At the lower operation frequencies for PFM, the islands exhibited lower heights than when measured with tapping mode at 120 kHz. Both spring constants and heights at the different frequencies clearly show a frequency dependent behavior.

INTRODUCTION

Atomic force microscopy (AFM) is widely used to study (bio)materials for their nanoscale morphological properties. Aside from these morphological studies AFM is also a suitable tool to characterize the mechanical properties of materials on the nanoscale [1-3]. Nanoindentation with an AFM tip is the most widely used method to determine nanomechanical properties of polymers [4-6]. In this mode the tip approaches and indents the sample until a certain predefined force is reached. At this point the tip is retracted. During this approach and retract cycle the force is continuously measured, resulting in a force versus distance graph, from which the modulus of elasticity can be derived using different contact models [7-9]. Besides the information in the force curve itself, the residual indentation depth measured with the AFM imaging mode could also be translated into hardness values of the polymers [6,10].

The approach-retract cycle in nanoindentation is typically performed at a rate of 0.5 to 10 Hz, which makes this method inherently slow. Nanoindentation can also be used in a force-volume mode to get an overview of the mechanical properties of a sample. In this approach, a complete force curve is recorded for every pixel in an image, which results in data acquisition times of up to hours for a single image.

Recently several high-speed surface property mapping techniques like pulse force microscopy (PFM), harmonic force microscopy and Peakforce QNM have been introduced [11-13]. These modes work on the same principle as the conventional nanoindentation approach but at far higher frequencies, leading to a significantly higher data throughput. These modes are used to obtain mechanical information on polymers [11,14], and are also increasingly used on biological materials like DNA or amyloid

proteins [15-16].

However, complex materials like polymers and biological materials are known to display viscoelastic behavior, a combination of solid- and fluid-like responses depending on the frequency at which the sample is probed [17-19]. In spite of this known behavior, very few AFM studies have attempted to characterize the frequency-dependent modulus of elasticity of complex materials. Kim et al. studied the response of PDMS, a polymer with a surface stiffness similar to that of biological samples, probed at different frequencies [20]. They clearly showed the viscoelastic response of PDMS within the frequency range of 1 Hz to 1000 Hz. Yang et al. demonstrated the viscoelastic behavior of poly (vinyl alcohol) nanofibers suspended over a channel [21]. A few studies on biological samples such as filaments or cells have also been performed [22-24], but these studies have typically been limited to a small frequency range, mostly in the conventional nanoindentation frequency regime.

We use the AFM in nanoindentation mode and PFM mode to study the frequency dependent behavior of low-density polyethylene (LDPE) using a standard 'training' sample supplied by Bruker (Bruker, Santa Barbara CA, USA). This sample is often used as a calibration sample for the surface property mapping techniques like Peakforce QNM or HarmoniX. A previous study showed that the elastic modulus of LDPE increases when probed between 0.5 Hz to 1000 Hz at room temperature [25]. Here we show that with increasing frequency, up to frequencies frequently used in methods such as PFM or Peakforce QNM®, the apparent stiffness (which is proportional to the elastic modulus) of the LDPE increases. This study demonstrates the ability, with the development of these new mechanical property mapping methods, to probe nanoscale rheological behavior of materials with AFM, at much broader frequency ranges than so far possible. Moreover, these results show that the frequency-dependent variations in mechanical properties of a sample like LDPE are very prominent in the frequency range used in these surface property mapping methods. Such samples should therefore be used with care for calibration purposes.

MATERIAL & METHODS

SAMPLE & TIP

The sample consists of a surface of polystyrene (PS) with phase separated islands of low-density polyethylene (LDPE) spin coated on top of a silicon plate (HarmoniX training sample PS-LDPE, Bruker, Santa Barbara CA, USA). The PS layer has a thickness of 20-30 nm and has a bulk modulus of elasticity of 2 GPa. The LDPE islands are

around 2000 nm in diameter and 30-45 nm thick and have a bulk modulus of elasticity of 0.2 GPa.

The sample is scanned and indented with an MSCT tip F cantilever (Bruker, Santa Barbara CA, USA). For both single-point nanoindentation and pulsed force microscopy experiments one single cantilever is used to be able to compare the results. The nominal spring constant of this cantilever is 0.5 N/m, the nominal tip radius is 10 nm and the resonant frequency is around 120 kHz. This spring constant (or stiffness) of the cantilever is matched with the stiffness of the LDPE, in order to be sensitive for changes in the elastic properties of the LDPE. The stiffness of the PS however, is much higher compared to the cantilever spring constant, rendering this method insensitive for the elastic properties of the PS. This means that the PS layer is perceived to be as stiff as the silicon layer underneath. The stiffnesses extracted from the force curves recorded on the bare silicon substrate and the PS layer indeed did not show significant differences.

SINGLE-POINT NANOINDENTATION

A Bioscope Catalyst microscope (Bruker, Santa Barbara CA, USA) was used for the single-point nanoindentation experiments. The measurements were performed with the "point and shoot" application in the NanoScope 8.10 software. To locate the LDPE drops, we first imaged the sample in tapping mode. Thereafter, the tapping amplitude was set to zero and indentation curves were made in the TM deflection mode as implemented in the Nanoscope 8.10 software. The maximum force applied on the sample was on average around 10 nN. In total 5 curves each on the PS and on a LDPE drop were recorded at different frequencies, namely at 0.5 Hz, 1 Hz, 2 Hz, 5 Hz, 10 Hz, 20 Hz and 35 Hz. The slopes of the retract curves were determined by fitting a linear function to the data for the first 5 nm, ultimately resulting in average slopes for PS and LDPE. We only used only the first 5 nm of the curve (that is, < 20% of the sample thickness) to account for finite sample thickness effects [26]. At each measurement frequency, we then calculated the stiffness of LDPE.

PULSED FORCE MICROSCOPY ON WITEC

The pulsed force microscopy (PFM) method was used as implemented on a WITec alpha300 microscope series (WITec alpha 300 microscope, WITec focus innovations, Germany). In the PFM method the cantilever is driven with a sinusoidal function and allows a maximum force setpoint; here a setpoint of 0.5 V (17.5 nN) was used. This force resulted in a maximum indentation, at the lower frequencies, of 3.5 nm, which is well under 20% of the total LDPE thickness. The cantilever is continuously in contact

with the sample to avoid snap-in/snap-off effects due to adhesion forces, especially on the PS part of the sample. This gives direct control of the amplitude of the sinusoidal function (50-60 nm on PS). The software generates several images including error signal and topography, which are built up by measuring the z-stage displacement required to maintain the setpoint force. Three additional images are created by choosing three different user-defined regions in the sinusoidal signal (see Figure 1A): red region for the maximum force, a green region for the slope (called stiffness in the software) and a blue region we use for minimum force to get information about the amplitude. Furthermore, it is possible on this microscope to change the drive frequency. A frequency range of 260 Hz to 1100 Hz with steps of 50 Hz was used to measure the sample. The average height and slope (representing the measured stiffness, or the contact stiffness) values for a large LDPE island were determined and compared to the direct PS surrounding of the island. With these values the stiffness of LDPE was calculated.

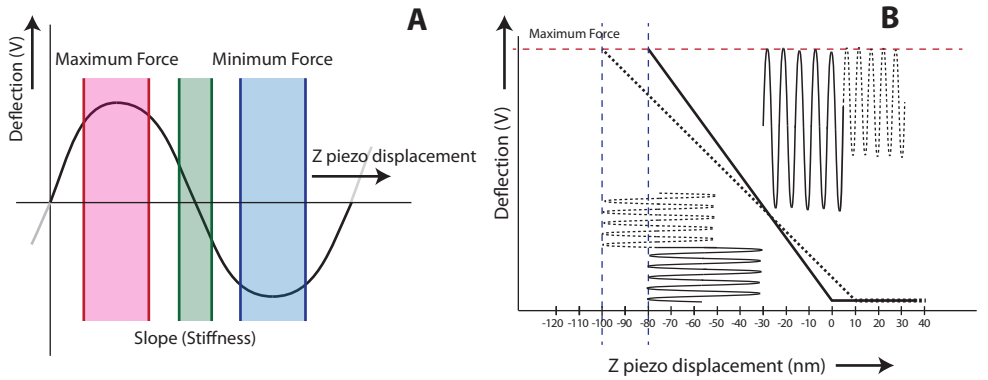

FIGURE 1; PFM principle as implemented on WITec alpha 300 microscope. Panel (A) shows the deflection signal with the three regions: maximum force (red area), slope (green area) and minimum force (blue area). The maximum force of the sine wave is the same as the force setpoint. The slope of the deflection in the green region is proportional to the measured stiffness (or contact stiffness) and changes as the elastic properties of the material being probed are changing. Panel (B) shows 2 force curves on both a hard sample (e.g., PS, solid line) and a softer 10 nm higher feature (e.g. LDPE island, dashed line. The vertical sine wave represents the signal that is used for driving the cantilever, which amplitude remains constant during the measurement. The resulting (measured) deflection signal is displayed horizontally and indicates a higher amplitude (steeper slope) on a hard sample compared to a soft sample. As the AFM tip indents the soft sample, the stage has to travel longer to reach the same force setpoint (the vertical blue lines indicate the z stage position), resulting in a lower height in the topography image and a smaller amplitude (or lower slope) indicating a softer material.

MODULUS OF ELASTICITY VALUES OF LDPE FROM SINGLE-POINT NANOINDENTATION

The raw deflection curves on LDPE, obtained on the Bioscope Catalyst AFM at 0.5 Hz & 10 Hz, were converted to a force separation curve using the deflection sensitivity of the cantilever and the nominal spring constant provided by the manufacturer. The modulus of elasticity of LDPE was determined from the first 5 nm of the slope of the separation curve according to the DMT model 2,8, using an estimated tip radius of 25 nm, spring constant 0.5 N/m and a Poisson ratio of 0.45.

RESULTS

Figure 2 shows two examples of the nanoindentation curves obtained at 0.5 Hz and 10 Hz. Both graphs show differences in the slopes of the curves corresponding to the LDPE and PS domains. The stiffness of LDPE is calculated with the following equation:

$$\frac{1}{k_t} = \frac{1}{k_c} + \frac{1}{k_s}$$

where k_t is the measured stiffness, k_c the cantilever stiffness (spring constant) and k_s the stiffness of the probed sample, here that of LDPE. From the curves shown in Figure 2 the calculated LDPE stiffness changes from 0.18 N/m at 0.5 Hz to 0.46 N/m at 10 Hz. Applying the DMT model to the force separation curves measured at both frequencies yields modulus of elasticity of 349 MPa at 0.5Hz and 787 MPa at 10 Hz.

Figure 3 shows the images of the slope and height measured at different frequencies obtained with the WiTec AFM. The images of the slope clearly show a decreasing contrast between PS and LDPE at increasing frequencies. The slope on the PS stays constant due to the insensitivity of the chosen cantilever (see Materials and Methods) for the stiff PS. This indicates that the material increases in stiffness with increasing frequency. In the topography images the height increase of the LDPE islands compared to the PS is clearly visible, as the frequency is increasing. This height increase is caused by the implementation of the image method, that is, the cantilever needs to travel a longer distance on a soft sample (LDPE island) compared to a hard surface (PS) with a predefined force setpoint (Figure 1B). At low frequencies, where the LDPE behaves as a soft material, the height signal is lower than the surrounding PS, due to the AFM tip sinking into the material. However, at higher frequencies, where the LDPE has a higher stiffness, the height signal corresponding to the LDPE is higher than that of the surrounding PS, and approaches values closer to the height measured in tapping mode (around 10 nm).

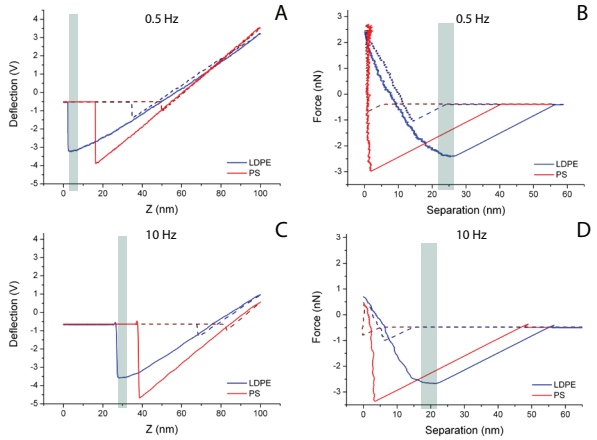

FIGURE 2; Examples of the raw nanoindentation deflection curves at 0.5 Hz (A) and 10 Hz (C) and their corresponding force separation curves (B&D). Dotted and solid lines represent approach and retract curves respectively. Blue curves are measured on LDPE and red curves on PS. Due to indentation in a soft material and the finite-sample thickness effects the curves on LDPE are clearly not linear. Therefore the analysis of the raw deflection and separation curves is done on the first 5 nm (grey bars in graphs).

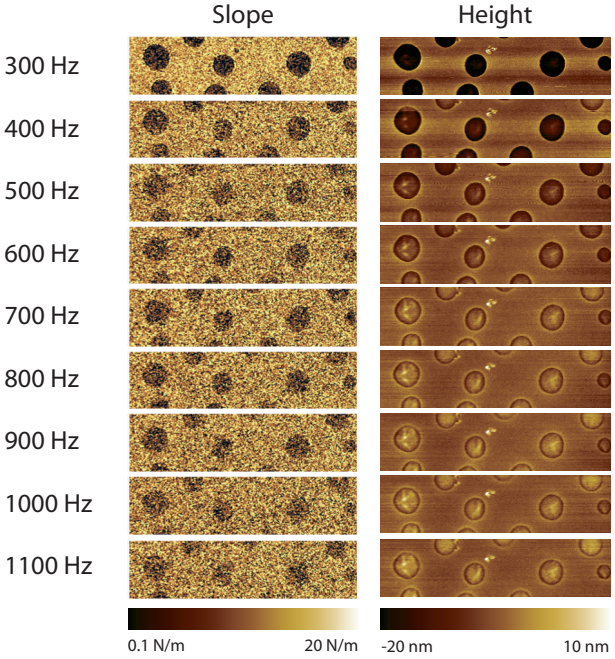

FIGURE 3; Slope and topography images recorded with PFM at different frequencies. Image sizes are 10x2.5 µm. The contrast in the slope is very clear at low frequencies, whereas this contrast diminishes at higher frequencies. The heights of the LDPE islands are below the PS surface at the lower frequencies and gradually come up as the frequency is increased.

Figure 4A shows the height increase of the LDPE islands compared to the PS surrounding measured with PFM, and also shows the actual height measured with tapping mode at 120 kHz. This graph shows the frequency dependent effect already depicted in the image series of Figure 3. The spring constants for LDPE calculated from the slopes of the curves acquired by both methods with equation 1 are plotted versus frequency in Figure 4C. For the stiffness calculations from the PFM results an area of interest is drawn on the LDPE island and the average spring constant of this area is used in the equation shown in Figure 4D to calculate the LDPE stiffness (Figure 4D). The increase in stiffness with increasing frequency is clearly visible, even at lower frequencies (inset

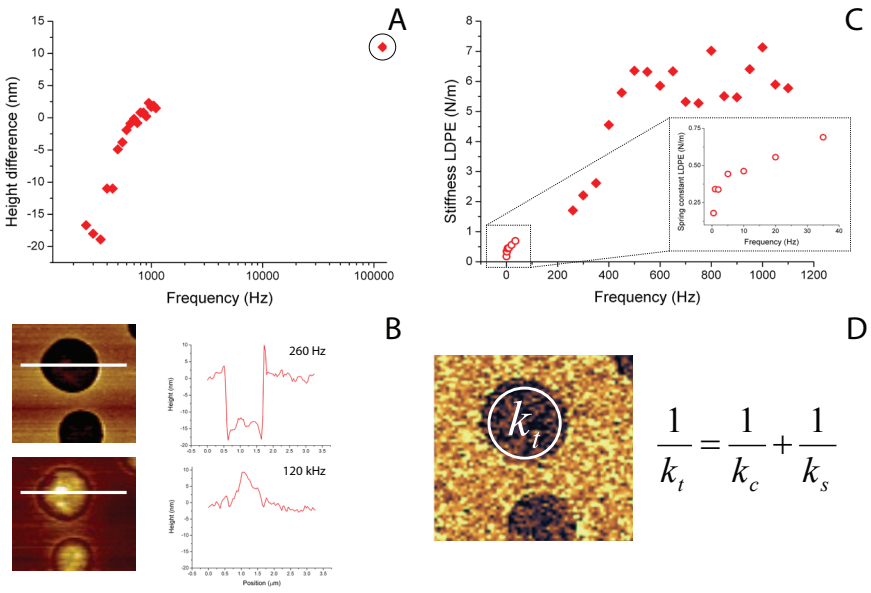

FIGURE 4; Single-point nanoindentation and PFM results. (A) The height of a large LDPE island, compared to the PS surrounding, from the PFM images are plotted as a function of frequency. The circled data point depicts the height of the same island measured with tapping mode. (B) Examples of line profiles of the large LDPE islands at 260 Hz (upper image) and at tapping mode frequency of 120 kHz (lower image). (C) Frequency-dependent LDPE stiffness calculated from both single-point nanoindentation (open circle data points) and PFM measurements (filled diamond data points). Inset is zoom of the single-point nanoindentation results at the lower frequencies. (D) Short description of spring constant calculation method with the PFM results, where kt is the total measured spring constant, kc the cantilever spring constant and ks the contact stiffness of the sample.

of Figure 4C)DISCUSSION & CONCLUSION

The graph in Figure 4A, where the height measurements performed in PFM mode are combined with the actual height measured in tapping mode AFM, clearly shows the

frequency dependent behavior. The graph indicates that at lower operating frequencies the AFM measures the LDPE islands as being a softer material, resulting in the islands appearing as holes in the sample (Figure 4B). The height measured with tapping mode AFM is commonly assumed to be the true height. In tapping mode, the cantilever essentially probes the sample at such a high frequency (120 kHz). At this frequency the material is extremely stiff, resulting in hardly any indentation under the applied force. These attributes makes it possible to gently image very soft and delicate samples, for instance live cells, using tapping mode imaging [27].

While the height images made with PFM show very good contrast, the slope images have a low signal to noise ratio. For the height analysis presented here, we draw a line profile across the LDPE island and measure the difference between the PS background and the highest point of the LDPE island (Figure 4B). The high noise level in the slope images made analyses of single line profiles difficult, and we thus chose to compute average values over a substantial area of an island (defined by the white circle in Figure 4D) for the stiffness calculations.

Figure 4C shows a clear dependence of the LDPE spring constant on the frequency. At the lowest frequency, 0.5 Hz, the LDPE spring constant is similar to the cantilever spring constant. Around 35 Hz the LDPE spring constant is already 5 times higher compared to the cantilever spring constant (see inset of Figure 4C). The gap in the data between 35 Hz and 260 Hz is attributed to instrumental limitations. Specifically, the PFM implemented in the WITec system was not capable of performing the measurements with the required force settings at operating frequencies below 260 Hz. Additionally, the nanoindentation software implemented on the Bioscope Catalyst automatically reduces the number of samples/pixels in the curve when measuring above 10 Hz. Above 35 Hz the number of pixels are reduced to less than 128 pixels, a value that appeared to be insufficient for robust analysis. At the higher frequencies, starting around 400 Hz, the LDPE stiffness approaches the maximum stiffness measurable with this particular cantilever. The stiffness measured on LDPE is related to the modulus of elasticity of LDPE, and the geometric contact volume of the probing tip. In this study we varied the force on the sample in contrast to bulk rheology measurements, in which the displacement is varied. We did not observe a distinct phase shift during the measurements, that is, no phase difference between the drive signal and the deflection signal. We used the same tip for the indentation measurements, and indented only a few nanometers. From this we can conclude that this is pure elastic behavior and proportional to the storage modulus, G' of the LDPE. The G' of LDPE as a function of the frequency has been measured by Capodagli et al. using bulk rheology, and the frequency increase is in the same range as our results [25]. Future studies comparing this AFM technique with

bulk rheology measurements of samples with the same thermal history should be done to get insights into whether absolute values of G´ are in good agreement.

The modulus of elasticity values found for LDPE in this study are slightly higher compared to the provided value of around 200 MPa. However, the values we extract are in the same range as previous nanoindentation studies of LDPE [6,28]. Considering that the analysis of moduli of elasticity from contact models, like the DMT model used in this study, require many assumptions on contact areas, point of contact, Poisson ratio and spring constant calibration methods, we therefore chose to analyze our data only in terms of stiffness values. Also, since the LDPE islands are only 30-40 nm in thickness, the results are prone to finite sample thickness effects [26,29]. The maximal indentation on LDPE on the PFM measurements was 3.5 nm (less than 20% of the full thickness). For the single-point nanoindentation measurements we only used the first 5 nm of the curve for analysis. To exclude that the frequency-dependent behavior measured here is induced by plastic deformation caused by the multiple scans, the sample was scanned in PFM mode at 260 Hz for multiple times in the same time span as the variable frequency series. However, there was no effect seen in the height images during a 70-minute time span (Figure 5), confirming that the results shown in Figure 3 are indeed attributable to a purely elastic effect which is frequency-dependent.

We observed an increase in the LDPE stiffness within 400 Hz. This increase and the repeated measurements at one frequency show that results obtained at a certain frequency could be very reproducible (Figure 5), but that they are completely different when compared to the results measured at different frequencies. For LDPE this apparent stiffness already increases by a factor of 2 when going from 0.5 Hz to 2 Hz. It is thus crucial to report the frequency at which nanomechanical properties are measured for effective comparison of experimental data. The shape of the stiffness curve obtained here is specific for the LDPE material [25,30].

High speed surface property modes are often calibrated with a training sample composed of copolymer blends, such as the LDPE/PS blend used here. The LDPE component of this sample is very soft and proven to be very frequency dependent. This polymer is used in the calibration sample because the modulus of elasticity is close to the moduli of elasticity of biological samples. However the question remains whether the frequency dependent behavior is also comparable to other polymers and especially to biological materials. The new surface property mapping methods probe at very high frequencies compared to the conventional nanoindentation technique. Although the data throughput is very fast, one should combine the results with nanoindentation measurements at low frequencies. In this manner the frequency dependent behavior of the sample, which could influence the measurement and analyses, can be studied. Furthermore,

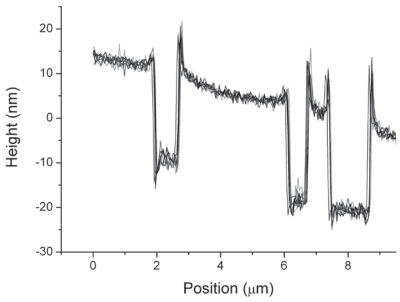

FIGURE 5; Line traces of 7 topographic images made with the PFM method in a period of 70 minutes at 260 Hz with similar settings as the frequency series. The traces show no height increase as seen in Figure 3, which confirms that the results shown in Figure 3 are truly frequency dependent.

it is very important to calibrate the measurement system with a calibration sample which exhibits elastic and viscoelastic behaviors that are close to those of the actual sample to be measured. The results obtained in this study show that frequency dependent behavior of a sample like LDPE is very prominent in the frequency range used in the recently developed surface property mapping methods. These approaches should be calibrated with the deflection sensitivity, spring constant and tip radius of the cantilever instead of with the training samples alone. Finally, all mechanical properties measured with these surface property mapping techniques or with conventional nanoindentation should be reported with explicit mention of the frequency at which the sample is probed.

In this study we have shown that in addition to measuring morphological and elasticity properties, AFM is also very well suited to investigate frequency dependent behavior of complex materials. The results obtained are very similar to those from bulk rheological studies [25,30], with the added advantage of being able to spatially resolve these properties at exceedingly small length scales. Although a few studies on nano/micro-rheology using AFM exist, they are still limited to narrow frequency ranges, often below 100 Hz [24,31,32]. We demonstrate that, with the development of the new nanomechanical mapping techniques, AFM can be used to obtain frequency-dependent modulus of elasticity curves of nanometer sized single polymer or biological samples in considerably larger frequency ranges, which are not accessible to conventional rheology.

REFERENCES

1. Yang L, van der Werf KO, Koopman BFJM, Subramaniam V, Bennink ML, Dijkstra PJ, Feijen J. (2007) J. Biomed. Mater. Res. 82:160-168
2. Sweers K, Werf K, Bennink M, Subramaniam V. (2011) Nanoscale Res. Let. 6:270

3. Knowles TPJ, Buehler MJ.(2011) Nat. Nanotech. 6: 469-79
4. Bhuyan S, Sundararajan S, Andjelkovic D, Larock R. (2010) Tribology 43:2231-39
5. Celik E, Oterkus E, Guven I, Madenci E. (2009) IEEE 262-268
6. Jee AY, Lee M. (2010) Polym. Test. 29:95-99
7. Hertz HJ. (1882) Reine Angew. Math 94:156-171
8. Derjaguin BV, Muller VM, Toporov YUP. (1975) Colloid Interf. Sci 53:314-26
9. Johnson KL, Kendall K, Roberts AD. (1971) Proc. R. Soc. London A 324:301-13
10. Tranchida D, Kiflie Z, Piccarolo S. (2007) Macromolecules 40:7366-71
11. Pittenger B, Erina N, Su C. Application Note Veeco Instruments Inc. http://nanoscale-world.bruker-axs.com/nanoscaleworld/media/p/418.aspx
12. Rosa-Zeiser A, Weilandt E, Hild S, Marti O. (1997) Meas. Sci. Technol. 8:1333-38
13. Sahin O. (2007) Rev. Sci. Instrum. 78:103707
14. Schön P, Bagdi K, Molnár K, Markus P, Pukánszky B, Vancso GJ. (2011) Eur. Polym. J. 47:692-98
15. Sahin O, Erina N. (2008) Nanotechnology 19:445717
16. Dong M, Husale S, Sahin O. (2009) Nat. Nanotechnol. 4:514-17
17. Nho YC, Kim JI, Kang PH. (2006) J. Ind. Eng. Chem. 12:888-92
18. Meissner J. (1975) Pure and Appl. Chem. 42:551-612
19. Van der Vegt AK. Polymeren, van keten tot kunststof. Delft University Press 1999
20. Kim KS, Lin Z, Shrotriya P, Sundararajan S, Zou Q. (2007) Proc. 3rd Ann. IEEE Conf. Aut. Sci. Eng. SuRP-B02.1:219-224
21. Yang N, Wong KKH, Bruyn JR, Hutter J. (2009) Meas. Sci. Technol. 025703(9pp)
22. Chaudhuri O, Parekh SH, Fletcher DA. (2007) Nature 445:296-98
23. Knowles TPJ, Oppenheim TW, Buell AK, Chirgadze DY, Welland ME. (2010) Nat. Nanotech. 5:204-207
24. Bremmel KE, Evans A, Prestidge CA. (2006) Coll. Surf. B: Biointerfaces 50:43-48
25. Capodagli J, Lakes R. (2008) Rheol. Acta. 47:777-86
26. Sullan RMA, Gunari N, Tanur AE, Chan Y, Dickinson GH, Orihuela B, Rittschof D, Walker GC. (2008) Biofouling 25:263-275
27. Putman CAJ, Van der Werf KO, de Grooth BG, Hulst NF, Greve J. (1994) Biophys. J. 67:1749-53
28. Passeri D, Bettucci A, Biagioni A, Rossi M, Alippi A, Lucci M, Davoli I, Berezina S. (2008) Rev. Sci. Instr. 79:066105
29. Guo S, Akhremitchev BB. (2006) Biomacromolecules 7:1630-36
30. Yamaguchi M, Abe S. (1999) J. appl. Polym. Sci. 74:3160-64
31. Mahaffy RE, Shih CK, MacKintosh FC, Käs J. (2000) Phys. Ref. L. 85:880-83
32. Roca-Cusachs P, Almendros I, Sunyer R, Gavara N, Farré R, Navajas D. (2006) Biophys. J. 91:3508-18

CHAPTER 9

Nanoscale patterned materials for mechanical characterization of α-synuclein fibrils using atomic force microscopy

The protein α-synuclein has a propensity under specific conditions to aggregate into larger fibrillar structures. This aggregation is associated with the development of Parkinson's disease. Mechanical characterization of these micrometers long, but only 10 nm in diameter, amyloid fibrils is becoming increasingly interesting from both a biological and engineering point of view. One approach to mechanically characterize these fibrils is by suspending them across channels or pores and testing them for bending. In this exploratory study we investigated several patterned surfaces to be used for these mechanical bending tests. We furthermore tested whether these amyloid fibrils have affinity for these surfaces and whether they, upon random deposition from solution, end up freely suspended across the channels or pores. Although the fibrils do adhere firmly to some of the surfaces, no suspended parts of the α-synuclein fibrils have been observed. We propose an alternative approach in which the fibrils are pushed sideways to test for bending.

INTRODUCTION

Misfolding of proteins and aggregation into fibrillar structures are the pathological hallmark of various neurodegenerative diseases like Alzheimer's, Huntington's and Parkinson's disease. In the case of Parkinson's disease (PD) the relevant protein is α-synuclein, a small 140 amino acid natively unfolded protein [1-3]. Structural and morphological characterization of these protein fibrils has been performed with atomic force microscopy [Chapters 5 & 6, refs 4 & 5], nuclear magnetic resonance and electron microscopy [6]. A handful of studies have mechanically characterized α-synuclein fibrils. Most of these use AFM-based nanoindentation [Chapter 7] or high-resolution AFM imaging, in which the curvature of the amyloid fibril is used to calculate the flexural or bending rigidity [Chapter 6]. Here, we aimed for a different type of mechanical characterization method that has been previously demonstrated on silicon nanofibers [7], elastic fibers [8] and collagen fibrils [9]. In these studies the samples were suspended across channels of suitable dimensions, which allowed testing these fibrils for bending under the application of force using an atomic force microscope. From the recorded force-distance data, the mechanical properties of the fibrils can be extracted.

Although this technique was very successful for bending collagen fibrils, which typically have a diameter of 100 to 200 nm, it is far more challenging for amyloid fibrils which have diameters of only about 10 nm. A single report has successfully demonstrated bending of insulin amyloid fibrils on a gold-coated silicon channel patterned surface [10]. The challenges are twofold. Firstly, due to the small size of the fibrils it is difficult to accurately determine location of bending on the suspended part of the fibril with the AFM tip. In the case of collagen fibrils an optical microscope was able to clearly resolve the fibrils enabling guiding and positioning of the AFM cantilever in a rather straightforward manner [9]. 10 nm fibrils are not resolved in an optical microscope. The AFM must be used first to image the protein fibril crossing the channel, before the cantilever can be positioned accurately on top of it. When the tip is even slightly off-center, the forces obtained are not only from pure bending but will also include shear components. The second reason why these bending experiments are far more challenging when applied to amyloid fibrils is that the width of the channels needs to be around 50 to 200 nm. Fabrication of channels of such dimensions requires special fabrication techniques such as E-beam lithography in combination with deep etching technologies, or nano-imprint technologies. The actual required widths of the channels depend on a number of factors, including the bending rigidity of the fibril itself, its adhesion to the surface, and its resistance to breaking. The width of 50 to 200 nm is based on the work of Smith et al., and serves as a starting point [10].

In this study we explored six different surfaces that can be used as a substrate for

bending experiments on α-synuclein fibrils. We have fabricated nanochannels (140 nm width) in polymethylmethacrylate (PMMA) and polystyrene (PS) with nanoimprint lithography (NIL) [11] and also used a commercially available silicon patterned surface, which was also used as a template for the NIL. Channels of around 50 nm were furthermore fabricated in glass with a focused ion beam. A gold surface with pores of various sizes (between 200 and 1000 nm) was fabricated and a polycarbonate membrane with pores of 50 nm was also investigated. Because none of the six patterned surfaces yielded a successful outcome, that is, an amyloid fibril suspended across a channel or pore, in the last section we discuss alternative strategies for bending amyloid fibrils.

MATERIALS & METHODS

ALPHA-SYNUCLEIN

We performed recombinant expression and purification of wild type & E46K α-synuclein protein as previously described [4]. To prepare the fibrils, a 100 μM monomeric wild type α-synuclein solution in 10 mM Tris-HCl, 50 mM NaCl, pH 7.4 was incubated at 70°C in glass vials (duplicates) under constant shaking conditions [4,5].

SUBSTRATES

Gold surfaces with holes were prepared using a template-stripping method [12]. Mica was freshly cleaved and subsequently a 50-nm gold layer was sputtered on top of it. (Sputter Coater 108, Cressington Scientific Instruments Ltd. Watford, England). As a next step a metal disk was glued on top of the gold using two-component glue and the sample was allowed to dry overnight. Afterwards the mica was carefully removed layer by layer until the gold surface was exposed. The resulting gold surface had a roughness equivalent to that of mica and contained holes of various sizes (200 nm up to 1000 nm) and depths of around 100 nm.

Isopore membrane polycarbonate, track-etched screen filter with pores were used as received (IsoporeTM Membrane Filters, Millipore, Billerica MA, USA)

Glass with channels of 50 μm long and 22 nm wide were created using focused ion beam milling. First a microscope glass slide was covered with a 10 nm gold layer. This sample was then processed with a focused ion beam (FIB, FEI NovaLab600, FEI, Eindhoven, The Netherlands) according to an ASCII file which is directly loaded in the machine's patterning board using a current of 93 pA. This structure was made in an area of 3 mm^2 on the glass.

Silicon surfaces patterned with channels 140 nm wide and 140 nm deep (280 nm

pitch) were used as received (LightSmyth Technologies, Eugene OR, USA).

Nanochannels in polymethylmethacrylate (PMMA) and polystyrene (PS) were fabricated using nanoimprint lithography. For the first substrate 4% PMMA (140 kDa) in toluene was used and for the second substrate polystyrene in toluene (PS). These solutions were spin coated on a wafer of around 15 mm by 15 mm in size for 30 seconds at 3000 rpm. This resulted in layers of around 5 μm thickness. For solvent removal the silicon/polymer layers were baked in a vacuum oven for 1 hour at 120° C and 0.1 bar.

Silicon surfaces patterned with channels 140 nm wide and 140 nm deep (280 nm pitch, LightSmyth Technologies, Eugene OR, USA) were used as stamps for the nanoimprinting. Before imprinting, these silicon stamps were silanized using a perfluorinated alkylsilane by chemical vapor deposition (CVD) followed by curing for one hour at 100° C.

The imprinting was done using a manual press (Specac HP, Cranston, USA) with hot plates. In the press the stamp was pressed into the PMMA layer for twenty minutes at a pressure of 0.4-0.6 tons of weight and a temperature of the plates of 180° C. This temperature is well above the glass transition temperature (TC=125° C) of PMMA, required for making the material fluid enough to press the stamp in a non-destructive way into the polymer [13]. For polystyrene samples the same method was used with temperatures of 160° C, adjusted to the glass transition temperature of PS (TC=95° C).

ATOMIC FORCE MICROSCOPY

All surfaces were characterized on a Bioscope II or Bioscope Catalyst AFM (Bruker, Santa Barbara CA, USA). Channel and pore sizes were measured in air with an NSC36 probe (Mikromash, Tallin, Estonia) in tapping mode with an amplitude reduction of 70% from the free 100 nm amplitude. Tapping mode imaging in liquid conditions (buffer solution 10 mM Tris-HCl, 50 mM NaCl, pH 7.4) was performed on the same instrument equipped with a MSCT, tip F cantilever (Bruker, Santa Barbara CA, USA) with an amplitude reduction of 90% from the free 5 nm amplitude.

RESULTS

Six different substrates with channels or pores in the range of 100 to 250 nm have been acquired or fabricated and imaged with tapping mode AFM in ambient conditions. The six different surfaces are numbered according to the following list:

Surface 1. Surface template-stripped gold layer with pores.

Surface 2. Polycarbonate membrane with pores.

Surface 3. Focused ion beam glass sample with channels.

Surface 4. Silicon surface with channels.

Surface 5. Nanoimprinted PS surface with channels

Surface 6. Nanoimprinted PMMA surface with channels

We argued that we need channels or pores between 50-200 nm in width and at least 50 nm in depth to be able to actually push the fibril with an AFM tip in the channel. It is further necessary to be able to spatially resolve the fibrils on the surface, thus requiring the surface roughness to be less than the average fibril height (around 10 nm).

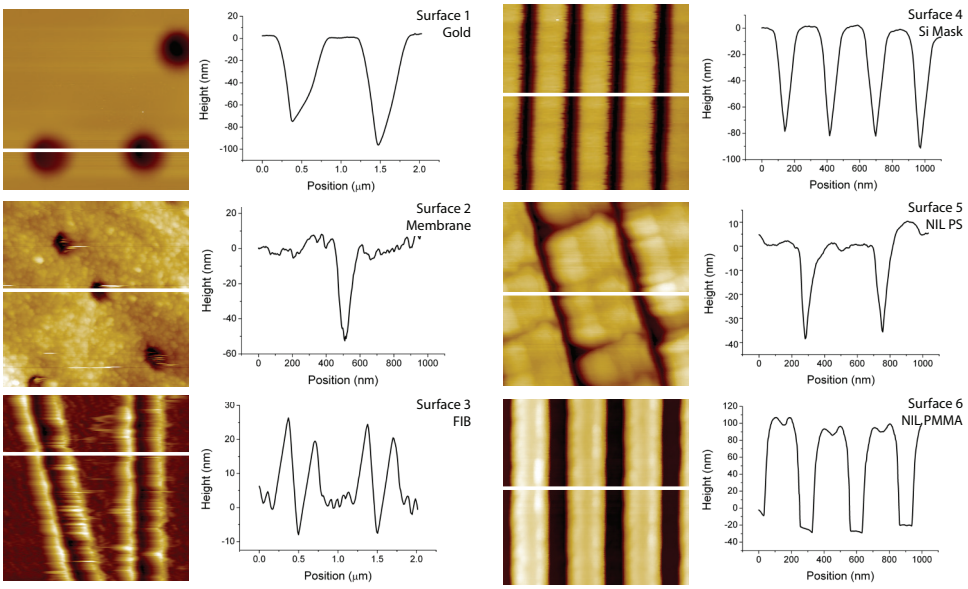

FIGURE 1; Height images of the 6 surfaces with corresponding line profiles. All images are 1x1 μm or 2x2 μm in size, see the line profiles for the size. All images are representative for a larger part of the surface except the one for surface 5, which was the best obtainable result.

The results of imaging the surfaces are displayed in Figure 1. The pores on surface 1 (template-stripped gold surface) and surface 2 (polycarbonate membrane) are respectively 90 and 50 nm deep, which is sufficient to perform the bending tests. The surface roughness of sample 2 is 11.7 nm (average of 17 images). Fibrils are similar or smaller in size so makes it difficult to locate the fibrils on the surface. The underlying mechanism of how the pores appear in the template stripping method (surface 1) is not understood and hence not controlled. The surface roughness is about 0.14 nm [Chapter 3] The size and number of pores was not controlled and fluctuates greatly. Surface 3, the glass surface into which channels have been milled using a focused ion beam, showed

channels with a width of around 22 nm, see Figure 1, which was expected with the chosen current used for the milling process. However, the material which was removed by the beam is redeposited right next to the channel creating high rims. Surface 4 (the Si mask) and surface 6 (the nano-imprinted replica in PMMS both displayed channels 140 nm in width. The depth of the stamp obtained from the image is lower than the intended 140 nm, but from the height profile it is clear that this is due to the finite size of the AFM tip. Surface 5 (the nanoimprinted replica in PS) did not display channels as expected based on the stamp used (surface 4). The example of surface 5 showed in Figure 1 is not typical and is the best result obtained in this study. Most other areas on this sample did not show any channels or the channels appeared to have large rims on the side. Therefore, this sample was excluded for further analysis.

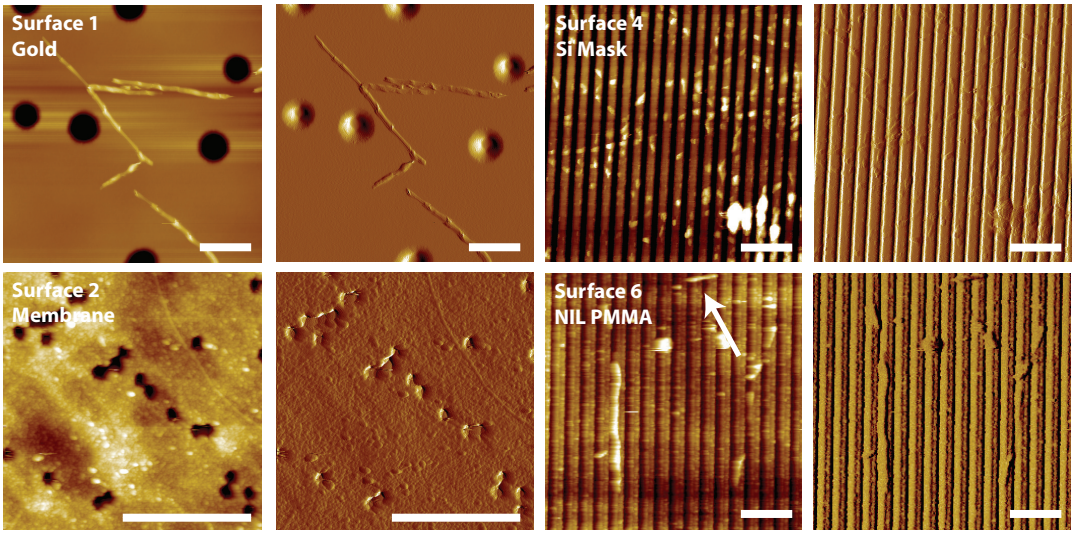

FIGURE 2; AFM height and error images of 4 different surfaces with wild-type α-synuclein. (A) Surface 1, the template-stripped gold surface, showing fibrils but none crossing the pores. Z-scale is 168 nm. (B) Surface 2, the polycarbonate membrane with a single fibril which is not clearly seen due to the rough surface, Z-scale is 143 nm. (C) Si surface with 140-nm channels, showing fibrils that appeared to be completely sunken into the channels. Z-scale is 176 nm. (D) PMMA surface with 140-nm nano-imprinted channels, showing fibrils aligned alongside or in the channels. Z-scale is 96 nm. All images have a scale bar of 1 μm and are recorded in air except surface 1, which is recorded in liquid.

After incubation of the 5 remaining surfaces with an undiluted α-synuclein fibril solution and rinsing with ultrapure water for measurements in air and with 10 mM Tris-HCl for liquid measurements, tapping mode images were recorded in both air and liquid. When imaged in liquid conditions, fibrils were only found on surface 1. In ambient air conditions all samples showed fibrils except for the FIB-fabricated glass surface, number 3. The area on which FIB channels were made was only 3 mm^2. Interestingly,

fibrils were found on the part of the gold layer that was not patterned. Due to the relatively high roughness (11.7 nm) of the polycarbonate membrane (surface 2) it was difficult to localize the protein fibrils on the surface.

None of the fibrils were observed actually crossing the pores on surface 1 and surface 2. The fibrils did cross the channels on the silicon mask sample, surface 4. However, the fibrils appear to be completely sunken into the channels. On surface 6, fewer fibrils were found compared to surface 4 and these fibrils appear to align with the channels, both on top or maybe even in the channels. One small fibril seems to cross a channel at the top of the image of surface 6, indicated with a white arrow in Figure 2.

DISCUSSION

In chapters 3 and 4 we have reported that α-synuclein fibrils bind to different kinds of surfaces like mica, HOPG, gold, glass or membranes. However, the affinity of fibrils for mica and HOPG was larger than that for gold or glass. Although α-synuclein does bind to many surfaces with different affinities, it is unclear how the fibrils actually adsorb onto the surface. We envision two different adsorption possibilities, schematically depicted in Figure 3.

	Result 1 Fibril on top of or in the channels	**Result 2** Fibril crossed the channels
Option A 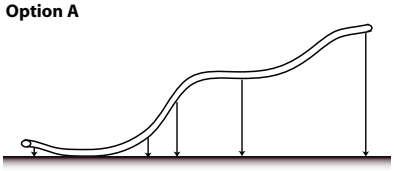 Part of the fibril touches the surface and adsorbs; the rest of the fibrils gently follows the adsorption process	**A1** Thermally it could be more favorable to stay completely on top or in the channels during the adsorption process	**A2** The fibril follows the surface contours. So it will also follow the edges of the channels and goes in and out of the channels
Option B 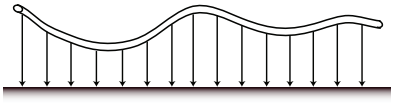 The fibril is 'trapped' by the surface; the adsorption process is instantly.	**B1** The fibril is after trapment still able to move around for some time and it will in the end choose to be completely on top or in the channel	**B2** Fibril is not able to move around and will stay suspended over the channel

FIGURE 3; Different mechanisms with which the fibril adsorbs onto the surface, and the result obtained depending on how the fibril is aligned with respect to the channels.

Option A describes the adsorption process in case the interaction of the fibril with the surface is relatively weak. A small part of the fibril touches the surface first and the rest of the fibril is pulled sequentially towards the surface. Since the interaction with the surface is weak the fibril is able to move on the surface. Option B describes the adsorption process in case the interaction is relatively strong; the fibril is instantly 'trapped' by the surface. The magnitude of the interaction is dependent on the physicochemical properties of both amyloid fibrils and the surface and the surrounding medium [Chapter 5].

Previously the curvature of α-synuclein fibrils on mica was compared to those on membranes and no difference in bending rigidity was found [Chapter 4]. This suggests that adsorption occurs as described in option A, where the system is continuously in thermal equilibrium. When we compare the different possibilities to the results obtained with αSYN fibrils on the different patterned substrates in this study we observe that, especially in liquid, most fibrils are aligned with the channels. It has never been observed that fibrils still move around on substrates after adsorption with the exception of supported lipid bilayers [Chapter 4]. Furthermore, the 'trapping' of the fibril is caused by a large adhesion forces; these forces are not likely to be overcome in order for the fibril to be able to move around afterwards. We therefore, according to the results obtained in this study, believe that option A is the most likely scenario for the adsorption process. However, in air we observe more fibrils crossing the channels. Possibility A2 seems less likely when one considers the persistence length of fibrils, which is reported to be in the hundreds of micrometers. It seems very unlikely that fibrils would fold around the corners of the channels if the fibrils indeed do have these large reported persistence lengths. This could indicate that the fibril does not behave as a semi-flexible polymer upon the drying process.

In summary, it is important to find a surface and surrounding medium which alter the adhesion forces in such a way that option B comes in to play. The fibrils are then trapped by the surface and the possibility to cross channels would greatly increase.

ALTERNATIVE SURFACES & SAMPLE PREPARATION

All surfaces investigated in this study have correct channel width sizes, according to the desired values mentioned in the introduction (50-200 nm), which was based on to the previously performed study [10]. For surface 3, the FIB surfaces, the channels were however not deep enough. In case of the gold surface, surface 1, often the pores were too large (up to 1μm), however the smaller pores were around 200 nm. The desired size ranges (50-200 nm) are dependent on the modulus of elasticity of the fibrils. When a fibril is rather flexible or the channel is very wide it will become easier for the adsorption

forces to pull the fibril down into the channel. However the fibrils do not seem to cross the channels or pores. The repetitive channel structures do seem to increase chances of crossing fibrils, especially upon drying. The fibrils are still sunken into the channels. An alternative for the sample preparation could be to induce a flow perpendicular to the channels to increase the probability of having fibrils that cross the channels.

Another problem is the small width of the channels. On one hand the width of the channel needs to be small enough to have a fibril spanning it. However, the channel cannot be too small, such that the AFM tip does not fit into the channel. This is already noticeable on surface 4. Although the channels are 140 nm in depth, the AFM tip cannot reach all the way down and measures a depth of only 50 nm (Figure 1).

To address the issues mentioned above we propose two alternative options. The first option could be to let the fibrils adsorb on filled channels (for instance a silicon mask with polymer-like substance); the fibrils are always supported in this way. After adsorption, the channels can be emptied by a suitable chemical or other process. However, to find a suitable material which can be removed without damaging the fibrils can be challenging. Also, when the required channel size is in the same size as the AFM tip, it does not resolve the tip versus channel size problem.

Both problems can be solved by functionalizing surfaces in the same repetitive line structures with partly adhesive and non-adhesive lines. For instance, one could use an α-synuclein variant with a cysteine in the C-terminus (for instance the A140C variant) which would firmly attach to gold lines. In between the gold lines a PEG layer could make sure that the fibrils are still able to move. The bending experiment could then be performed by moving the fibrils sideways instead of downward into a channel. This also solves difficulties with tip sizes that cannot fit in the channel or pore.

OBTAINING FREQUENCY DEPENDENT ELASTICITY CHARACTERISTICS

By pushing the fibril, in the channel or sideways, at various frequencies and measuring the response, it is possible to study the frequency dependent behavior. This rheological behavior is already studied for amyloid fibrils in network conformations, for instance for sheets [14]. In this study, the authors investigate the difference in modulus of elasticity at different frequencies of sheets formed by β-lactoglobulin. However, single amyloid fibrils are already complex structures that could exhibit both elastic and visco-elastic components and the frequency-dependent bending approach might be a method to get more insight into these properties.

CONCLUSION

In this exploratory study a few suitable surfaces were found for the bending experiments. All patterns were in the size range of 50 to 200 nm in accordance with a previous report [10].

The gold surfaces with pores made using template stripping from mica is easy to fabricate but the size, number and position of the pores is not controlled. However, no fibrils were observed crossing the pores. We showed that channel patterned surfaces increase the chance for channel crossing fibrils. Nanoimprinted PMMA even showed a single channel crossing fibril in liquid conditions.

Although a few suitable surfaces were found in this study, the question remains whether the approach in this study is the most appropriate one in terms of experimental ease. Possibly, the proposed sideways pushing method is an easier approach. The pattern size can be completely adjusted to the persistence length of the fibrils and experimentally fewer difficulties with finite AFM tip size are encountered.

REFERENCES

1. Goedert M. (2001) Nat. rev. neurosci. 2:492-501
2. Dobson CM. (2003) Nature 426:884-890
3. Schultz W. (2006) Proc. Natl. Acad. Sci. 103:1661-68
4. Raaij ME van, Segers-Nolten IMJ, Subramaniam V. (2006) Biophys. J: Biophys. Lett. 91:L96-L98
5. Segers-Nolten I, Van der Werf K, Van Raaij M, Subramaniam V. (2007) Proceedings of the IEEE Conf. Eng. Med. Biol. Soc. 6609-12
6. Villar M, Chou H, Luhrs T, Maji SK, Riek-Loher D, Verel R, Manning G, Stahlberg H, Riek R. (2007) Prot. Natl. Acad. Sci. 105:8637-42
7. Kjelstrup-Hansen J, Hansen O, Rubhan HG, Bøggild P. (2006) small 2:660-66
8. Koenders MMJF, Yang L, Wismans RG, Van der Werf KO, Reinhardt DP, Daamen W, Bennink ML, Dijkstra PJ, Van Kuppevelt TH, Feijen J. (2009) Biomaterials 30:2425-32
9. Yang L, van der Werf KO, Koopman BFJM, Subramaniam V, Bennink ML, Dijkstra PJ, Feijen J. (2007) J. Bio. Mat. Res. 82:160-68
10. Smith JF, Knowles TPJ, Dobson CM, MacPhee CM, Welland ME. (2006) Prot. Natl. Acad. Sci. 103:15806-11
11. Chou SY, Krauss PR, Renstrom PJ. (1996) J. Vac. Sci. Tech. 14:4129-33
12. Hegner M, Wagner P, Semenza G. (1993) Surf. Sci. 1:39-46
13. Hirai Y. (2005) J. Photopol. Sci. Techn. 18:551-58
14. Knowles TPJ, Oppenheim TW, Buell AK, Chirgadze DY, Welland ME. (2010) Nature Nanotech. 5:205-7

CHAPTER 10

Concluding remarks

Atomic force microscopy is a widely used technique to obtain nanometer scale morphological and mechanical characteristics of amyloid fibrils. This thesis has systematically explored the vast possibilities of the method, while carefully considering its limitations, to gain quantitative insights into the structure and mechanical properties of α-synuclein fibrils associated with Parkinson's disease. Although the attention of the field has shifted towards the intermediate aggregation products like oligomers, it remains very important to understand the full aggregation pathway, including the mature fibrils, in order to get a comprehensive picture of the pathology and progression of the disease. Moreover, the extreme stability of amyloid fibrils and their ability to self-assemble makes them increasingly interesting as nanobiomaterials. Exploiting the self-assembly properties in a controlled fashion, and using the toolbox of modern molecular biology and nanotechnology, allows one to fabricate functional nanostructures, surfaces with special properties, or networks that could possibly be used as scaffolds for cells for tissue regeneration purposes.

The AFM technique is now available for more than 20 years. A wealth of technical detail is available in the literature describing the unprecedented ability of this imaging modality to obtain nanometer-scale information. The increasing commercial availability of these instruments makes the technique more accessible to a wide range of scientists in different fields, and is of particular interest to biomedical scientists owing to its ability to measure in solution in near-native conditions. However, the method is not without its pitfalls, and careful consideration must be given to those factors that can lead to errors in analysis and interpretation of the data. Such errors can occur due to non-optimal AFM settings, effects of the surrounding media, or even the underlying substrate. Mechanical properties derived from AFM measurements are even more prone to large differences due to instrumental settings and analysis methods. The introduction of new

high-frequency nanomechanical approaches has made probing for mechanical properties at the nanoscale easier. It is important to keep in mind that measurements at these high frequencies often have a significant impact on the results, as discussed in this thesis (Chapter 8). This thesis demonstrates that with careful consideration to instrumental settings, systematic application of analysis methods, and the use of different AFM operation modes, it is possible to extract fascinating new information about structure and mechanics of amyloid fibrils at nanometer length scales.

Finally, the morphological and nanomechanical studies on α-synuclein fibrils are integrated into self-consistent structural model for α-synuclein fibril organization. In this model, α-synuclein fibrils would have six smaller filaments that are circularly arranged, or intertwined in two twisted bundles of three filaments (Chapter 6). The nanoindentation experiments resulted in a high modulus of elasticity (1.3 GPa), which suggests a tight packing of monomers within the fibril core. These results were confirmed by experiments comparing fibrils imaged in air versus liquid, which also suggest little room for water molecules within the core. The proposed packing arrangement of the filaments within the core is a result from both morphological and mechanical data from this thesis.

SUMMARY

Misfolding of proteins leading to formation of fibrillar aggregates called amyloid fibrils is a process commonly associated with neurodegenerative diseases. The mechanism which leads to amyloid aggregation is not yet fully understood. Amyloid fibrils is a general term for aggregates with the following characteristics: (1) the fibrils are around 10 nm in diameter, (2) they bind to dyes such as Thiovlavin T and (3) the fibrils consists of cross β-sheets stacked perpendicular to the fibril axis and exhibit intermolecular hydrogen bonds. These fibrillar structures also appear to have very specific, and universal, material properties, irrespective of the protein from which they are formed.

Disease related amyloid fibrils are studied for understanding the pathology, origin and progression of the disease. Moreover, amyloid fibrils, whether formed from disease-related or other proteins, are becoming more interesting for applications in biotechnology. Atomic force microscopy (AFM) appears to be a very suitable tool to study amyloid fibrils in their near-native environment, such as physiological buffers. AFM is capable of performing both morphological and mechanical analysis on the fibrils. Especially the mechanical properties of the fibrils are becoming increasingly interesting from a nanomaterials point of view.

In this thesis we have studied the structural and mechanical properties of amyloid fibrils formed by the human α-synuclein protein, associated with Parkinson's disease. The thesis is divided in three parts where firstly the influence of the surface on morphological and mechanical properties is investigated. The morphological differences on 5 different substrates are discussed in chapter 3. IN chapter 4 the interaction between the fibrils and supported lipid bilayers is investigated using morphological, mechanical and affinity parameters. Secondly, a more detailed study in to the structural characteristics of the amyloid fibrils is performed. In chapter 5 environmental influences, like different buffers, are used to get a more detailed understanding of structural characteristics, mainly the situation and structure of the C-terminal region. Chapter 6 uses both morphological and mechanical properties to develop a structural model. The last part is completely focused on the mechanical properties of amyloid fibrils and how to measure them accurately. In chapter 7, single-point nanoindentation measurements are performed and these are systematically compared to the results obtained with the newly-developed surface property mapping techniques like Peakforce QNM and HarmoniX. These techniques use much higher frequencies to perform the indentation curves and to create higher data throughput. The influences from probing materials at these higher frequencies are discussed in chapter 8. Chapter 9 is an exploratory study towards the

possibility of performing bending experiments on single fibrils.

A structural model for fibril organization that is consistent with all morphological and nanomechanical measurements would have the α-synuclein fibrils with six smaller filaments which are circularly arranged or in two twisted bundles of three filaments. The highly negatively charged C-terminal region remains unstructured outside the fibril. This C-terminal part can be modulated by charge shielding with different ion-concentrations increasing or decreasing the fibril size. Furthermore, we hypothesize that there is limited room for water molecules within the fibril core. This is verified by both height measurements and mechanical measurements. Air/liquid height measurements showed drying artifacts of around 18% for fibrils of full-length wild-type protein. However, similar measurements on C-terminal truncated fibrils did show negligible height differences. This indicates that the drying artifact was only induced by the C-terminal region. Furthermore, nanoindentation resulted in a high modulus of elasticity (~1.5 GPa) for both air and liquid measurements suggesting a stiff structure with no changes in modulus of elasticity upon drying.

SAMENVATTING

Het misvouwen van eiwitten dat leidt tot de vorming van fibrillaire aggregaten, welke amyloid fibrillen genoemd worden, is een proces dat vaak geassocieerd wordt met neurodegeneratieve aandoeningen. Het mechanisme achter deze aggregatie is nog lang niet volledig begrepen. "Amyloid fibrillen" is een algemene term voor aggregaten met drie typische kenmerken: (1) de fibrillen zijn ongeveer 10 nm in diameter, (2) ze binden aan kleurstoffen zoals Thiovlavin T en (3) de fibrillen zijn opgebouwd uit β-sheets die loodrecht gestapeld zijn, verbonden met intermoleculaire waterstofbruggen, langs de as van de fibril. Deze fibrillen blijken altijd deze zeer specifieke en universele materiaaleigenschappen te hebben ongeacht het eiwit waaruit ze zijn gevormd.

De ziekte gerelateerde amyloid fibrillen worden vaak bestudeerd om de pathologie, de oorsprong en de voortgang van de ziekte beter te begrijpen. Maar de fibrillen, ongeacht of ze gevormd zijn uit ziekte-gerelateerde of andere eiwitten, worden ook steeds interessanter voor toepassingen in de biotechnologie. Atomic force microscopie (AFM), of atomaire krachten microscopie, blijkt een zeer geschikte techniek om de fibrillen te bestuderen in hun bijna natuurlijke omgeving, zoals fysiologische buffers. AFM is in staat om zowel de morfologische als mechanische eigenschappen van de fibrillen te analyseren. Maar vooral vanuit een materieel oogpunt worden de mechanische eigenschappen van de fibrillen steeds interessanter.

In dit proefschrift hebben we de fibril structuur van de fibrillen, maar ook de mechanische eigenschappen van fibrillen bestudeerd. Deze fibrillen zijn gevormd door het menselijk α-synucleïne eiwit, geassocieerd met de ziekte van Parkinson. Het proefschrift is verdeeld in drie delen waar eerst de invloed van het oppervlak op de morfologische en mechanische eigenschappen onderzocht is. In hoofdstuk 3 worden de morfologische verschillen op 5 verschillende substraten gemeten. In hoofdstuk 4 wordt de interactie tussen de fibrillen en lipidedubbellagen onderzocht met behulp van morfologische en mechanische eigenschappen en affiniteit parameters. In het tweede deel wordt een meer gedetailleerde studie van de structurele kenmerken van de amyloid fibrillen uitgevoerd. In hoofdstuk 5 worden omgevingsinvloeden gebruikt, zoals verschillende buffers, om de structurele eigenschappen van het C-terminus gedeelte van het eiwit te verkrijgen. Hoofdstuk 6 maakt gebruik van zowel morfologische en mechanische eigenschappen om een model te vormen dat de structuur van de filamenten in de fibril beschrijft. Het laatste deel is volledig gericht op de mechanische eigenschappen van de fibrillen en hoe deze te meten zijn. In hoofdstuk 7, zijn nano-indentatie metingen uitgevoerd en deze worden systematisch vergeleken met de resultaten verkregen met de pas nieuw

ontwikkelde technieken zoals Peakforce QNM en HarmoniX. Deze technieken brengen ook de mechanische eigenschappen in kaart, maar om dit op snelheid te kunnen doen maken ze gebruik van veel hogere frequenties om de metingen uit te voeren. De invloeden van het indenteren van materialen bij deze hogere frequenties worden besproken in hoofdstuk 8. Hoofdstuk 9 is een verkennende studie naar de mogelijkheid van het uitvoeren van buig experimenten op enkele individuele fibrillen.

Voor de fibril organisatie is een model opgesteld dat de fibrillen beschrijft als zes kleinere filamenten die circulair zijn opgesteld of als twee gedraaide bundels van drie filamenten. Dit model is in overeenstemming met alle morfologische en mechanische metingen die gedaan zijn in dit proefschrift. In dit model zit de negatief geladen C-terminus ongestructureerd buiten de fibril. Het C-terminus gedeelte kan vervolgens gemoduleerd worden door de ladingen op het eiwit af te schermen met verschillende zoutconcentraties, dit resulteert in verschillende fibril hoogtes. Verder veronderstellen we dat er in de fibril kern beperkte ruimte is voor water moleculen. Dit wordt aangetoond door zowel hoogtes als mechanische metingen. Lucht / vloeistof hoogtemetingen geven hoogteverschillen van ongeveer 18% voor de fibrillen gevormd door het volledige lengte wild-type eiwit. Echter, soortgelijke metingen op C-terminus afgeknipte fibrillen toonden verwaarloosbare hoogteverschillen. Dit geeft aan dat het geobserveerde opdroog effect alleen werd geïnduceerd door de C-terminus. Bovendien leidde de nano-indentatie metingen tot een hoge elasticiteitsmodulus (~ 1,5 GPa) voor lucht en vloeistof metingen. Dit duidt op een stijve structuur zonder veranderingen in elasticiteitsmodulus tijdens opdrogen.

DANKWOORD

Na 4 jaar is het dan eindelijk zover en ben ik aan het belangrijkste, meest gelezen hoofdstuk van mijn boekje aangekomen: het dankwoord. Hoewel er altijd maar 1 naam op de voorkant van zo'n proefschrift staat is de inhoud natuurlijk nooit tot stand gekomen door de hulp van een grote groep mensen, zowel werk gerelateerd als op persoonlijk vlak.

Allereerst Vinod en Martin, dank je wel dat ik na mijn afstuderen mocht blijven en lekker aan de gang mocht blijven met de AFMs. Hoewel dingen misschien niet altijd even soepel liepen is het toch maar mooi af gekomen in 4 jaar en daar ben ik erg blij mee. Ik had jullie beiden nodig voor zowel het biologische gedeelte als de technische kant van het verhaal. Verder ben ik erg blij dat jullie me vrij gelaten hebben om te doen wat me leuk leek terwijl er toch voldoende sturing was om er gevuld boekje van te maken. Martin, het was prettig dat ik altijd zo binnen kon vallen voor discussies over resultaten of artikelen of gewoon een gezellig kletspraatje (let op, dit wordt een terugkerend thema in dit dankwoord, je mag ook lezen: Ouwehoeren…).

Naast Vinod en Martin is een van de belangrijkste personen voor dit boekje toch wel Kees geweest. Kees; bedankt dat je altijd geduldig bleef als ik iets niet begreep, iets niet lukte met de AFM of als ik gewoon zin had om te zeuren. Ik vond het samenwerken met jou toch wel echt een van de leukste dingen van de afgelopen 4 jaar. Ik heb veel van je geleerd, bijvoorbeeld in het bedenken van praktische oplossingen. Zeg nou zelf, een baardhaar is een prima referentiepunt. Ook de echt inhoudelijke discussies waren altijd erg nuttig en verhelderend, maar laten we vooral de gezellige kletspraatjes niet vergeten. Ik vind het heel erg jammer dat je niet mee verhuist naar Demcon. Ik heb er al even goed rondgekeken, maar heb er geen 2e Kees kunnen vinden.

Ine, via jou ben ik eigenlijk in de groep terechtgekomen en de begeleiding bij mijn afstuderen zorgde er mede voor dat ik bleef. Je stond altijd klaar als ik je nodig had voor metingen, materiaal, als dingen niet zo lukten of gewoon voor de kletspraatjes. En ons artikel waar we 4 jaar geleden aan begonnen zijn is nu dan toch maar mooi geaccepteerd.

Tom, Dirk Roelof en Annelies (en ook Ellen voor een paar maanden), mijn hokgenoten. Het is erg fijn geweest dat ik bij jullie op kantoor kon zitten. Het was altijd gezellig en ik heb veel aan jullie gehad. Het gewone kletspraatje, het afreageren als iets weer niet lukte, het zoeken naar het juiste Engelse woord waar je dan weer niet op komt en ga zo maar door. Ik denk dat ik wel kan zeggen dat we met zijn allen Tom heel erg miste toen hij weg moest. Maar ik denk dat het vooral voor Dirk Roelof soms zwaar was, zo in het

(kippen)hok met Annelies, Ellen en mij.

Hetty, dank je wel voor de training op de multimode en dat ik te pas en te onpas jouw AFM ook echt mocht gebruiken. Verder hielp je altijd goed om de soms ellenlange saaie AFM metingen door te komen met kletspraatjes.

Sissi, dank je wel voor de hulp met HarmoniX. Hoewel de rest van het project niet meer zo van de grond is gekomen ben ik blij met de resultaten die we behaald hebben.

Kirsten, Yvonne en Marloes, ik ben jullie dankbaar voor al het werk wat jullie altijd weer stoppen in het maken van eiwit wat wij dan met zijn allen weer binnen no-time opmaken. Ik heb er altijd dankbaar gebruik van gemaakt. Ook ben ik jullie heel erg dankbaar voor als ik weer eens iets in het enge lab moest doen wat ik dan eigenlijk niet zo goed kan. Gelukkig stonden jullie altijd klaar om mij dan toch te helpen. Ook Anja en Martin hebben me goed geholpen met het maken van lipid vesicles.

De hele synuclein groep (niet op volgorde van nog aanwezig of belangrijkheid), Bart, Bart, Gert Jan, Tom, Dirk Roelof, Anja, Martin, Mireille, Ine, Chris, Martijn en wie ik verder nog vergeten ben. De discussies tijdens de werkbespreking, maar ook daarbuiten waren altijd erg nuttig.

Thea, jij was toch wel de beste en leukste student die ik gehad heb. Nu zegt dat misschien niet zo heel veel, maar ik vond het erg leuk om met je te werken. Ik heb er veel van geleerd en ik hoop stiekem jij ook.

Daarnaast natuurlijk de rest van de groep. Koffiepauzes, lunches, uitjes, conferenties, het Veldhoven gebeuren was altijd erg gezellig.

Naast dingen doen voor mijn proefschrift heb ik ook met verschillende collega's van allerlei andere dingen gedaan. Samen met Dirk Roelof een jaartje de colloquia verzorgt. Het fitnessgroepje op vrijdagmiddag was ook altijd gezellig, helaas niet geslaagd genoeg voor mij om het vol te houden ☺. Wilma, we hebben toch een aantal keertjes gezellig gezwommen en we werden steeds beter. Dan heb ik nog 3 weken in een grote ronde witte tent gestaan samen met Kees en Robert, gedeelde smart is halve smart. Hoewel het een grote puinhoop was vond ik hartstikke leuk om te doen en dat kwam mede door jullie. Als laatste heb ik met Dirk nog een aantal jaren geprobeerd een vrijdagmiddag borrel van de grond te krijgen. Hoewel dit misschien niet het meest succesvolle is wat we ooit gedaan hebben zal het niet aan ons gelegen hebben.

Als laatste moet ik nog 2 belangrijke personen bedanken: Sylvia en Frans. Heel erg bedankt voor alles wat jullie wilden regelen.

Om het bruggetje te slaan tussen collega's en vrienden: Liesbeth, dank je wel voor de leuke tijd tijdens zowel de UT-werk, UT-sport en de wijntjes thuis! Vrienden en familie,

dank jullie wel voor de welkome afwisselingen met werk in de vorm van etentjes, verjaardagen, skivakanties, familie weekend (stiekem toch altijd weer erg gezellig), zonvakanties zoals Tenerife, muziekfestivals en meer.

Pap & mam, dank jullie wel voor alles. Niet alleen de afgelopen 4 jaar maar ook alle jaren daarvoor. Het heeft allemaal even geduurd, maar nu is het echt allemaal af. En zusje, ik ben heel erg blij dat we het zo goed samen kunnen vinden en ik hoop dat dat zo blijft.

Als laatste Marc, ik kan eigenlijk niks bedenken wat niet kazig klinkt dus moet het maar: Dank je wel voor alles en ik heb heel erg zin in de komende tijd met spruitje.